ABSTRACT

Title of Dissertation: DEFORMATION MECHANICS OF SOFT MATTER UNDER EXTERNAL STIMULI

Jian Cheng, Doctor of Philosophy, 2019

Directed by: Professor Teng Li,
Department of Mechanical Engineering

Artificial soft matters are a class of materials which can be easily deformed by external stress, typical examples include foams, colloids, elastomers, and hydrogels. Due to their unprecedented and unique properties, such as large deformability, high resemblance to biological systems, versatile response to multi-physical stimuli, and biological compatibility, soft matters have found applications in fields like soft actuators and robots, soft sensors, bio-mimicking material systems, micro-fluidic system control, biomedical engineering, etc. In these applications, the large deformability of soft matters has taken an enabling role. The deformation theory of polymeric soft matters can date back to 1940s in the early infancy of the statistical mechanics sketch of rubbery materials, with a fast growth in the most recent decade concurring the latest progress in soft matters. However, the mechanical modeling of soft matter leaves many open questions.

This doctorate research is devoted to advance the understanding of the deformation mechanics of soft matter, specifically, from the following aspects: (1) how the chemo-

mechanical interaction between the solvent molecules and the polymeric network invokes anomalous behaviors of a thin-walled hydrogel structure under internal pressure, in contrast to its polymer counterpart; (2) the application of the dielectric elastomer as sensing medium in soft sensor technology; (3) the development of a novel light-responsive hydrogel material system with the application in bio-mimicking shape transform; (4) and enriching the existing theory to facilitate the mechanistic understanding of the deformational behaviors of a type of fiber-reinforce anisotropic hydrogels.

For that, this dissertation (1) reveals the delayed burst of hydrogel thin-shell structures as a new failure mechanism, which is dissimilar from the instantaneous burst of a rubber shell: at a subcritical applied pressure the burst occurs with a delay in time; (2) presents a facile design of capacitive tactile force sensor using a dielectric elastomer subjected to a modest voltage and a pre-stretch; (3) develops a theoretical framework to simulate the light-responsive deformation of the proposed hybrid hydrogel system; and (4) from the perspective of micromechanics, constructs a constitutive model suitable for the microfiber-reinforced anisotropic hydrogel, with large deformation, mass transportation, and the origin of anisotropy are intrinsically captured.

DEFORMATION MECHANICS OF SOFT MATTER UNDER EXTERNAL STIMULI

by

Jian Cheng

Dissertation submitted to the Faculty of the Graduate School of the
University of Maryland, College Park, in partial fulfillment
of the requirements for the degree of
Doctor of Philosophy
2019

Advisory Committee:
Professor Teng Li, Chair
Professor Hugh A. Bruck
Professor Abhijit Dasgupta
Professor Bongtae Han
Associate Professor Dongxia Liu, Dean's Representative

Dedication

This doctorate dissertation is dedicated to my mother, who has brought me up with enduring patience and love, for the great sacrifice she has made to offer me the best upbringing and education a parent can ever provide.

Table of Contents

List of Tables

List of Figures

Chapter 1: Introduction

1.1 Background and Motivation

Artificial soft matters are a class of material which can be easily deformed by external stress[1]. Typical examples include foams[2], [3], colloids, elastomers[4]–[6], and hydrogels[1], [7]–[13]. The past decades have witnessed a rapid growth in research interest in soft matters due to their unprecedented and unique properties, such as large deformability, high resemblance to biological systems, fast and versatile response to multi-physical stimuli, and biological compatibility[10]. As a result, soft matters have found applications in fields like soft actuators and robots[4]–[6], soft sensors, bio-mimicking material systems, micro-fluidic system control [9], [11]–[13] tissue engineering [7], [14] biomedical engineering [7], [9], [10], [13], drug delivery system [15] and in the development of novel materials with exceptional mechanical properties [8].

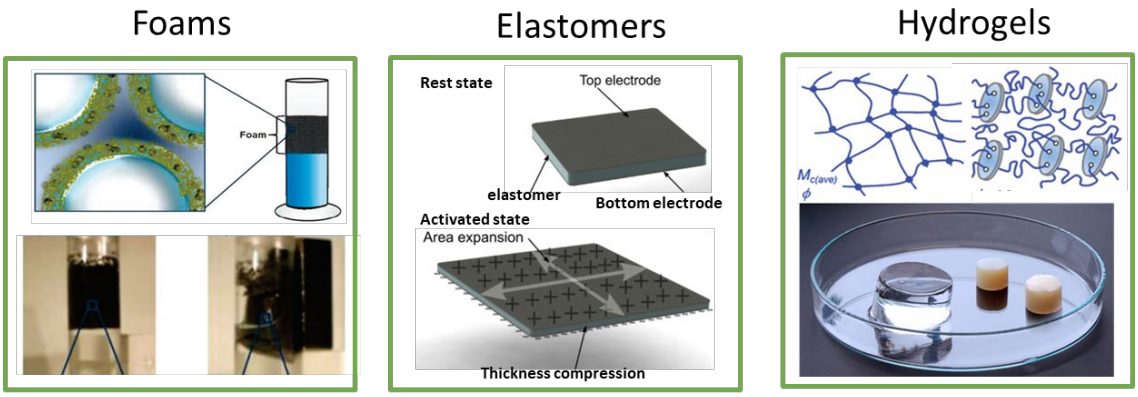

Figure 1.1 Example of soft matters:(a) foams [3], (b) elastomers [5], and (c) hydrogels [16].

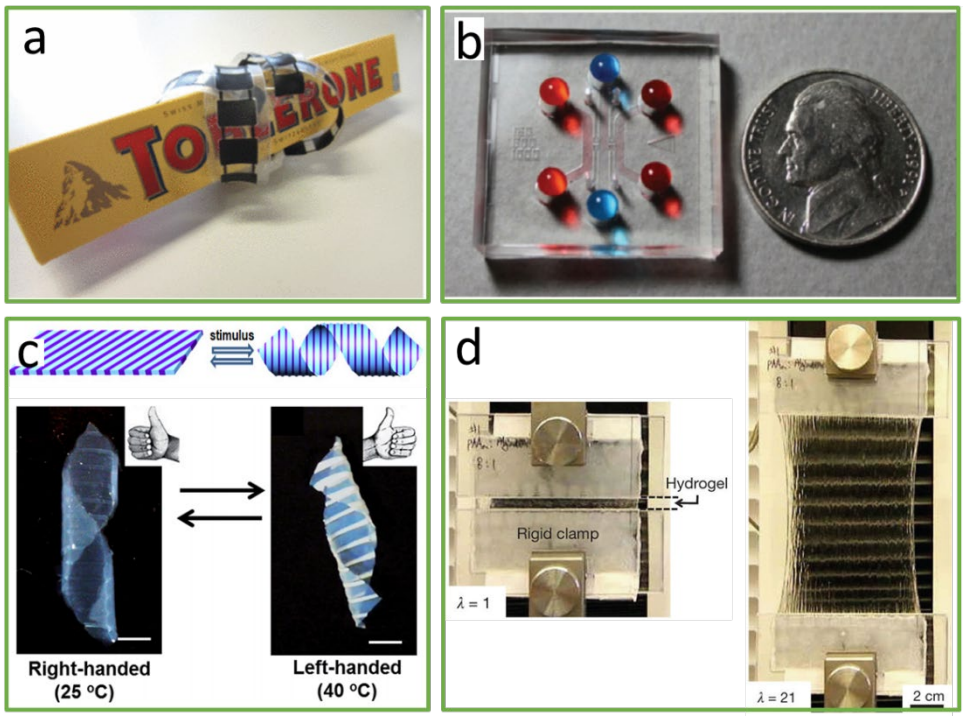

Figure 1.2 Examples of the applications of soft materials. (a) A dielectric-elastomer-based robot gripper[4]. (b) A microfluidic channel system with hydrogel-based controllable valves [9]. (c) A morphology change strategy based on hydrogel. [17] (d) A tough hydrogel with exceptional stretchability and toughness [8].

In the development of the abovementioned applications, the large deformability of soft matters has taken an enabling role. For example, the robot fingers rely on the deformation actuated by dielectric elastomer to perform gripping and releasing [4]; the hydrogel valve in the microfluidic control system switches between on/off mode by shrinking or swelling [9]; the macroscopically hybrid hydrogel piece scrolls into a 3-dimensional morphology by invoking the differential swelling of the neighboring gel blocks [17]; and the super tough and extremely stretchable hydrogel is realized through a deformation procedure accompanied by an energy dissipation mechanism [8]. As demonstrated in these examples,

such a polymeric-network-based soft material can afford all types of large deformation, including shrinking, swelling, bending, and stretching.

The deformation theory of polymeric soft matters can date back to 1940s in the early infancy of the statistical mechanics sketch of rubbery materials. For example, the interaction mechanism of solvent molecules dispersed in the polymer matrix in a hydrogel material is formulated by Flory and Rehner, as a pioneering work in this field [18]. From a thermostatistical point of view, the free energy of a hydrogel is postulated to take the form of

$$W = W_{\text{network}} + W_{\text{mixing}} \tag{1-1}$$

where W_{network} represents the entropic conformational energy due to the deformation of the polymer network, and W_{mixing} denotes the energy stemming from the mixing of two chemical species. Ever since, this formulation has been revisited sporadically over a time span of half a century [14], [18]–[21]. However, these developments are mainly restricted to the aspect of statistical mechanics and physics, until the Flory-Rehner theory was recast by Zhao et al. [22] and Hong et al. [23] in the framework of continuum mechanics, which concurs the recent fast progresses in soft matter [1], [7]–[13].

The physics depicted by Equation (1-1) is concise but powerful. In fact, the second term can be replaced by the energy of all other natures presenting in the soft matter system, i.e.

$$W = W_{\text{network}} + W_{\text{other}} \tag{1-2}$$

The material specific of W_{other} makes possible the constitutive model of a vast variety of soft matters by using such a formulation. For example, for a poly (N-isopropyl acrylamide)

temperature sensitive hydrogel, W_{other} represents the enthalpy of a globule-to-coil phase transition of network [24], [25]; for an ionic hydrogel, W_{other} includes the energy due to ionic association/dissociation [26], [27]; for a dielectric elastomer, W_{other} represents the electrostatic energy of polarization [28], [29]; and for a hydrogel system with embedded colloidal micro-filler array, W_{other} accounts for the DLVO potential of the colloid particles [30], etc.

1.2 Scope and goals

This research plan is devoted to advance the understanding of the deformation mechanics of soft matters, specifically, from the aspect of (1) the chemo-mechanical interaction of the solvent molecules and the polymeric network in a hydrogel; (2) the application of the dielectric elastomer in soft sensor technology; (3) the development of a novel light-responsive hydrogel material system with the application of bio-mimicking shape change; (4) as well as enriching the theoretical scheme formulated by Equation (1-2) to model the behavior of a type of fiber-reinforce anisotropic hydrogel.

Within the topic of *Deformation Mechanics of Soft Matter under External Stimuli*, the layout of this doctorate reach is organized into the following chapters:

1.2.1 Deformation of a thin-walled hydrogel structure and delayed burst in a hydrogel balloon

This chapter attempts to demonstrate how the chemo-mechanical interaction between the solvent molecule species and the polymeric network would invoke anomalous behaviors of a thin-walled hydrogel structure under external mechanical load, in contrast to its

polymer counterpart. Specifically, the delayed burst mechanism in the inflation of a hydrogel balloon is investigated. Such a unique instability phenomenon might also be complicated by the delayed fracture of the hydrogel material, leading to a failure mode that is previously unseen.

1.2.2 Dielectric-elastomer-based capacitive force sensor with tunable and enhanced sensitivity

This chapter focuses on the deformation mechanics of dielectric elastomers. We leverage the tunable mechanical behavior of dielectric elastomer under voltage in the facile development of a force sensor with enhanced and tunable sensitivity. The sensitivity of the sensor can be continuously elevated in an *in-situ* manner to more than 40 times its original performance.

1.2.3 Deformation of temperature-sensitive hydrogel and the development of a light-responsive morphology transform

The deformation mechanics of poly (N-isopropyl acrylamide) temperature-sensitive hydrogel in an inhomogeneous temperature field is studied in this chapter. The deformation of the hydrogel is obtained by a using coupled heat transfer and mechanics finite element method scheme. We further present a hybrid hydrogel system, which comprises a dispersed Au nanoparticle phase that absorbs near infrared irradiation and transduces the light into heat flux. The present hybrid hydrogel system features a fast and reprogrammable shape transform in response to light.

1.2.4 Deformation mechanics of fiber-reinforced anisotropic hydrogels

This chapter aims to enrich the deformation mechanics of hydrogel to model the anisotropic material properties of a type of fiber-reinforced hydrogel. We put forward a free energy density function which incorporates the conformational energy due to the affine deformation of the reinforcement fiber family. This constitutive model is related to the microscopic picture of the fiber-reinforced hydrogel through a distribution function of the constituent fibers. Through an array of studied cases, such as anisotropic free swelling, deformation under uniaxial stretch, we verify the proposed model's capability of capturing anisotropic behaviors of microfiber-reinforced hydrogels. We will enable the theoretical prediction of the deformation under complicated and inhomogeneous external loads. More importantly, we will apply the model in an attempt to shed light in some intriguing and useful applications of anisotropic hydrogels, such as soft actuators.

Chapter 2: Deformation of a Thin-Walled Hydrogel Structure and Delayed Burst of a Hydrogel Balloon[1]

When inflating a rubber balloon, it is commonly concluded that a sudden expansion in balloon size (i.e. the burst) occurs once the inner pressure reaches a critical threshold, the instantaneous burst pressure. Such burst phenomena are usually attributed to the snap-through instability. In this work, we demonstrate that when a hydrogel balloon is subject to a subcritical pressure lower than the instantaneous burst pressure, the hydrogel balloon may remain stable for a span of time, and then burst suddenly. We refer to such burst phenomena as the delayed burst of the gel balloon. When subject to such a subcritical inner pressure, a hydrogel balloon slowly and continuously absorbs solvent and swells. We find the instantaneous burst pressure of the hydrogel balloon to be a decreasing function of swelling ratio. The criterion for the onset of the burst is that the swelling-related instantaneous burst pressure drops to the applied inner pressure. The delayed burst can, therefore, be attributed to the time needed for the hydrogel swelling to reduce the instantaneous burst pressure to the level of applied pressure. We further delineate a map indicating three distinct deformation modes of gel balloons, i.e. instantaneous burst, delayed burst, and steady deformation without burst (safe mode), in the parameter space of applied pressure and mechanical properties of the hydrogel. The delayed burst of a hydrogel balloon is counterintuitive and a crucial aspect in developing hydrogel-shell-

[1] The main findings from this chapter have been published as J. Cheng, Z. Jia, H. Guo, Z. Nie, T. Li, Delayed burst of a gel balloon, *Journal of the Mechanics and Physics of Solids* 124, 143-158 (2019).

based soft actuators and soft machines. The research findings may shed light on the understanding of the complex failure mechanisms of hydrogel actuators and also facilitate the design of hydrogel-based tissue delivery capsules.

2.1 Background

Hollow thin-shell structures have found widespread applications from as small as nano-anodes in Li-ion batteries [31] to as large as radar domes and fuel tanks [32]. The past decade has witnessed a wealth of attentions paid to soft thin shells, which represent a paradigm shift in research interests from conventional rigid structures to deformable, inflatable, and multifunctional components. For instance, the use of soft polymeric thin shells has been embraced as a trending strategy for soft actuator and soft robot design: inflated either pneumatically or hydraulically, such a strategy provides a promising avenue for agile and swift actuation. By controlling the pressurization of each individual joint in concert with the others, the actuators are able to achieve complex motions, such as walking [33]–[35], jumping [36], swimming [37], [38], and gripping [39]. For example, Wehner et al. successfully prototyped a soft octopus-like robot and controlled its motion via an embedded microfluidic system [40]; Acome et al. designed a soft gripper driven by the localized inflation of a hollow structure by electrostatically directing the motion of liquid dielectrics [39]; Kim et al. demonstrated a multifunctional inflatable catheter as a surgical tool that delivers therapy and diagnosis to desired local lesions [41]. Despite successful applications of soft polymeric thin-shell structures in soft actuators and medical devices, their applications in biomedical engineering and tissue engineering are often hindered by

poor biocompatibility arouse from the physical dissimilarity between polymeric materials and living tissues.

Hydrogels are composed of a considerable amount of water and a polymer network. This unique combination provides biocompatibility, permeability, and deformability. For this reason, hydrogel thin-shell structures such as hydrogel capsules have emerged in a myriad of biomedical applications such as *in vitro* 3D tissue culture [42]–[45], biomedical sensors [46], cell-based therapy development [47]–[49], drug delivery [50], and bio-mimicking structures [51]. Alessandri et al. described a method to culture tumor cellular aggregations encapsulated in cross-linked alginate hydrogel shells. By monitoring the expansion or even burst of the hollow spherical hydrogel shells, the growth of tumor cells under mechanical confinement can be directly investigated [46]. In addition, for applications such as drug release [52] and cell therapy [53], the burst and degradation of the hydrogel capsule play a pivotal role. That is, the burst event has to precisely concur with the drug's arrival at the delivery target or the tissue's full development. A premature release only results in an unsuccessful delivery of under-developed tissues, whereas a late burst may cause adverse reactions [53], [54]. Therefore, understanding the deformation and burst mechanism is the key to successful applications of hydrogel thin-shell structures in biomedical and tissue engineering.

Inflation and burst of an elastomeric thin-walled structure have long been a focal topic of solid mechanics. One of the earliest accounts of the inflation of a rubber balloon is predicted analytically by Feodos'ev [55]. This pioneering work was followed by others with their main attention devoted to the inflation response of hyperelastic materials with

different constitutive assumptions [56]–[59] and of different geometries [60], [61]. According to these classical notes, it is both observed experimentally and concluded theoretically that, when inflating a rubber balloon, a sudden expansion in balloon size (i.e. the burst) occurs once the inner pressure reaches a critical threshold, the instantaneous burst pressure. Such burst phenomena are commonly attributed to the snap-through instability. Based on these understandings, most recent research interests are also directed to harness such snap-through instability to our benefit, such as achieving enhanced actuation performances of soft actuators [62], [63], or to investigate the highly enriched deformation bifurcations of electrically active soft materials due to instability [64], [65].

Despite extensive studies on elastomeric thin-walled structures, the instability of hollow hydrogel structures is far from well understood. Wang and Cai investigated drying induced growth of inner cavity in confined hollow spherical hydrogels [66], however, in that study, the inflation of the hydrogels is restricted by rigid confinement at its outer surface. Alessandri et al. experimentally observed growth-induced bursts of the spherical hydrogel capsules in the culture of tumor tissue, however, a quantitative mechanistic understanding of the burst of hydrogel capsules remains elusive [46]. To address these unsolved issues, a systematic study of inflation and burst of hollow thin-walled hydrogel structures should be carried out. Most recently, Zamani and Pence investigated the swelling-induced burst of a swellable Mooney-Rivlin spherical shell [67]: the pressure-expansion response was simply studied by assigning an increasing swelling factor to the elastic shell; However, some key questions still remain unclear in their study: (1) What is the underlying physics bestowing the swellable behavior of the hyperelastic network? (2) Will the balloon shell further swell

under inner pressurization? (3) If the further swelling indeed occurs, what serves as the driving force and to what extent the balloon shell will swell? In the present paper, we will directly answer these open questions.

As aforementioned, hydrogels intrinsically differ from elastomers and polymers. In the hydrogel, the polymer chains are interacting with water molecules by weak intermolecular forces. When a hydrogel is in contact with an aqueous environment and subject to mechanical loads and confinements, water migrates in and out the hydrogel to accommodate the applied loads and boundary conditions. Therefore, the deformation behavior and failure of a hydrogel structure also deviate from its water-free elastomeric counterparts. For example, when a hydrogel sample containing a pre-crack is subject to a static load less than the critical load for instantaneous fracture, the pre-crack initially remains virtually stationary for some time, followed by sudden and rapid propagation, causing a catastrophic fracture. Such a facture mode of hydrogel is referred to as delayed fracture [68]–[71], which is usually attributed to viscoelasticity stemming from mechano-chemical reaction in stressed molecular chains [72], [73], dissociation of physical crosslinks [74], [75], and migration of water molecules [68]. Nonetheless, the existing investigation into the delayed failures of hydrogels is primarily limited to its fracture.

Herein, we unveil the delayed burst of hollow spherical thin-walled hydrogel structures (i.e. a hydrogel balloon), a failure mode that has not as yet investigated. Under an interior pressure, a hydrogel balloon gradually and continuously absorbs water and swells. This fact leads to the anomalous delayed burst behavior of a hydrogel balloon: when subject to a subcritical pressure less than the instantaneous burst threshold, the hydrogel balloon

remains stable for a span of time, slowly grows and swells, then expands suddenly in size until burst to fracture. Delayed burst is counterintuitive as it is triggered by a load below the critical threshold for instantaneous fracture. Such a failure phenomenon is also more detrimental than instantaneous burst given its latent nature. Even worse, delayed burst may complicate other failure mechanisms of a hydrogel balloon, such as delayed fracture [68], structure buckling [76], and swelling induced wrinkling [77], [78], especially in the presence of geometry imperfections [79] and material defects [66], [68], [80]–[82]. From the perspective of applications, whether it is on one end of the spectrum where the burst phenomenon is intended as a design feature to fulfil functions such as drug release and cell delivery, or on the opposite end where delayed burst is deemed as a failure mode of applications such as soft actuators, soft robots, and *in vitro* cell cultivation, an accurate mechanistic understanding of the delayed burst of hydrogel balloons is of vital importance.

The rest of this paper is organized as follows. In Section 2, we examine the long-term, hence equilibrium deformation behavior of a hydrogel balloon under interior pressurization at a constant load. The most intriguing finding is the balloon's propensity to imbibe more water molecules into its hydrogel shell, accompanying its expansion in size. Section 3 investigates the instantaneous response of a hydrogel balloon when subject to a rapidly supplied pressure. The findings in Sections 2 and 3 lead to a theoretical explanation of the delayed burst phenomenon of a hydrogel balloon in Section 4. In Section 5, we extend the study to the burst behavior of a hydrogel shell with a finite thickness.

2.2 Deformation of a Hydrogel Balloon

2.2.1 The long-term response of a hydrogel balloon during slow inflation

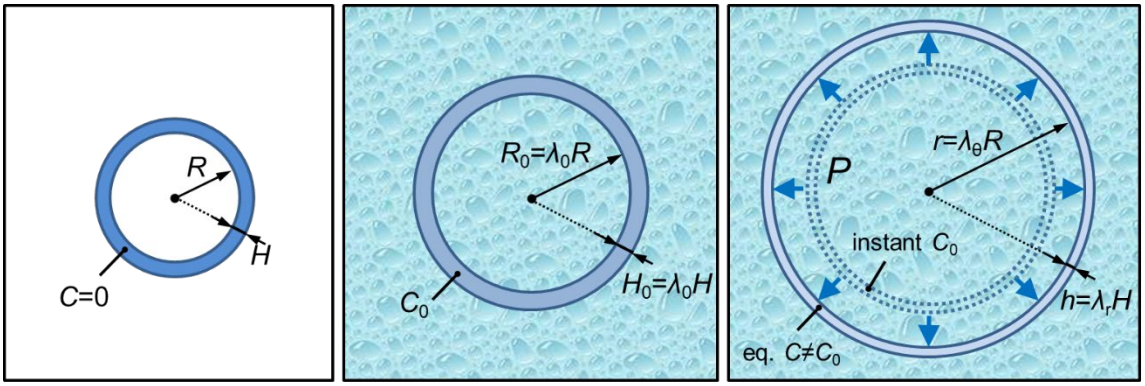

Figure 2.1 Schematic of the inflation process of a hydrogel balloon. (a) The dry state of a hydrogel balloon with its radius being R and thickness H, where $H \ll R$. (b) The free-swelling equilibrium state of the hydrogel balloon in water. (c) The inflated states of the balloon under an inner pressure P. Dashed-line shell: instant deformation under fast pressurization ($t_p \ll t_{eq}$); solid-line shell: long-term final deformation of the hydrogel balloon due to fast inflation ($t_p \ll t_{eq}$) or quasi-equilibrium deformation during slow inflation ($t_p \gg t_{eq}$).

The inflation process of a hydrogel balloon is depicted in Figure 2.1. In its completely dehydrated state (water concentration C=0), a spherical hydrogel shell (or a hydrogel balloon) has a radius of R and a thickness of H, as shown in Figure 2.1(a). In this section, we first consider a thin spherical balloon, namely $H \ll R$. When immersed in water, the hydrogel balloon swells uniformly to a stress-free state with a water concentration C_0 and an isotropic stretch ratio λ_0, such that the network equilibrates with the water surrounding in absence of a mechanical load. With this stress-free stretch ratio λ_0, the radius expands to $R_0 = \lambda_0 R$ and the thickness increases to $H_0 = \lambda_0 H$ (Figure 2.1(b)). In the next step, the balloon is inflated by applying an internal pressure P, accordingly, the radius further expands to r

and the thickness becomes h. Under an evenly distributed interior pressure, the inflated hydrogel balloon retains the spherical symmetry. Provided that the thickness of the balloon shell is much smaller than the overall size of the balloon, the variation over the thickness of both hoop stretch λ_θ and radial stretch λ_r are negligible. Thus, λ_θ can be evaluated approximately at the inner surface; similarly, λ_r can be estimated as the average over the entire thickness, namely

$$\lambda_\theta = \frac{r}{R},\ \lambda_r = \frac{h}{H} \tag{2.3}$$

where λ_θ and λ_r represent the hoop and radial stretches with respect to the dry state, respectively.

The deformation of hydrogels in response to mechanical forces is time-dependent, resulting from the migration of water molecules. The time needed by the hydrogel balloon to reach an equilibrium via water diffusion, t_{eq}, approximately scales with H_0^2/D. Here H_0, the free-swelling shell thickness, constitutes the characteristic length; D represents the diffusivity of water molecules transporting through the hydrogel. Another time scale relevant to the balloon inflation, the time of the pressurization procedure t_p, is defined as the time period as the inner pressure builds up from 0 to P. Depending on the comparison between t_{eq} and t_p, the balloon exhibits disparate mechanical responses to the applied pressure. In the scenarios where pressurization occurs very fast, i.e. $t_p \ll t_{eq}$, the local water concentration inside the hydrogel remains at the same level C_0 as the free-swelling state during the entire loading process, since the time of pressurization t_p is too short for any water molecule to migrate. Immediately after the completion of a fast pressurization procedure (at $t=t_p$), the

hydrogel balloon deforms to what we term the instantaneous inflated state, as sketched schematically by the dashed-lines in Figure 2.1(c).

Considering the molecular incompressibility [23], [83], the volume ratio J can be related to the local water concentration C through

$$J = 1 + \nu C \tag{2.4}$$

where ν is the volume per water molecule. This equation implies that in hydrogel both the polymeric network and the water molecules are incompressible. As a result, the volume of the hydrogel is a summation of the volume of these two constituents. Therefore, because of the unchanged water concentration C, the balloon's instantaneous response to a fast inflation is featured by a volume-conserving deformation, similar to the deformation of elastomeric materials, whose volume change is often negligible. Note that here the conserved volume refers to that of the hydrogel shell rather than the volume enclosed by the balloon; the enclosure volume will nevertheless increase as the balloon expands.

However, if the pressure is applied during a slow process ($t_p \gg t_{eq}$) that takes place incrementally and in a quasi-equilibrium manner, the inflation is accompanied by water transportation across the hydrogel network. According to the molecular incompressibility condition (Eq. (2.2)), with more water content uptake, the volume of the hydrogel shell increases by the volume of the water entering the polymeric network; and conversely, it decreases due to local water content loss. Therefore, the water concentration C is subject to vary in these equilibrium deformations ($C \neq C_0$). While the pressure builds up, the water molecules also take time to migrate, allowing the deformation of the balloon to pass

gradually through a series of quasi-equilibrium states. Moreover, for fast inflation ($t_p \ll t_{eq}$) if the applied pressure is maintained after completion of the loading, i.e. P=const for $t > t_p$, the hydrogel balloon also evolves towards a final equilibrium state, which is the long-term response to pressure P. Regardless of the loading characteristics, given the same applied pressure, the equilibrium responses are essentially the same. The boundary of the equilibrium deformation state is defined by the solid shell in Figure 2.1(c).

In this section, we focus our attention on the long-term/equilibrium deformation of the hydrogel balloon, while leave the instantaneous response to be studied in the next section. Following previous works [23], [83], when immersed in a solvent reservoir with a constant chemical potential μ, the free energy density of a hydrogel in the reference state can be expressed by

$$W = \frac{1}{2}NkT(\lambda_1^2 + \lambda_2^2 + \lambda_3^2 - 3 - 2\log J) - \frac{kT}{v}\left[(J-1)\log\left(\frac{J}{J-1}\right) + \frac{\chi}{J}\right] - \frac{\mu}{v}(J-1) \tag{2.5}$$

where N is the number of polymer chains per unit volume in the dry state, kT is the absolute temperature in unit of energy, λ_i (i=1, 2, 3) denotes the principal stretches of the deformed state, $J = \lambda_1\lambda_2\lambda_3$ is the volume ratio and is related to the local water content through Eq. (2.2), and χ is the dimensionless Flory-Huggins parameter representing the enthalpy of mixing.

The principal component of the nominal stress and Cauchy stress can be calculated by

$$\frac{S_i}{kT/v} = \frac{\partial}{\partial \lambda_i}\left(\frac{W}{kT/v}\right) = Nv(\lambda_i - \lambda_i^{-1}) + \lambda_i^{-1}\left[J\log\left(1-\frac{1}{J}\right) + 1 + \frac{\chi}{J} - \frac{\mu}{kT}J\right] \quad (2.4\text{-}1)$$

$$\frac{\sigma_i}{kT/v} = \frac{\lambda_i}{J}\frac{S_i}{kT/v} = \frac{Nv}{J}(\lambda_i^2 - 1) + \left[\log\left(1-\frac{1}{J}\right) + \frac{1}{J} + \frac{\chi}{J^2} - \frac{\mu}{kT}\right] \quad (2.6\text{-}2)$$

In particular, relative to the dry polymer network, a freestanding hydrogel immersed in water swells with isotropic stretches $\lambda_1=\lambda_2=\lambda_3=\lambda_0$, where λ_0 denotes the isotropic free-swelling stretch. Since the free-swelling state is associated with a stress-free deformation, λ_0 can be determined by equating the Cauchy stress in the hydrogel to zero. Given the value of Nv, the free-swelling ratio λ_0 can be expressed as follows:

$$Nv(\lambda_0^{-1} - \lambda_0^{-3}) + \log(1-\lambda_0^{-3}) + \lambda_0^{-3} + \chi\lambda_0^{-6} - \mu/kT = 0 \quad (2.7)$$

The dimensionless group Nv is identified as the shear modulus of the dry state polymer under infinitesimal strain.

When subjected to an evenly distributed interior pressure, a hydrogel balloon undergoes spherically symmetric deformation. Taking advantage of symmetry, we have hoop stretches $\lambda_1=\lambda_2=\lambda_\theta$, radial stretch $\lambda_3=\lambda_r$, and volume ratio $J= \lambda_\theta^2\lambda_r$. Plugging these relations into Eq. (2.4-1), the nominal hoop and radial stresses are

$$\frac{S_\theta}{kT/v} = Nv\left(\lambda_\theta - \lambda_\theta^{-1}\right) + \lambda_\theta^{-1}\left[J\log\left(1-\frac{1}{J}\right) + 1 + \frac{\chi}{J} - \frac{\mu}{kT}J\right] \quad (2.8\text{-}1)$$

$$\frac{S_r}{kT/v} = Nv\left(J\lambda_\theta^{-2} - J^{-1}\lambda_\theta^2\right) + J^{-1}\lambda_\theta^2\left[J\log\left(1-\frac{1}{J}\right) + 1 + \frac{\chi}{J} - \frac{\mu}{kT}J\right] \quad (2.6\text{-}2)$$

And the Cauchy stresses in the hoop and radial directions can be calculated by using Eq. (2.4-2) as

$$\frac{\sigma_\theta}{kT/v} = J^{-1}Nv\left(\lambda_\theta^2 - 1\right) + \left[\log\left(1 - \frac{1}{J}\right) + \frac{1}{J} + \frac{\chi}{J^2} - \frac{\mu}{kT}\right] \tag{2.9-1}$$

$$\frac{\sigma_r}{kT/v} = J^{-1}Nv(\lambda_\theta^{-4}J^2 - 1) + \left[\log\left(1 - \frac{1}{J}\right) + \frac{1}{J} + \frac{\chi}{J^2} - \frac{\mu}{kT}\right] \tag{2.7-2}$$

In the deformed configuration, the force balance in the radial direction gives

$$\frac{d\sigma_r}{d\rho} + 2\frac{\sigma_r - \sigma_\theta}{\rho} = 0 \quad (r \le \rho \le r + h) \tag{2.10}$$

where ρ is the radius of a differential spherical layer in the deformed configuration. Consider that for a thin-walled hydrogel balloon with $H \ll R$, when inflated, the tensile stress in the hoop direction σ_θ is orders of magnitude greater than the compressive stress in the thickness direction σ_r. Therefore, the triaxial stress state in the balloon shell can be approximated by an equal-biaxial state, namely,

$$\boldsymbol{\sigma} = \begin{bmatrix} \sigma_\theta & & \\ & \sigma_\theta & \\ & & \sigma_r \end{bmatrix} \approx \begin{bmatrix} \sigma_\theta & & \\ & \sigma_\theta & \\ & & 0 \end{bmatrix} \tag{2.11}$$

Moreover, in a thin-walled hydrogel balloon, σ_θ barely varies over the thickness of the balloon shell. Although σ_r varies from $-P$ to 0 through the thickness, its magnitude is trivial compared to the hoop stress σ_θ. As a result, the value of $(\sigma_\theta - \sigma_r)/\rho$ in Eq. (2.8) can be treated as a constant over the entire thickness of the balloon shell. In the deformed coordinate,

integrating Eq. (2.8) from the pressurized inner surface to the stress-free outer surface of the balloon

$$\int_{-P}^{0} d\sigma_{\mathrm{r}} = 2\int_{r}^{r+h} \frac{\sigma_{\theta}-\sigma_{\mathrm{r}}}{\rho} d\rho \tag{2.12}$$

yields

$$\sigma_{\theta} - \sigma_{\mathrm{r}} = \frac{Pr}{2h} \tag{2.13}$$

Substituting Eq. (2.7) and the relations that $\lambda_{\theta} = r/R$ and $\lambda_{\mathrm{r}} = h/H$ into Eq. (2.11) we can express the inflation pressure P as a function of J and λ_{θ}

$$\frac{P}{kT/v} = \frac{2H}{R} Nv \cdot \left(\lambda_{\theta}^{-1} - \lambda_{\theta}^{-7} J^{2}\right) \tag{2.14}$$

By adopting an approximation of the equal-biaxial stress state, σ_{r} vanishes, so that Eq. (2.6-2) gives

$$J^{-1} Nv(\lambda_{\theta}^{-4} J^{2} - 1) + \left[\log\left(1 - \frac{1}{J}\right) + \frac{1}{J} + \frac{\chi}{J^{2}} - \frac{\mu}{kT}\right] = 0 \tag{2.15}$$

Combining Eqs. (2.12) and (2.13), we establish the mechanical behavior of the hydrogel balloon as a relation between the pressure P and the equilibrium deformation state of the balloon (J and λ_{θ}). Given the thin-walled geometry of the balloon, we can further ignore the variation of J, λ_{θ}, and λ_{r} over the thickness. Therefore, the deformation is homogeneous throughout the balloon shell and can be completely set by two parameters J and λ_{θ} (here J, λ_{r}, and λ_{θ} are not independent since $J=\lambda_{\mathrm{r}}\lambda_{\theta}^{2}$). $\lambda_{\theta}=r/R$ indicates the size of the balloon: a larger

λ_θ corresponds to a further inflated state, i.e., a larger balloon; while J suggests the steady-state water concentration inside the balloon shell, a higher value of J implies more water content is absorbed into the hydrogel network in the current equilibrium frame. When material properties and geometry parameters (Nv, χ, μ, and H/R) are specified, the equilibrium deformation state of the hydrogel balloon can be identified for any given inner pressure P by solving Eqs. (2.12) and (2.13). Representative values of the dimensionless crosslinking density of a hydrogel Nv may vary over 1×10^{-4}~1×10^{-1}, and the Flory-Rehner interaction parameter χ typically ranges 0~1.2 [23]. In the numerical examples below, we will take values, χ=0.2, H/R=0.01, and the chemical potential of the water reservoir μ=0, unless otherwise mentioned.

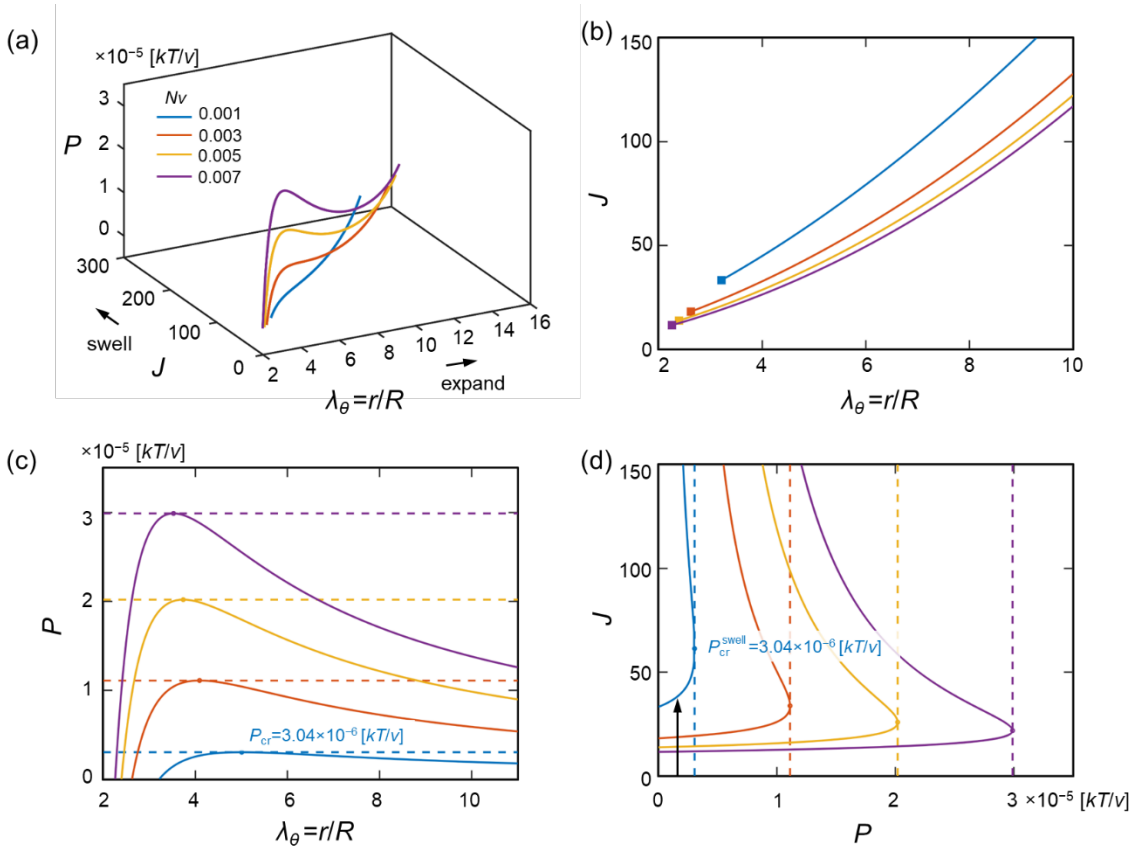

Figure 2.2 Long-term equilibrium deformation of a hydrogel balloon. (a) Three-dimensional curves representing the relation between applied pressure Pv/kT and the equilibrium deformations for hydrogel balloons with different Nv values (Nv=0.001, 0.003, 0.005, and 0.007). (b) J as a function of λ_θ; J and λ_θ are volume strain and hoop stretch with respect to the dehydrated state. Curves start from the free-swelling states (labeled by the squares) for each hydrogel balloon. (c) Normalized pressure Pv/kT as a function of λ_θ. (d) Volume ratio J as a function of applied pressure Pv/kT. In (c) and (d), the maximum pressure permitting the existence of equilibrium deformation and bounded swelling is marked by the dashed lines. The black arrow indicates an equilibrium final deformation when $P < P_{\mathrm{cr}}^{\mathrm{swell}}$.

For different values of Nv (0.001, 0.003, 0.005, and 0.007), Figure 2.2(a) plots the correlation among normalized pressure Pv/kT, volume strain J, and hoop stretch λ_θ as a family of three-dimensional curves, such that the equilibrium response of a hydrogel to applied pressure is readily spotted. Projecting these curves onto J-λ_θ plane, as shown in Figure 2.2(b), J is plotted as a function of λ_θ. Starting from the free-swelling state (marked by the squares, for example), along the inflation process the expansion of the gel balloon is accompanied with a monotonic increase of J, indicating a spontaneous migration of water into the balloon shell as the balloon expands in size. This fact can be ascribed to the equal-biaxial tensile stress state in the hydrogel balloon [84].

Figure 2.2(c) shows the relation between the dimensionless internal pressure Pv/kT and the normalized balloon size r/R. For example, when Nv=0.001 the inflation procedure starts at its free-swelling state λ_0 =3.21. The pressure Pv/kT required by an equilibrium state of the hydrogel balloon continues to increase until a maximum magnitude of 3.04×10^{-6} is reached as the balloon expands to r/R=5.00. Thereafter, the pressure drops for further inflation, indicating the existence of a critical pressure P_{cr} (dashed line) above which no equilibrium deformed states can be obtained. Any quasi-equilibrium inflation process with pressure

above P_{cr} would lead to a continual and infinite growth in the balloon size, resulting in a burst (i.e. fails by rupture) of the hydrogel balloon.

Moreover, the swelling also becomes infinite if the critical pressure is exceeded because of the simultaneous increasing of the swelling ratio and hoop stretch. It is concluded from Figure 2.2(d) that when a pressure P less than P_{cr} is applied, the hydrogel swells and the volume ratio J evolves to a corresponding equilibrium state which can be recognized on the lower half of the curve in Figure 2.2(d), as illustrated by the arrow. For $P<P_{cr}$, the higher the applied pressure, the more the hydrogel swells in its final equilibrium state. In contrast, beyond $P_{cr,}$ the water absorption becomes unbounded due to the lack of equilibrium state. Water molecules will continuously migrate into the hydrogel. Therefore, the critical pressure P_{cr} for equilibrium deformation can be physically interpreted as a threshold for unbounded swelling P_{cr}^{swell}. Such an unbounded swelling will invoke anomalous inflation behavior of the hydrogel balloon, as to be discussed in the following sections.

2.2.2 The instantaneous response of a hydrogel balloon to fast inflation

As aforementioned, the pressurization time scale governs the mechanical responses of a hydrogel balloon. When an internal pressure is applied suddenly ($t_p \ll t_{eq}$), the instantaneous response of the balloon is characterized by a volume-conserving deformation, similar to that of elastomeric materials. In an effort to determine the instantaneous inflation behavior subject to fast inflation, we first consider a homogeneously swollen hydrogel balloon with an arbitrary water concentration $\hat{C}$ inside the balloon shell. Let us denote this swollen state

of the gel balloon as state S($\hat{C}$), referring to its homogeneous water distribution. In state S($\hat{C}$), the corresponding isotropic swelling ratio can be calculated by

$$\hat{\lambda} = \left(1 + v\hat{C}\right)^{\frac{1}{3}} \tag{2.16}$$

Next, we think of a scenario where the boundaries of the balloon become impermeable so that solvent exchange between hydrogel balloon and the reservoir is prohibited. We take the hydrogel shell containing polymer chains and water content as the control volume. Under such an impermeable boundary condition, the balloon shell is therefore turned into a closed system with a constant water concentration remaining at $\hat{C}$. Any subsequent deformation of the hydrogel is thus incompressible and the volume ratio $\hat{J}$ remains fixed. The incompressibility constraint can be written as

$$J = \hat{J} = 1 + v\hat{C} = \hat{\lambda}^3 = \text{const} \tag{2.17}$$

Given the fixed volume ratio, the Helmholtz free energy density defined in Eq. (2.3) becomes $W(\lambda_1, \lambda_2, \lambda_3)=1/2NkT(\lambda_1^2+\lambda_2^2+\lambda_3^2-3)+$const for instantaneous inflation responses. Note that λ_1, λ_2, and λ_3 are defined on the dry state of the hydrogel balloon. To impose the incompressibility condition, let Π denote a Lagrange multiplier and add a term $\Pi(J-\hat{J})$ to the free energy density

$$\mathcal{L}(W, \Pi) = W(\lambda_1, \lambda_2, \lambda_3) + \Pi(J - \hat{J}) \tag{2.18}$$

The nominal stress in principal directions are

$$S_1 = \frac{\partial \mathcal{L}(W,\Pi)}{\partial \lambda_1} = \frac{\partial W(\lambda_1,\lambda_2,\lambda_3)}{\partial \lambda_1} + \Pi\lambda_2\lambda_3 \tag{2.17-1}$$

$$S_2 = \frac{\partial \mathcal{L}(W,\Pi)}{\partial \lambda_2} = \frac{\partial W(\lambda_1,\lambda_2,\lambda_3)}{\partial \lambda_2} + \Pi\lambda_1\lambda_3 \tag{2.17-2}$$

$$S_3 = \frac{\partial \mathcal{L}(W,\Pi)}{\partial \lambda_3} = \frac{\partial W(\lambda_1,\lambda_2,\lambda_3)}{\partial \lambda_3} + \Pi\lambda_1\lambda_2 \tag{2.19-3}$$

and the principal Cauchy stresses are

$$\sigma_1 = \frac{S_1}{\lambda_2\lambda_3} = \frac{\lambda_1}{\hat{J}}\frac{\partial W(\lambda_1,\lambda_2,\lambda_3)}{\partial \lambda_1} + \Pi \tag{2.18-1}$$

$$\sigma_2 = \frac{S_2}{\lambda_1\lambda_3} = \frac{\lambda_2}{\hat{J}}\frac{\partial W(\lambda_1,\lambda_2,\lambda_3)}{\partial \lambda_2} + \Pi \tag{2.18-2}$$

$$\sigma_3 = \frac{S_3}{\lambda_1\lambda_2} = \frac{\lambda_3}{\hat{J}}\frac{\partial W(\lambda_1,\lambda_2,\lambda_3)}{\partial \lambda_3} + \Pi \tag{2.20-3}$$

For the spherical gel balloon undergoes a spherically symmetric deformation, we have $\sigma_1=\sigma_2=\sigma_\theta$, and $\sigma_3=\sigma_r$, therefore,

$$\sigma_\theta - \sigma_r = \sigma_1 - \sigma_3 = \frac{1}{\hat{J}}\left(\lambda_1\frac{\partial W}{\partial \lambda_1} - \lambda_3\frac{\partial W}{\partial \lambda_3}\right) \tag{2.21}$$

Insert Eq. (2.19) into the equation of force balance (Eq. (2.8)) and integrate from the pressurized inner surface to the stress-free outer surface, we arrive at an expression of the pressure in terms of the deformation of the balloon, i.e., the instantaneous mechanical response to fast inflation

$$\frac{P^{vc}}{kT/v} = 2\frac{H^*}{R^*}\frac{Nv}{\hat{\lambda}}\left[(\lambda_\theta^*)^{-1} - (\lambda_\theta^*)^{-7}\right] \tag{2.22}$$

where $H^* = \hat{\lambda}H$ and $R^* = \hat{\lambda}R$ are the thickness and radius of the hydrogel balloon in the initial isotropic swollen state S($\hat{C}$) before inflation, $\lambda_\theta^* = \lambda_\theta/\hat{\lambda}$ is defined as the hoop stretch with regard to the reference state S($\hat{C}$), P^{vc} denotes the applied pressure, and the superscript VC serves as a reminder of the volume-conserving deformation. Note that the pressure-deformation relation depicted by the equation above recovers the well-studied inflation behavior of a balloon made of incompressible Neo-Hookean rubber. Examining the form of Eq. (2.20), if water migration is not allowed, mechanically the hydrogel behaves as a diluted polymeric material. The equivalent initial shear modulus of such a diluted polymeric network is $Nv/\hat{\lambda}$ (dimensionless). Compared to that of the dry state, the swollen network is softened by a factor of $1/\hat{\lambda}$. Additionally, at $\lambda_\theta^* = 1.383$, the pressure reaches a maximum value of

$$\frac{P_{\text{cr}}^{\text{vc}}}{kT/v} = 1.24\frac{H^*}{R^*}\frac{Nv}{\hat{\lambda}} \tag{2.23}$$

This maximum pressure as well constitutes a critical value that the balloon can sustain in a volume-conserving inflation. For $P < P_{\text{cr}}^{\text{vc}}$, the inflation is steady and the applied pressure carries the balloon to a deformed state that is determined by Eq. (2.20). Whereas if $P \geq P_{\text{cr}}^{\text{vc}}$, the balloon grows unstably, leading to a rupture. Since such a failure is not associated with water migration, when the applied load satisfies the failure criterion, it occurs in an instantaneous fashion. Furthermore, Eq. (2.21) reveals that this critical pressure $P_{\text{cr}}^{\text{vc}}$ is dependent on the isotropic swelling ratio $\hat{\lambda}$ and thus the water concentration $\hat{C}$: at a specific concentration, there exists a corresponding critical pressure $P_{\text{cr}}^{\text{vc}}(\hat{C})$ beyond which burst occurs. This conclusion becomes very useful when interpreted equivalently as follows: the

criterion to predict whether an instant burst happens or not is whether the applied pressure exceeds $P_{\mathrm{cr}}^{\mathrm{vc}}(\hat{C})$, which is defined by the water concentration $\hat{C}$ at the current time instance. Particularly, when an inner pressure is suddenly applied to an initially free-swelling hydrogel balloon, the mechanical response of the hydrogel balloon starts with an instantaneous and volume-conserving deformed state. If the load is supercritical, namely, $P \geq P_{\mathrm{cr}}^{\mathrm{vc}}(C_0)$, the balloon fails instantaneously by burst. We refer to such a failure mechanism as the instant burst of a hydrogel balloon because it takes place immediately upon the pressurization. The instant burst threshold $P_{\mathrm{cr}}^{\mathrm{ins}}$ of a free-swelling hydrogel balloon is identical to $P_{\mathrm{cr}}^{\mathrm{vc}}(C_0)$.

Lastly, for hydrogel balloons with different water concentrations, the critical pressure for instant burst is a decreasing function of the homogeneous swelling ratio. According to Eq. (2.21), the critical pressure is inversely proportional to $\hat{\lambda}$, hence the gel balloon becomes more susceptible to volume-conserving burst if it has more water taken up by the polymeric network. Compare two geometrically identical gel balloons A and B, if $C_{\mathrm{A}} > C_{\mathrm{B}}$, $P_{\mathrm{cr}}^{\mathrm{vc}}(C_{\mathrm{A}}) < P_{\mathrm{cr}}^{\mathrm{vc}}(C_{\mathrm{B}})$.

2.3 Delayed burst of a hydrogel balloon

It is well known that the time-dependent mechanical behavior is one of the most fundamental characteristics of hydrogel materials. The time-dependency may either arise due to the intrinsic viscoelasticity of the constituent cross-linked polymer chains or stem from the poroelasticity that take accounts for the molecular interaction between the polymer network and the surrounding solvent molecules [85], [86]. In the present study,

we assume the polymer network is ideally elastic and ascribe the time-dependency to the water transportation process through the hydrogel. As aforementioned, mechanical response of a hydrogel subjected to suddenly applied mechanical loads is characterized by an incompressible deformation, followed by a long-term time-dependent deformation towards equilibrium state due to water transportation. In this section, we will systematically study the evolution process of the hydrogel balloon deformation from the instant response state towards the long-term equilibrium state.

2.3.1 Mechanism of the delayed burst procedure of a hydrogel balloon

When a free-swelling gel balloon is subject to a fast pressurization, even though the water diffusion between the hydrogel and water reservoir is allowed, the immediate response is dominated by the incompressible inflation: if $P \geq P_{\mathrm{cr}}^{\mathrm{ins}} = P_{\mathrm{cr}}^{\mathrm{vc}}(C_0)$, instant burst occurs, whereas if $P < P_{\mathrm{cr}}^{\mathrm{ins}} = P_{\mathrm{cr}}^{\mathrm{vc}}(C_0)$, the instantaneous deformation is given by Eq. (2.20) with $\hat{J} = J_0$ and $\hat{\lambda} = \lambda_0$, namely

$$\frac{P}{kT/v} = 2\frac{H}{R}\frac{Nv}{\lambda_0}[(\lambda_\theta')^{-1} - (\lambda_\theta')^{-7}] \tag{2.24}$$

where λ_0 is the free-swelling stretch ratio sketched in Figure 2.1(b) and thus $\lambda_\theta' = \lambda_\theta/\lambda_0$ denotes the hoop stretch relative to the free-swelling state.

However, because of the migration of water molecules, the gel balloon does not stay in this instantaneous deformed state but keeps evolving to equilibrate with the solvent and mechanical loads. Driven by the biaxial stretch state in the hoop directions, the surrounding water molecules in the solvent reservoir start to migrate into the balloon shell. The stiffness

of the hydrogel is effectively reduced as the hydrogel balloon swells, which in turn leads to a further expansion under a constant interior pressure. According to Section 2, depending on the applied pressure, subsequent to the instant deformation, the balloon will either arrive at an equilibrium final state through a gradual procedure of simultaneous swelling and expansion, or, in another case, experience an unbounded water intake. For example, if pressure Pv/kT=2.90×10^{-6} is suddenly pumped into the balloon (Nv=0.001, H/R=0.01), since the load is less than the critical pressure for unbounded swelling $P_{\mathrm{cr}}^{\mathrm{swell}}v/kT = 3.04 \times 10^{-6}$(see Figure 2.2(c) and (d)), eventually the hydrogel balloon will arrive at an equilibrium final state with λ_{eq}=4.39 and J_{eq}=51.06, which is determined by solving Eqs. (2.12) and (2.13). However, if the hydrogel is subjected to a supercritical pressure Pv/kT=3.34×10^{-6}, the balloon will expand and imbibes water continuously in an unbounded fashion.

The subsequent time-dependent evolution procedure in response to a fast pressurization is explained by Figure 2.3. The green curve in Figure 2.3(a) plots the incompressible response of the balloon at water content C_0 corresponding to the free-swelling state $\lambda_0=R_0/R$=3.21. When a subcritical pressure of Pv/kT=2.90×10^{-6} is applied, following the green curve, the balloon expands immediately from the initial free-swelling state (denoted by point 1 in Figure 2.3(a)) λ_0 =3.21 at $J_0=\lambda_0^3$=33.23 to the instantaneous deformed state $\lambda_\theta=r/R$=3.64 at the same volume ratio $J=J_0$ (point 2). During the expansion, the radius grows to 1.13 times of its initial size. Soon afterwards, a small amount of water diffuses into the gel balloon shell, causing the water content to increase to $C_0+\Delta C$ and the volume ratio to $J_0+\Delta J$. In response to the water migration, the hydrogel balloon expands further and evolves to a new

deformed state, which can be determined by Eq. (2.20) at the water concentration of $C_0+\Delta C$. For instance, when water continues to migrate into the gel so that J=40, the deformation of the balloon can be found at the intersection (denoted by point 3) of the volume-conserving response curve with J=40 and the horizontal line $Pv/kT=2.90\times10^{-6}$. Via a sequence of these intervening states, the hydrogel balloon evolves towards its equilibrium final state. Under a constant applied pressure, the state of the hydrogel balloon progresses consecutively across a family of incompressible P-λ_θ curves with ascending J, from the starting volume ratio $J=J_0$ and terminates at the final equilibrium volume ratio J_{eq}=51.06 (point 4).

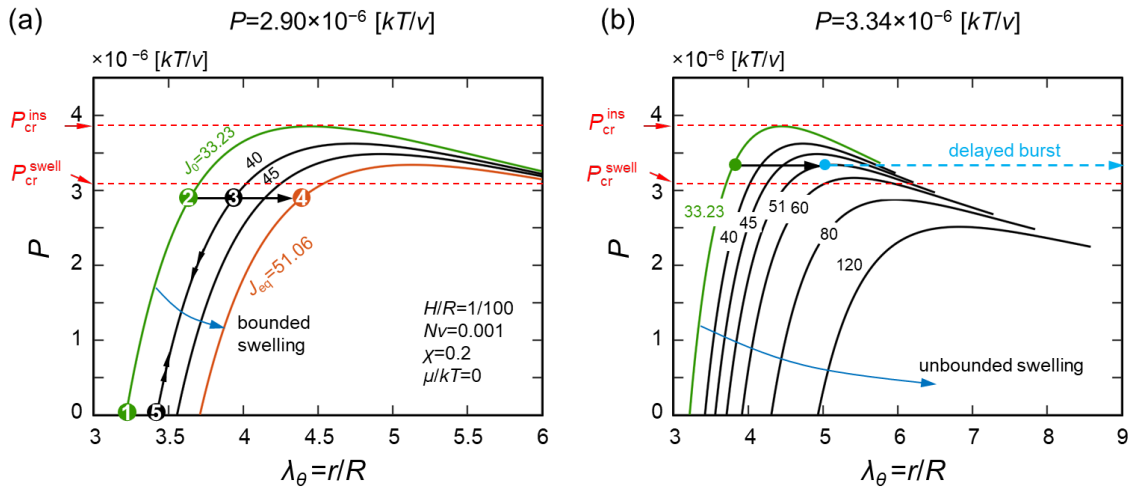

Figure 2.3 Mechanism of the delayed burst of a hydrogel balloon. (a) Evolution of the intermediate states during inflation when a subcritical pressure of $Pv/kT=2.90\times10^{-6}$ is applied to the balloon. Compared to case (b) when the balloon is subject to a supercritical pressure of $Pv/kT=3.34\times10^{-6}$, delayed burst occurs as a consequence of the unbounded swelling. ②③④ in (a) represents progressively deformed states in response to the applied pressure as the hydrogel shell continues to swell.

To illustrate that the volume-varying evolution of the gel balloon indeed passes through these intermediate states determined by the family of volume-conversing curves, let us consider an unloading process: at the moment J=40, the boundaries of the gel balloon abruptly loses its permeability, then we drop the pressure. Fully unloaded, the balloon rests at a uniformly swollen state $\lambda_\theta=\lambda_r=40^{1/3}$ marked by point 5. Lastly, we bring the pressure back to the previous value, the reloading process follows the double arrow from point 5 to point 3 on the incompressible response curve. Therefore, point 5 and 3 is connected by a constant-volume process with J=40, in other words, the intermediate state denoted by point 3 can be identified as the intersection of the incompressible response curve and the applied pressure.

In contrast, if the applied inner pressure is above the critical threshold $P_{\mathrm{cr}}^{\mathrm{swell}}\nu/kT = 3.04\times10^{-6}$, the gel balloon will expand unstably, rather than come to a standstill at a final equilibrium state. Whereas the balloon expands and the hydrogel shell imbibes more water content, the critical pressure for instant burst monotonically decreases as a result of the reduced shear modulus of the diluted polymeric network (Eq. (2.21)); and the critical pressure for instant burst eventually falls below the applied pressure. As Figure 2.3(b) shows, under an applied pressure of 3.34×10^{-6}, starting from the initial volume ratio $J=J_0$=33.23, the hydrogel continuously swells to J=51.06 over time, and the corresponding critical pressure for burst decreases from $P_{\mathrm{cr}}^{\mathrm{ins}}\nu/kT = P_{\mathrm{cr}}^{\mathrm{vc}}(J=J_0)\nu/kT = 3.86\times10^{-6}$ to the value of the applied pressure, i.e. 3.34×10^{-6}. As a result, the applied pressure of 3.34×10^{-6} triggers the instant burst of the hydrogel balloon when the volume ratio has increased to J=51.06 by water absorption. Compared to the instant failure which occurs

immediately upon the pressurization of a free-swelling hydrogel balloon, such burst phenomenon does not take place until a span of time has elapsed after the Pv/kT=3.34×10^{-6} is applied. The delayed time period is attributed to the time-dependent swelling procedure during which the volume ratio J continuously increases from 33.23 to 51.06 and the critical pressure for instant burst $P_{\mathrm{cr}}^{\mathrm{vc}}(C)$ reduces to the level of the applied pressure $P_{\mathrm{cr}}^{\mathrm{vc}}(C) = P$. The delayed burst of a hydrogel balloon is so named because the onset of it is postponed. Nevertheless, the occurrence of burst itself is instantaneous, as long as the water concentration in the hydrogel shell registers a critical level C such that $P_{\mathrm{cr}}^{\mathrm{vc}}(C) = P$. As analyzed above, unbounded swelling and the decreasing critical pressure $P_{\mathrm{cr}}^{\mathrm{vc}}(C)$ conspire to cause the delayed burst phenomenon. By analogy with the notion of damage mechanics, at a constant pressure load, the capability of the balloon to resist burst failure decays over time as the hydrogel swells, indicating some form of "degradation" is accumulated by virtue of unlimited water migration.

As the delayed burst is a direct consequence of the unbounded swelling, the critical pressure for unbounded swelling $P_{\mathrm{cr}}^{\mathrm{swell}}\nu/kT = 3.04 \times 10^{-6}$ also defines a critical threshold for delayed burst: when a normalized applied pressure $P < P_{\mathrm{cr}}^{\mathrm{swell}}$, the hydrogel balloon will takes in water and eventually equilibrates with the pressure load and the solvent environment, no burst occurs; whereas if a normalized applied pressure$P_{\mathrm{cr}}^{\mathrm{swell}} \leq P < P_{\mathrm{cr}}^{\mathrm{ins}}$ is applied, delayed burst will occur.

The intrinsic time scale of the delayed burst can be estimated by the solvent diffusion dynamics, $t \sim H_0^2/D$. At room temperature, diffusivity D can be approximated by the self-

diffusivity of water molecules, $D \approx 1\times10^{-9}\mathrm{m^2s^{-1}}$ [68], [83]. For a hydrogel balloon with an initial thickness H_0=1mm, the time required by the water molecule to migrate into the balloon shell is on the order of 1000s, which dictates the characteristic time for the delayed burst. Here, we analyze the delayed burst of a hydrogel balloon by investigating the evolution of the intermediate states from the instant mechanical response of the balloon towards its long-term equilibrium state. A full account of the time-dependent process resorting to directly solving solvent transportation kinetics is beyond the scope of the present paper.

2.3.2 *Energy evolution associated with the delayed burst*

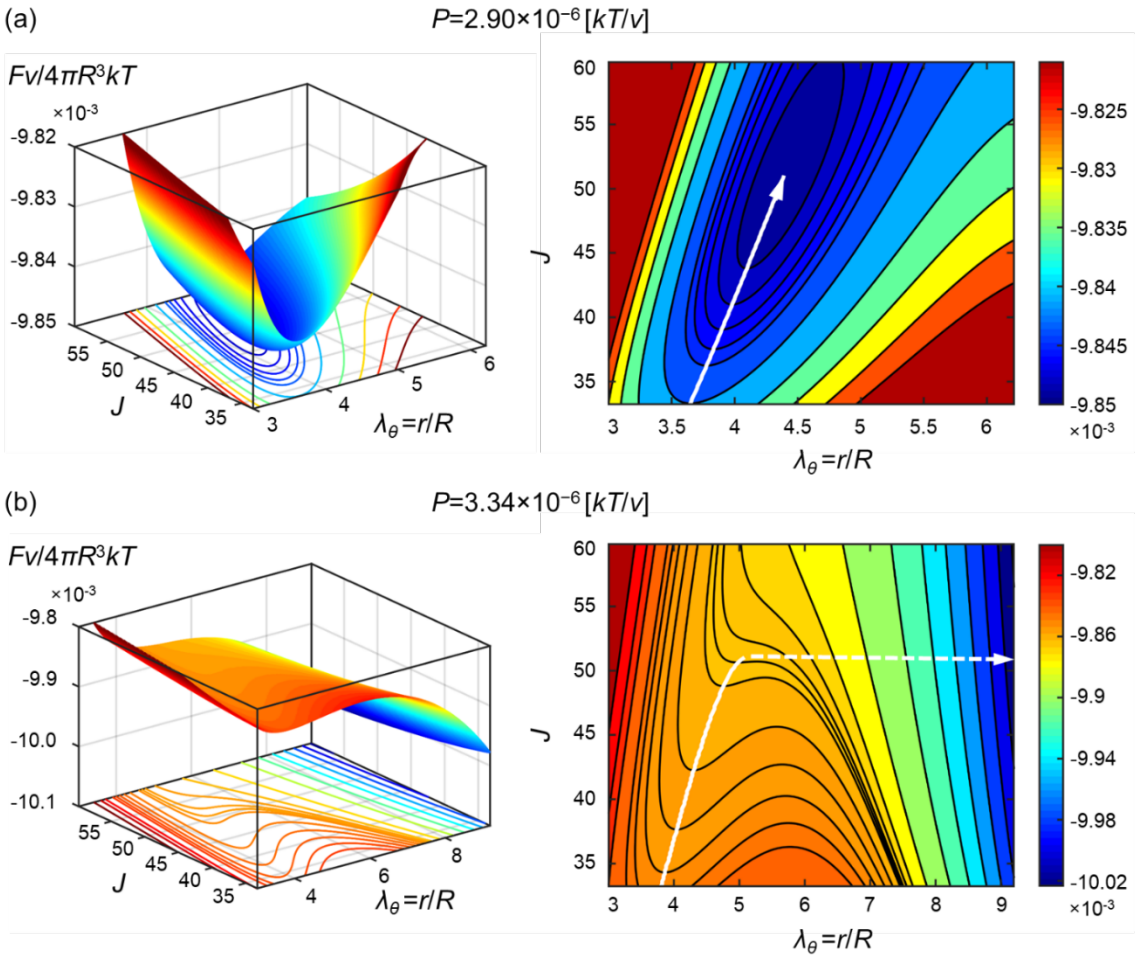

Figure 2.4 Free energy surface and contour at an applied pressure (a) Pv/kT=2.90×10^{-6} and (b) Pv/kT=3.34×10^{-6}. The solid white trajectory tracks the minimum energy state of the system as the balloon swells. The white dashed line indicates the delayed burst.

The distinction between equilibrium inflation and delayed burst is also reflected on the free energy landscape. The total free energy of the system is composed of the strain energy of the hydrogel balloon and the potential energy due to the applied pressure. Therefore, the free energy is a function of the applied pressure and the deformation of the balloon

$$\frac{F(J,\lambda_\theta|P)}{\left(\frac{kT}{v}\right)\cdot 4\pi R^3} = \frac{H}{2R}Nv\left(2\lambda_\theta^2 + J^2\lambda_\theta^{-4} - 3 - 2\log J\right) - \frac{H}{R}\left\{\left[(J-1)\log\left(\frac{J}{J-1}\right) + \frac{\chi}{J}\right] + (J-1)\right\} - \frac{1}{3}\frac{P}{\frac{kT}{v}}\lambda_\theta^3 \quad (2.25)$$

Figure 4 plots the system free energy in J-λ_θ space at (a) a subcritical pressure for delayed burst Pv/kT= 2.90×10^{-6} and (b) a supercritical pressure 3.34×10^{-6}, respectively. When Pv/kT=2.90×10^{-6} ($P < P_{\mathrm{cr}}^{\mathrm{swell}}$), as shown in Figure 2.4(a), on the free energy surface there exists a local minimum representing the final equilibrium deformation. In the energy contour plot (Figure 2.4(a) right panel), the starting point of the white curve denotes the instantaneous deformation state (point 2 in Figure 2.3(a)), while the terminal point represents the final equilibrium deformation state (point 4 in Figure 2.3(a)). In between, the path connecting the instantaneous response and the final deformation represents the intervening states of the hydrogel balloon. Starting from the instantaneous inflated state, the hydrogel balloon keeps absorbing water with volume ratio J increasing. Since only the water migration requires time whereas the radial expansion of the balloon occurs promptly, at any increased value of J, the corresponding hoop stretch λ_θ=r/R should vary to minimize the free energy. The intervening states are thus identified by minimizing the free energy at a given J. Consequently, in the J-λ_θ space, the inflated hydrogel balloon leaves a white path tracing the evolution of its intermediate states. Driven by the minimization of the total free energy of the system, i.e. a hydrogel balloon under pressure Pv/kT= 2.90×10^{-6} and immersed in water, the balloon continues to swell and expand along the white path until the energy comes to a minimum, and the deformation stops at the final equilibrium state marked by the end of the white arrow.

As shown in Figure 2.4(b), the free energy landscape at a supercritical pressure of Pv/kT=3.34×10^{-6} ($P > P_{\mathrm{cr}}^{\mathrm{swell}}$) exhibits a lack of local minimum. The first stage of the energy minimization starts from the instantaneous response state at J=J_0=33.23 (corresponding to the green dot in Figure 2.3(b)) to the onset of the delayed burst (end of the white solid line, J=51.06, corresponding to the red dot in Figure 2.3(b)), during this process the hydrogel balloon slowly absorbs water and grows in size over time. At the turning point where J=51.06, the energy minimum no longer presents, there are actually multiple paths to further minimize the energy. However, the dashed line represents the only way which is not associated with water migration, in other words， it constitutes the fastest path to perform energy minimization that requires no time. Therefore, at J=51.06 the system seeks to minimize the energy by a pure size expansion (burst), as the dashed line indicates.

2.3.3 Phase diagram of the inflation of a hydrogel balloon

Furthermore, we can prove that, for an initially free-swelling hydrogel balloon shown in Figure 2.1(b), the critical pressure for instant burst $P_{\mathrm{cr}}^{\mathrm{ins}}$ is always greater than that for delayed burst $P_{\mathrm{cr}}^{\mathrm{swell}}$, i.e. $P_{\mathrm{cr}}^{\mathrm{ins}} > P_{\mathrm{cr}}^{\mathrm{swell}}$ (see Appendix A). For instance, in the previous numerical example, $P_{\mathrm{cr}}^{\mathrm{ins}} v/kT = 3.86 \times 10^{-6}$ is greater than $P_{\mathrm{cr}}^{\mathrm{swell}} v/kT = 3.04 \times 10^{-6}$, as shown in Figure 2.3(a) and (b). Hence, any applied pressure P may fall into one of three intervals, which are associated with three distinct response. If $P \geq P_{\mathrm{cr}}^{\mathrm{ins}}$, the gel balloon bursts immediately upon the load; when $P < P_{\mathrm{cr}}^{\mathrm{swell}}$, the balloon first deforms to an instantaneous state then swells and expands further to attain an equilibrium state; if $P_{\mathrm{cr}}^{\mathrm{swell}} \leq P < P_{\mathrm{cr}}^{\mathrm{ins}}$, delayed burst occurs, namely the hydrogel balloon expands gradually

for a span of time and then burst suddenly. Figure 2.5 delineates a map for these three situations in the parameter space of *P*-*Nv*. These two pressure limits $P_{\mathrm{cr}}^{\mathrm{ins}}$ and $P_{\mathrm{cr}}^{\mathrm{swell}}$ define the boundary of a new region corresponding to delayed burst failure mode. Owing to its latent nature, such delayed failure mode is more detrimental to the application of thin-walled hydrogel structures.

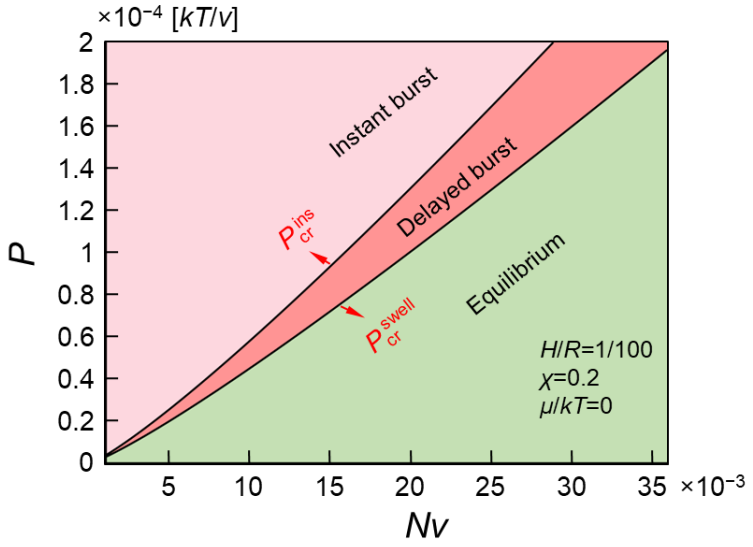

Figure 2.5 Failure mode map of the inflation of a hydrogel balloon delineating three regions in the parameter space of *P*-*Nv*: instant burst, delayed burst, and equilibrium inflation.

Recall that the material property *Nv* represents the crosslinking density and the initial stiffness of the polymer network. Both critical pressures for instant burst $P_{\mathrm{cr}}^{\mathrm{ins}}\nu/kT$ and for delayed burst $P_{\mathrm{cr}}^{\mathrm{swell}}\nu/kT$ scale up with stiffness *Nv*. Moreover, as *Nv* increases, the pressure window associated with the delayed burst becomes larger, because of the increasing difference between $P_{\mathrm{cr}}^{\mathrm{ins}}$ and $P_{\mathrm{cr}}^{\mathrm{swell}}$.

2.4 Delayed burst of a thick hydrogel balloon

In other cases [82], [87]–[90], the thickness of the hollow hydrogel structure may not be essentially small compared to other dimensions, for example, the inner radius of the hollow space. Especially, if the thickness is much larger than the inner radius, the hollow space becomes a cavity defect in a hydrogel. Under pressurization, these structures and defects may be as well susceptible to instant burst and delayed burst. In this section, we investigate the effect of the balloon thickness on the critical pressure for delayed burst.

When the balloon has a finite thickness, the variation of the quantities in the radial direction needs to be accounted for. The stretches λ_θ and λ_r, water concentration C, volume ratio J, radial stress σ_r, and hoop stress σ_θ all vary along the thickness direction. For a special case where the material is incompressible, this boundary value problem represented by Eq. (2.10) can be integrated analytically,

$$\frac{P^{\mathrm{vc}}}{kT/v} = Nv\left\{\left(\frac{B^3}{B^3-A^3+a^3}\right)^{\frac{1}{3}}\cdot\left[\frac{5B^3-4A^3+4a^3}{2B^3-2A^3+2a^3}\right]-\frac{1}{2}\left(\frac{A}{a}\right)^4-2\frac{A}{a}\right\} \tag{2.26}$$

where A and B are the inner and outer radii of the hydrogel balloon in the free swelling state (as labeled in Figure 2.6(a)), respectively, and a is the inner radius in the deformed state. Before deformation, the thickness of the balloon is $H=B-A$. As previously discussed, if the time scale of interest is much smaller than the characteristic time of the water diffusion, the hydrogel behaves as an incompressible hyperelastic material. Thus, Eq. (2.24) explicitly gives the response of a thick hydrogel balloon under fast inflation.

Whereas for hyperelastic materials exhibiting compressible behavior, as the quasi-equilibrium deformation during slow pressurization of a hydrogel balloon, the volume-conserving assumption is invalid. Analytical solutions of Eq. (2.10) are restricted to materials whose constitutive laws take special forms [91]–[95] or limited to asymptotic approximations [96]. In general, solving the boundary value problem described by Eq. (2.10) necessitates numerical approaches such as finite difference scheme (for example, shooting method) or alternatively finite element method (FEM) [97], [98]. Here, we examine the slow pressurization procedure by using commercial FEM package ABAQUS. Because the governing equation of the problem Eq. (2.10) possesses spherical symmetry, it is adequate to merely consider a differential volume that is cut out from the hollow sphere by planes $\Theta=\theta$, $\Theta=\theta+\delta\theta$, $\Phi=\varphi$, $\Phi=\varphi+\delta\varphi$, $\rho=A$, and $\rho=B$, as Figure 2.6(a) shows. Note that ABAQUS does not directly supply one-dimensional spherically symmetric element. However, this boundary value problem can be alternatively modeled by using two-dimensional axisymmetric quadrilateral elements under special treatments that ensure spherically symmetric behavior. Since the integration in one of the hoop directions Φ is already taken care of by the formation of axisymmetric elements, once we apply suitable boundary conditions to ensure the symmetry in another hoop direction Θ, the spherical symmetry is guaranteed. Therefore, by suppressing the hoop direction freedom, nodes are only free to displace in the radial direction. Furthermore, the radial displacement of nodes on the top side is constrained to be the same as the corresponding nodes on the bottom side, namely $u_{\text{top}}^{(i)} = u_{\text{bottom}}^{(i)}$, where ($i$) labels the node number. Now the Θ direction is discretized by taking advantage of symmetry. Under such a treatment, the two-dimensional model in Figure 2.6(b) becomes equivalent to one-dimensional spherically symmetric. In

the following analysis, we use $\delta\theta$=0.5°~1°. Mesh convergence analysis is also performed in order to ensure the accuracy of the calculation when A is comparatively miniature to H. In the next step, equilibrium pressure P is recorded as a function of the prescribed displacement of the inner surface a.

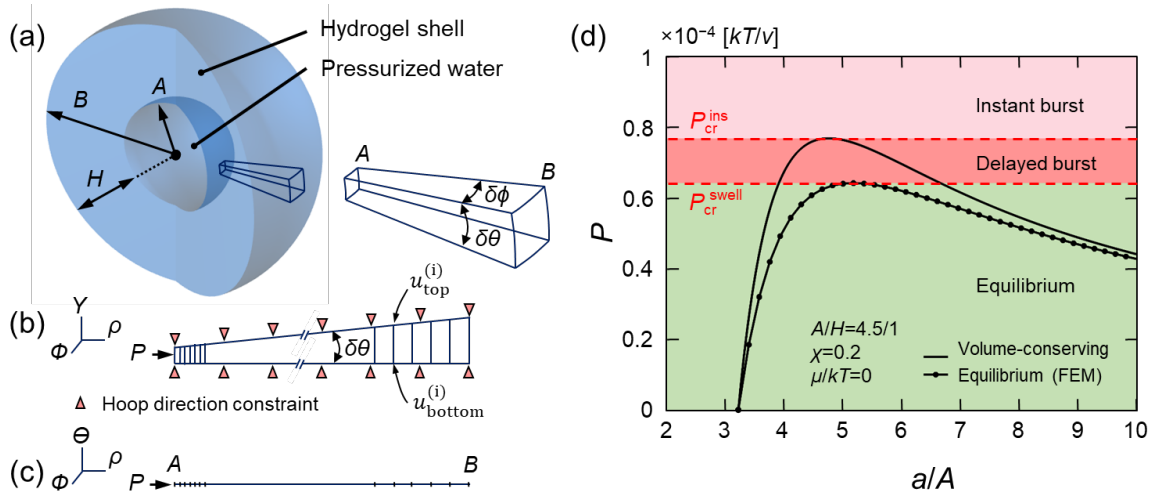

Figure 2.6 Finite element analysis for the internal inflation of a thick hydrogel balloon. (a) Geometry of a balloon with finite thickness $H = B-A$. A and B are undeformed inner and outer radii, respectively. Schematic of the (b) two-dimensional equivalent FEM representative of the (c) actual one-dimensional model. (d) Normalized pressure Pv/kT as a function of normalized inner surface deformation a/A for instant (volume-conserving) and slow (equilibrium) inflation of a thick balloon. (Hydrogel property Nv=0.001, and balloon geometry A/H=4.5/1).

Figure 6(d) compares the final equilibrium deformation to the instant (volume-conserving) response of a thick hydrogel balloon with ratio A/H=4.5/1. The equilibrium inflation response is obtained from FEM, and the instant inflation response is plotted from Eq. (2.24). Similarly to a thin balloon, the inflation of a thick balloon is also divided into three regions. An applied pressure greater than the peak value of the fast inflation ($P_{\mathrm{cr}}^{\mathrm{ins}}$) causes instant burst, while a pressure smaller than the maximum pressure on slow inflation curve

($P_{\mathrm{cr}}^{\mathrm{swell}}$) results in an equilibrium deformation. The peak pressure for fast inflation is higher than that of the slow inflation, carving out a pressure interval for delayed burst to occur.

The predominance of the delayed burst phenomenon can be represented by the difference between the two pressure limits $P_{\mathrm{cr}}^{\mathrm{ins}}$ and $P_{\mathrm{cr}}^{\mathrm{swell}}$. Figure 2.7 shows the percentage difference $(P_{\mathrm{cr}}^{\mathrm{ins}} - P_{\mathrm{cr}}^{\mathrm{swell}})/P_{\mathrm{cr}}^{\mathrm{ins}} \times 100\%$ for hydrogel balloons with a series of thicknesses from A/H=100 to A/H=0.01. As the thickness increases, the pressure difference is reduced from a highest value of 22% to a minimum value of 2%. The delayed burst phenomenon is more difficult to observe when the wall thickness increases. As A/H approaches 0, the critical pressures for instant burst and unbounded swelling tend to merge, and the delayed burst region diminishes on the failure map, indicating that the delayed cavitation becomes less pronounced for an infinitesimal cavity inside the hydrogel body. Ultimately, it might be expected that the importance of delayed burst diminishes as the dimension of inner surface diminishes, and while this is the case, instantaneous failure may become the only prevailing mode of cavitation in hydrogels. The corresponding critical pressure is $2.5Nv$, below which the long-term equilibrium state exists, as predicted by taking the limit of Eq. (2.24) with $B \gg A$ and $a \gg A$.

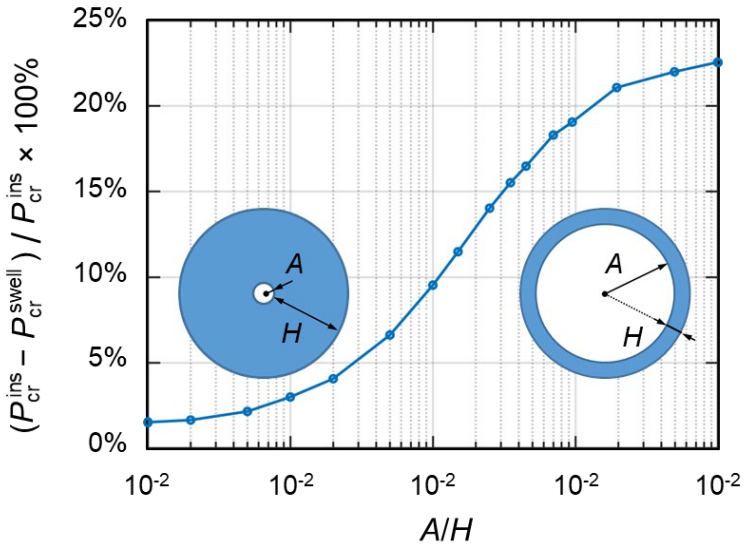

Figure 2.7 Percentage difference between the critical pressures for instant inflation and unbounded swelling $(P_{\mathrm{cr}}^{\mathrm{ins}} - P_{\mathrm{cr}}^{\mathrm{swell}})/P_{\mathrm{cr}}^{\mathrm{ins}} \times 100\%$, for hydrogel balloons with various thicknesses.

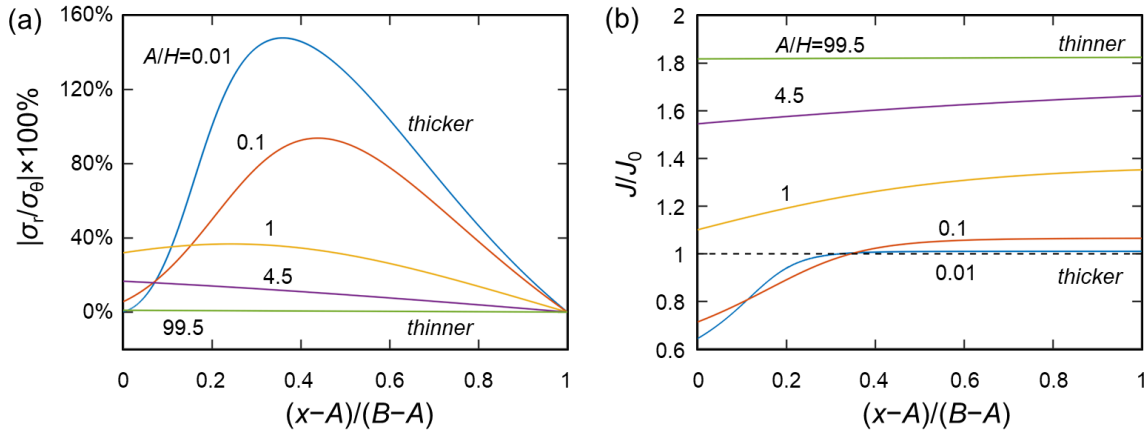

Figure 2.8 Distribution of (a) stress component ratio $|\sigma_{\mathrm{r}}/\sigma_{\theta}|$ and (b) relative volume ratio J/J_0 at critical pressure $P_{\mathrm{cr}}^{\mathrm{swell}}$ on equilibrium inflation curve for hydrogel balloons with various thicknesses.

In contrast to thin balloons, under inner pressurization, the stress state in a thick balloon deviates from an equal biaxial state. Figure 2.8(a) plots the ratio between the radial stress

and the hoop stress $|\sigma_r/\sigma_\theta|$ at critical pressure P_{cr}^{swell}. As the thickness increases, the radial stress is not negligible anymore when compared with the hoop stress. For a small pressurized cavity inside the hydrogel, between the inner surface and the outer surface, the compressive stress in the radial direction may exceed the tensile stress in the hoop direction. The dissimilarity in the stress states results in distinct distributions of water content and relative volume ratio J/J_0. As Figure 2.8(b) shows, the water absorption declines as the balloon becomes thicker. In the neighborhood of the inner surface of a small pressurized cavity, the hydrogel even loses water content to the environment. The loss of solvent effectively stiffens the hydrogel, elevates the critical pressure for slow inflation, and consequently, narrows the pressure range for delayed burst or cavitation in a thick hydrogel balloon.

2.5 Appendix of Chapter 2

First, we show that any equilibrium state determined by Eq. (2.12) is as well located on the incompressible response curve. For an arbitrary equilibrium state of the balloon, let us denote the volume ratio as

$$J = \hat{J} = \hat{\lambda}^3 \tag{A.27}$$

inserting Eq. (2.23) into (2.12) gives,

$$\frac{P}{kT/v} = \frac{2H}{R} Nv \cdot \left(\lambda_\theta^{-1} - \lambda_\theta^{-7}\hat{\lambda}^6\right) = \frac{2(\hat{\lambda}H)}{(\hat{\lambda}R)} \frac{Nv}{\hat{\lambda}} \left(\left(\frac{\lambda_\theta}{\hat{\lambda}}\right)^{-1} - \left(\frac{\lambda_\theta}{\hat{\lambda}}\right)^{-7}\right) \tag{A.28}$$

which recovers Eq. (2.20), namely the instantaneous response of a gel balloon at a uniform initial swelling ratio $\hat{\lambda}$. Therefore, we prove that any equilibrium state can also be achieved

through a volume-conserving process at the corresponding volume ratio J. Among all these equilibrium states, the critical pressure for unbounded swelling P_{cr} corresponds to one, (which is actually the equilibrium state at the highest water content or the highest volume ratio).

As J increases from J_0 to J_{eq}, the critical pressure for instant burst at the initial free swelling state $P_{\mathrm{cr}}^{\mathrm{inc}}$ is actually the highest pressure on all the instant response curves at different values of J. Therefore, the limit pressure for instant burst $P_{\mathrm{cr}}^{\mathrm{inc}}$ is always greater than that for the unbounded swelling, i.e. $P_{\mathrm{cr}}^{\mathrm{inc}} > P_{\mathrm{cr}}$.

2.6 Summary of Chapter 2

From the aspect of water migration, this paper investigates the delayed burst phenomenon as a new failure mechanism during the inflation of a hydrogel balloon. In contrast to instantaneous burst, the mechanism of the delayed burst is attributed to an unbounded swelling process subsequent to the instant deformation upon the load. As the hydrogel swells, the instantaneous burst critical pressure of the inflated balloon reduces gradually to the applied inner pressure, triggering the burst. This new failure mode is termed as the delayed burst to signify the fact that the onset of the burst is delayed by a time period for water molecules to migrate into the hydrogel balloon shell. The process of delayed burst is understood by tracking the evolving mechanical response of swelled hydrogel balloon and as well by minimizing the free energy profile of hydrogel balloon subjected to subcritical pressures.

Moreover, we identify the critical pressure for instantaneous burst and delayed burst, along with the three inflation modes of an initially free-swelling hydrogel balloon: If $P \geq P_{\mathrm{cr}}^{\mathrm{ins}}$, the gel balloon bursts immediately in response to the applied inner pressure; when $P_{\mathrm{cr}}^{\mathrm{swell}} \leq P < P_{\mathrm{cr}}^{\mathrm{ins}}$, delayed burst occurs, namely， the hydrogel balloon expands gradually for a span of time and then burst suddenly; if $P < P_{\mathrm{cr}}^{\mathrm{swell}}$, the balloon first deforms to an instantaneous state upon the load, followed by attaining an equilibrium state via bounded swelling and expansion. We further delineate a map of the three different inflation modes of a thin-walled hydrogel balloon in the parameter space of P and Nv: equilibrium inflation ($P < P_{\mathrm{cr}}^{\mathrm{swell}}$), delayed burst ($P_{\mathrm{cr}}^{\mathrm{swell}} \leq P < P_{\mathrm{cr}}^{\mathrm{ins}}$) and instantaneous burst ($P \geq P_{\mathrm{cr}}^{\mathrm{ins}}$). The delayed burst is counterintuitive and is even more detrimental than the instantaneous burst because of its latent nature.

Lastly, we extend our discussion to examine the delayed burst in thick hydrogel balloons by using finite element method. We find that the delayed burst phenomenon becomes less pronounced for a thick balloon as the pressure window evoking such a failure mode narrows down. Particularly, the delayed cavitation is predicted to become nearly irrelevant for a small vacancy defect enclosed in the hydrogel material. We limit our scope within the geometry of spherical balloons, however, it is believed that this research may also shed light on the delayed failure of other thin-walled hydrogel structures that find extensive applications in soft actuators, soft robots, and biomedical devices.

Chapter 3: Dielectric-Elastomer-Based Capacitive Force Sensing with Tunable and Enhanced Sensitivity[2]

Designing capacitive force sensors with enhanced and *in situ* tunable sensitivity is important in many fields such as robotic grippers but has been proved to be challenging. Existing capacitive force sensors mainly rely on ingenious but complex structural designs, imposing tremendous difficulty in fabrication and usually featuring a fixed sensitivity. In this chapter, we present a facile design of capacitive tactile force sensor endowed with tunable and enhanced resolution by utilizing the electro-mechanically responsive dielectric elastomer as the sensing medium. Dielectric elastomer exhibits tunable mechanical properties when subject to voltage and pre-stretch: increasing voltage and pre-stretch level leads to a more compliant response to the external pressure. Effectively, the sensitivity of the DE sensor can be continuously increased up to over one order of magnitude by properly exerting voltage and pre-stretch to the DE tactile sensor.

3.1 Introduction

In the daily delivery of multifunctional tasks such as touching, griping, pushing, and pulling, human hands count on the tactile feedback from the nerve endings, which are densely populated on palm skin[99], [100]. These nerve endings, working collaboratively to form a sensory network, feature a capability of detecting tactile forces across a range of several orders of magnitude with correspondingly appropriate sensitivities[101], [102].

[2] The main findings in this chapter have been published as J. Cheng, Z. Jia, T. Li, Dielectric-elastomer-based capacitive force sensing with tunable and enhanced sensitivity, *Extreme Mechanics Letters* 21, 49-56 (2018).

Recent research has suggested that human hands are sufficiently sensitive to perceive the haptic interaction with a nanoscale-featured surface[103], whereas in the other extreme scenarios it also sustains force of a few hundred pounds when lifting a barbell set. As an artificial analog of human skin, smart skin is a micro-electro-mechanical system (MEMS) that senses the force of different magnitudes and accurately tracks the force variation. Although the large-range or multi-resolution feature may be fulfilled through ingenious structural designs[104]–[107], on the systems level, the complication in MEMS fabrication imposes tremendous difficulty in employing such an approach, leading to a restriction of the tactile sensor development. An alternative approach that circumvents the complex fabrication processes would be leveraging smart materials that exhibit tunable mechanical behaviors. In this letter, we present a design of dielectric elastomer (DE) normal force sensor with enhanced and tunable sensitivity, facilitated by modulating the mechanical property of DE by electro-mechanical stimuli in an on-site manner.

A dielectric elastomer is a soft matter that can deform dramatically in response to both mechanical and electrical stimuli. DE is classified as electroactive polymer as it operates by converting changes of voltage to mechanical deformation. When subject to voltage, a piece of DE sandwiched between two thin conductive coating layers (as shown schematically in Figure 3.1a contracts in the direction of the applied voltage and expands its normal area. Because of its electroactive behavior and large deformability, DE has been studied extensively as soft actuators with a myriad of applications in artificial muscles, soft machines, and soft robotics[100], [108]–[114]. On the other hand, a sandwich architecture of dielectric elastomer actuator (DEA) in Figure 3.1a naturally forms a deformable

capacitor, of which the capacitance is directly tuned by the deformation of DE. This fact has inspired researchers to integrate the capacitance measurement functionality into the drive circuit of DEA to bestow deformation feedback to the actuator itself, enabling simultaneous mechanical actuation and strain sensing[100], [115]–[119]. Thus more advanced controllability can be achieved through accurate real-time displacement inquiry[118], [119]. Significant progresses aside, how to enhance and tune the sensitivity of DE sensors has been less studied.

A remarkable but often neglected aspect of DE is that the effective mechanical property also changes upon the application of electrical field. That is, the application of voltage induces opposite charges on the top and bottom surfaces of the DE piece, furthermore generates a resultant electrostatic pressure, and effectively squeezes the piece in the normal direction. This electrostatic pressure serves as an auxiliary force and works synergistically with the mechanical load acting on the structure. In the existence of such an electrostatic auxiliary pressure, to deform the DE piece to the same extent, a lower mechanical pressure is needed than in the absence of the applied voltage, or a larger strain can be achieved with the same level of mechanical pressure. Equivalently, the DE piece becomes more compliant; moreover, the extra deformability depends on the voltage difference placed on the top and bottom electrodes. Therefore, by changing the voltage difference, the mechanical response of DE can be altered in a controllable manner. The modulation of the effective stiffness of the sensing medium is essential for manipulating the sensor sensitivity. Utilizing the *in situ* adjustable mechanical property of DE, therefore, represents

a promising route towards advanced tactile force sensing with tunable and enhanced sensitivity.

3.2 Deformation of a DE force sensor under pressure and voltage

3.2.1 Deformation of a DE force sensor unit under mechanical and electrical load

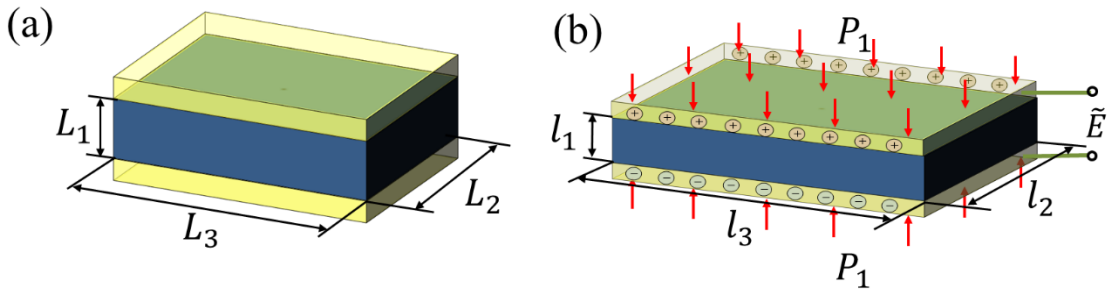

Figure 3.1 (a) Schematic of a dielectric elastomer (DE) sensor unit cell in its pristine state, dimensions of the DE (the blue part) are given by L_1, L_2, and L_3; and (b) when deformed in response to the applied voltage V and pressure P_1, the dimensions become l_1, l_2, and l_3. The yellow parts represent elastomeric conductive electrodes coated on the two sides of DE.

A piece of DE layer deforms when subject to a pressure load P_1 and a voltage V, and the dimensions in the original state L_1, L_2, and L_3 become l_1, l_2, and l_3 respectively. The deformation behavior of DE essentially resembles a hyperelastic material whose mechanical response can be derived from a free energy density function, except for that DE is responsive to both mechanical and electrical loads. It is stipulated that the free energy is composed of electrical and mechanical terms. In the deformed state, a generic form of the DE free energy density function is $w(\Lambda_1, \Lambda_1, \Lambda_3, D)$ with $\Lambda_1 = l_1/L_1$, $\Lambda_2 = l_2/L_2$, $\Lambda_3 = l_3/L_3$ denoting the stretch ratios and D representing the electric displacement. In accordance with the continuum mechanics convention, the free energy density of a deformed DE can be

defined in the reference state as $W(\Lambda_1, \Lambda_2, \Lambda_3, \widetilde{D})$, where $\widetilde{D}$ is the corresponding nominal electric displacement. As abovementioned, the energy stored in DE stems from two origins: the mechanical work done by the pressure on the deformation and the electrical work done by the power supply through the charge redistribution. Therefore, the variation of free energy density is

$$\delta W(\Lambda_1, \Lambda_2, \Lambda_3, \widetilde{D}) = S_1 \delta\Lambda_1 + S_2 \delta\Lambda_2 + S_3 \delta\Lambda_3 + \tilde{E}\delta\widetilde{D} \tag{3.1}$$

where $S_i = \partial W/\partial \Lambda_i$ (i=1,2, and 3) is the nominal stress, and $\tilde{E} = \partial W/\partial \widetilde{D}$ is the nominal electric field which is defined in the undeformed state. Note that the nominal electric field can be related to the applied voltage V through $V=\tilde{E}L_1$. When the DE piece is connected to a constant voltage supply through a closed circuit, V and $\tilde{E}$ both remain constant. We can simply write the free energy of a DE as a sum

$$W(\Lambda_1, \Lambda_2, \Lambda_3, \widetilde{D}) = W_S(\Lambda_1, \Lambda_2, \Lambda_3) + W_E(\Lambda_1, \Lambda_2, \Lambda_3, \widetilde{D}) \tag{3.2}$$

where the first term W_S denotes the energy due to stretching the polymeric network in the absence of applied voltage, and the following term W_E is the energy due to dielectric polarization.

In attempt to construct a specific form of the free energy function W, we suppose that the polymeric network follows the constitutive model by Gent[120], which captures the network stiffening effect at elevated strain levels,

$$W_s = -\frac{\mu J_m}{2}\log\left(1 - \frac{I_1 - 3}{J_m}\right) \tag{3.3}$$

where μ is the initial shear modulus, $I_1=\Lambda_1^2+\Lambda_2^2+\Lambda_3^2$ is the first invariant of right Cauchy-Green deformation tensor, and $J_m = I_m - 3$, I_m is the limiting value of I_1. The strain energy is infinite large when I_1 reaches its limiting value I_m, thus J_m is a quantity representing the maximum possible deformation. Note that μ and J_m are two material properties that can be determined experimentally[121], [122].

For the free energy arising from the dielectric polarization, to account for quasilinear and nonpolar dielectric behavior, we follow the quadratic approximation proposed by Zhao and Suo[28], [29]:

$$W_E = \Lambda_1\Lambda_2^{-1}\Lambda_3^{-1}\varepsilon^{-1}\tilde{D}^2/2 \tag{3.4}$$

where $\varepsilon=\varepsilon_r\varepsilon_0$, ε_r is the relative permittivity of DE, and $\varepsilon_0=8.854\times10^{-12}$ F/m is the permittivity of vacuum. The voltage is applied in the direction of L_1, as illustrated in Figure 3.1b.

When a dielectric elastomer deforms, the change in shape is usually much more pronounced than that in volume[28], [29], [108], [110], [123]. Consequently, it is reasonable to include the incompressibility constraint on the three stretches, i.e. $\Lambda_1\Lambda_2\Lambda_3=1$. To implement this constraint, we add a term $\Pi(\Lambda_1\Lambda_2\Lambda_3-1)$ to the free energy function W, where Π is a Lagrange multiplier. Therefore, considering Equation (3.1)~(3.4) and the incompressibility condition, the nominal stresses can be calculated respectively,

$$S_1 = \frac{\partial W}{\partial \Lambda_1}\Big|_{\Lambda_2,\Lambda_3,\tilde{D}} = \frac{\partial W_s}{\partial \Lambda_1} + \frac{1}{2\varepsilon}\Lambda_2^{-1}\Lambda_3^{-1}\tilde{D}^2 + \Pi\Lambda_2\Lambda_3 \tag{3.5-1}$$

$$S_2 = \frac{\partial W}{\partial \Lambda_2}\Big|_{\Lambda_1,\Lambda_3,\tilde{D}} = \frac{\partial W_s}{\partial \Lambda_2} - \frac{1}{2\varepsilon}\Lambda_1\Lambda_2^{-2}\Lambda_3^{-1}\tilde{D}^2 + \Pi\Lambda_1\Lambda_3 \tag{3.5-2}$$

$$S_3 = \frac{\partial W}{\partial \Lambda_3}\Big|_{\Lambda_1,\Lambda_2,\tilde{D}} = \frac{\partial W_s}{\partial \Lambda_3} - \frac{1}{2\varepsilon}\Lambda_1\Lambda_2^{-1}\Lambda_3^{-2}\tilde{D}^2 + \Pi\Lambda_1\Lambda_2 \tag{3.5-3}$$

as well as the nominal electric field,

$$\tilde{E} = \frac{\partial W}{\partial \tilde{D}}\Big|_{\Lambda_1,\Lambda_2,\Lambda_3} = \frac{1}{\varepsilon}\,\Lambda_1\Lambda_2^{-1}\Lambda_3^{-1}\,\tilde{D} \tag{3.6}$$

Equation (3.5) and (3.6) are the equations of state of DE. Note that the nominal electric field $\tilde{E}$ is directly related to the voltage V through $\tilde{E} = V/L_1$. Substituting Equation (3.6) into (3.5) gives

$$S_1 = \frac{\partial W_s}{\partial \Lambda_1} + \frac{1}{2}\Lambda_1^{-2}\Lambda_2\Lambda_3\varepsilon\tilde{E}^2 + \Pi\Lambda_2\Lambda_3 \tag{3.7-1}$$

$$S_2 = \frac{\partial W_s}{\partial \Lambda_2} - \frac{1}{2}\Lambda_1^{-1}\Lambda_3\varepsilon\tilde{E}^2 + \Pi\Lambda_1\Lambda_3 \tag{3.7-2}$$

$$S_3 = \frac{\partial W_s}{\partial \Lambda_3} - \frac{1}{2}\Lambda_1^{-1}\Lambda_2\varepsilon\tilde{E}^2 + \Pi\Lambda_1\Lambda_2 \tag{3.7-3}$$

When the DE sensor is compressed uniaxially in its thickness direction, it expands equal-biaxially in the two in-plane directions, resulting in Λ_2=Λ_3. Substituting the incompressibility condition Λ_2=Λ_3=$\Lambda_1^{-1/2}$ into Equation (3.7) we have

$$\frac{S_1}{\mu} - \frac{S_{2,3}}{\mu}\Lambda^{-\frac{3}{2}} = \frac{\Lambda - \Lambda^{-2}}{1 - J_m^{-1}(\Lambda^2 + 2\Lambda^{-1} - 3)} + \frac{1}{\Lambda^3}\left(\frac{\tilde{E}}{\sqrt{\mu/\varepsilon}}\right)^2 \tag{3.8}$$

where $\Lambda = \Lambda_1$ characterizes the deformation of the sensor. Since the deformation is homogeneous throughout the DE sensor unit, the nominal pressure applied to the DE sensor equals the corresponding nominal stress component, namely $-P_1$=S_1. Equation (3.8) relates the inputs of a DE sensor, i.e. the normal pressure P_1 and applied nominal electric field

intensity $\tilde{E}$, to the output, i.e. its deformation Λ. Therefore, Equation (3.8) governs the electro-mechanical response of the DE sensor.

3.2.2 Sensitivity of the DE capacitive force sensor

The configuration of DE sandwiched between conforming thin film electrodes, as shown in Figure 3.1, spontaneously forms a deformable capacitor, of which the capacitance can be related to the deformation through

$$C = \frac{\varepsilon a}{l_1} = \frac{\varepsilon A}{\Lambda^2 L_1} \tag{3.9}$$

where $a=l_2 l_3$ denotes the deformed surface area, and $A=L_2 L_3$ is the area in the reference state. When the DE sensor is compressed, the thickness reduces and the area expands, leading to a decreased Λ and an increased capacitance C.

The total force exerting on the DE sensor can be calculated as

$$F = P_1 A \tag{3.10}$$

The sensitivity of a sensor is defined as the change in output signal per unit change in input. Therefore, taking derivative of C with respect to P_1 yields

$$s = \frac{dC}{dP_1} = \frac{dC}{d\Lambda} \cdot \frac{d\Lambda}{dP_1} \tag{3.11}$$

For simplicity, we further define some dimensionless groups: $\underline{S_i} = S_i/\mu$, $\underline{P_i} = P_i/\mu$, $\underline{\tilde{E}}=\tilde{E}/\sqrt{\mu/\varepsilon}$, $\underline{V} = V/(L_1\sqrt{\mu/\varepsilon})$, $\underline{C} = C/(\varepsilon A/L_1)$, and $\underline{s} = s/(\varepsilon A/\mu L_1)$. In this work, we use the representative values of material properties of 3M^{TM} VHB series, a commercially

available acrylic DE: the initial shear modulus μ=250kPa, relative permittivity ε_r=6.0, J_m=125[28], [29], [123]–[125], the typical dimensions for a capacitive sensor unit are L_1=20μm, L_2=L_3=1mm. With these parameters, the highest voltage applied to the sensor will be ~300V during the working of a DE force sensor, which is modest compared to the kV level voltage applied to DE actuators[126]. A summary of theses dimensionless groups can be found in the following table.

Table 3-1 Summary of the dimensionless groups

quantity	dimensionless group	value
energy density W	μ	250 J/m^3
stress S_i, pressure P_i	μ	250 kPa
force F	μA	0.25N
electric field intensity $\tilde{E}$	$\sqrt{\mu/\varepsilon}$	6.68×10^7 V/m
voltage V	$L_1\sqrt{\mu/\varepsilon}$	1372.0 V
capacitance C	$\varepsilon A/L_1$	2.656 pF
sensitivity s	$\varepsilon A/\mu L_1$	1.0625×10^{-5} pF/Pa

3.3 DE force sensor without pre-stretch

In absence of the voltage, the sandwiched dielectric architecture reduces to a regular elastomer force sensor. For an as-fabricated sensor unit, neither the material property nor the resultant input-output dependence is to be altered. By contrast, the mechanical behavior of DE can be varied by changing the applied voltage. Equation (3.8) suggests a family of stress-deformation relations parametrized by different values of $\tilde{E}$, namely $\Lambda(S_1, S_{2,3} | \tilde{E})$.

When there exists no lateral load, $S_{2,3} = 0$ and $S_1 = -P_1$. Equation (3.8) can then be reduced to

$$\underline{P_1} = \frac{P_1}{\mu} = -\frac{\Lambda - \Lambda^{-2}}{1 - J_{\mathrm{m}}^{-1}(\Lambda^2 + 2\Lambda^{-1} - 3)} - \frac{1}{\Lambda^3}\left(\frac{\tilde{E}}{\sqrt{\mu/\varepsilon}}\right)^2 \tag{3.12}$$

Figure 3.2 plots the dimensionless pressure $\underline{P_1}$ as a function of the deformation Λ at various $\underline{\tilde{E}}$ levels. Note that Λ denotes the length ratio in the compression direction, therefore a smaller value of Λ reflects a larger deformation. For the same deformation, those DE sensors subject to a higher voltage experience a lower stress. The stress reduction can be interpreted as follows: in the procedure of compressing the sensor, the power supply is constantly providing energy by pumping charges onto the DE/electrode interfaces, the energy increase associated with dielectric polarization is $W_{\mathrm{E}} = \frac{1}{2}\Lambda^{-2}\varepsilon\tilde{E}^2$; with the electric work serving as an auxiliary, to carry the sensor unit to the same deformation, the required work done by the applied stress is therefore lowered. For Λ=0.12 (denoting a deformation where the DE is compressed to 12% of its original thickness) and $\underline{\tilde{E}}$=0, the dimensionless nominal pressure $\underline{P_1}$=77.84, whereas the dimensionless pressure reduces to 49.84 if $\underline{\tilde{E}}$=0.22. By switching on the voltage, the effective mechanical stiffness of the DE layer shows a decline of 36%.

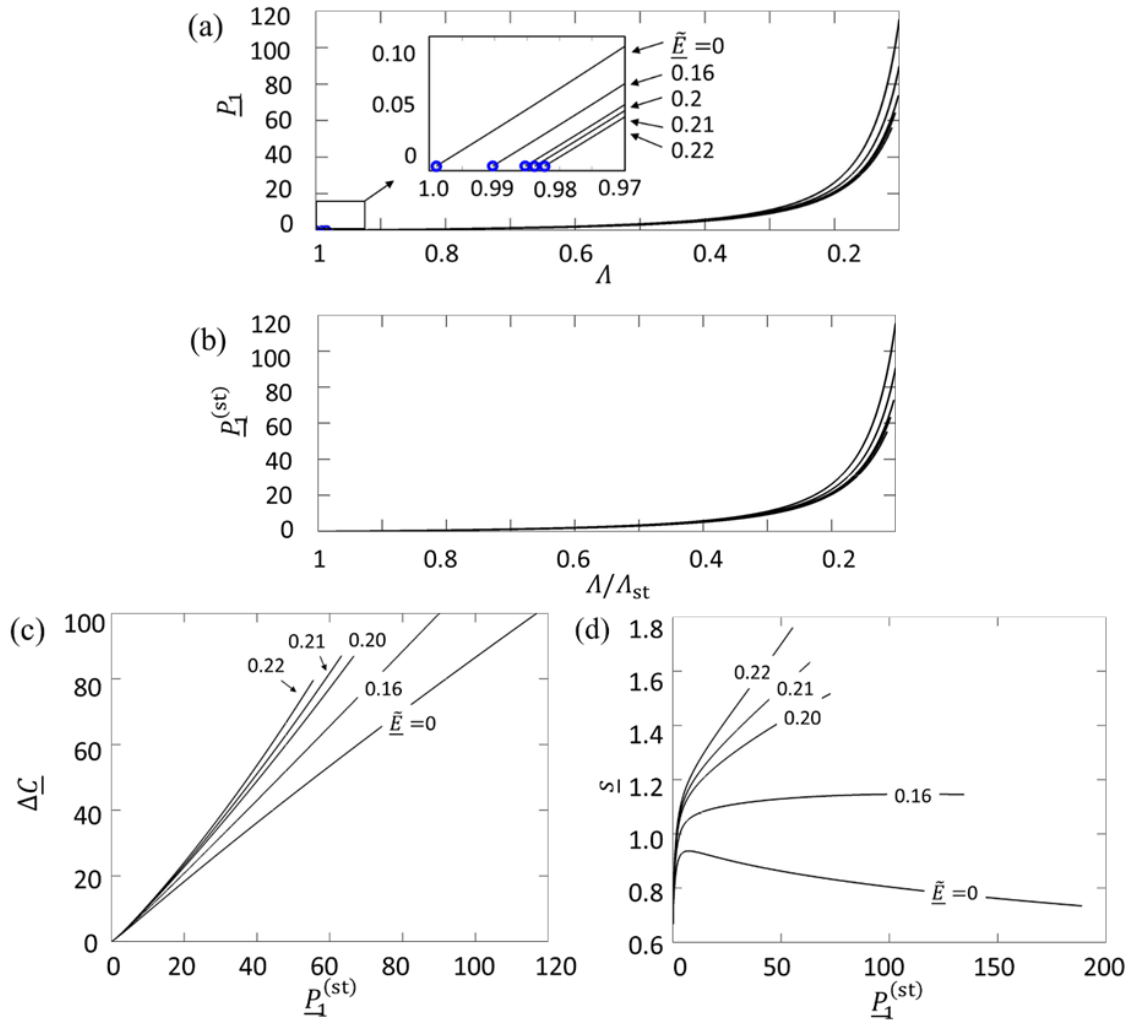

Figure 3.2 Electro-mechanical response of the DE force sensor in absence of in-plane pre-stretch. The normalized applied pressure is plotted as a function of the stretch ratio with respect to (a) the original state and (b) the starting state. The normalized voltages $\tilde{\underline{E}}$=0, 0.16, 0.20, 0.21, and 0.22. Blue circles mark the initial compression due to voltage application. Variation of (c) output capacitance signal and (d) sensitivity with applied normal stress.

It is worth noting that, before the pressure is applied to the sensor, the voltage itself has deformed the DE sensor to a starting state, which is labeled by the blue circles in Figure 3.2 inset. During this process the electric potential energy is the sole driving force of the deformation, hence the DE sensor is actually working in the actuation mode. The deformation associated with this starting state is characterized by Λ_{st} which is determined

by Equation (3.8) with the vanishing stress condition, namely $\Lambda_{\mathrm{st}} = \Lambda\left(S_1 = 0, S_{2,3} = 0 \middle| \tilde{E}\right)$. Subsequently, from these starting states the device starts to act as a sensor. Since the stresses are to be applied on top of these existing deformations, it is more convenient to recognize the starting states of DE sensors as the reference states to quantify the force loading exerted to the sensor. Then the nominal pressure defined in the new reference configuration is given by $\underline{P_1}^{(\mathrm{st})} = \underline{P_1}(\Lambda_{2,3}^{(\mathrm{st})})^{-2} = \underline{P_1}\Lambda_{\mathrm{st}}$, and the corresponding deformation can be calculated as $\Lambda/\Lambda_{\mathrm{st}}$. Figure 3.2b plots the $\underline{P_1}^{(\mathrm{st})} \sim \Lambda/\Lambda_{\mathrm{st}}$ relation.

Upon deformation the measurable output, namely the capacitance increment is

$$\Delta\underline{C} = \frac{\Delta C}{\varepsilon A/L_1} = \frac{1}{\Lambda^2} - \frac{1}{{\Lambda_{\mathrm{st}}}^2} \tag{3.13}$$

which is plotted as a function of applied pressure $\underline{P_1}^{(\mathrm{st})}$ in Figure 3.2c. At a given voltage, the capacitance increases monotonically with increasing $\underline{P_1}^{(\mathrm{st})}$, suggesting that the capacitance change can be used to measure the applied pressure. For a fixed $\underline{P_1}^{(\mathrm{st})}$, a higher voltage yields a larger capacitance change, as a result of the effective softening of the DE. For example, when $\underline{P_1}^{(\mathrm{st})}$=50, $\Delta\underline{C}$=44.92 in the absence of voltage and 70.10 with $\underline{\tilde{E}}$ =0.22. The derivative of $\Delta\underline{C}$ with respect to $\underline{P_1}^{(\mathrm{st})}$ yields the dimensionless sensitivity $\underline{s}$. As shown in Figure 3.2d, a DE force sensor with a higher applied voltage possesses enhanced sensitivity; for example, the peak sensitivity varies approximately from 0.73 to 1.76 for $\underline{\tilde{E}}$ in the range of 0~0.22. Moreover, with a modest applied voltage (e.g. from $\underline{\tilde{E}}$ =0.16 to $\underline{\tilde{E}}$ =0.22), the sensitivity of the DE sensor keeps increasing as the applied pressure increases,

indicating that the DE sensor is more sensitive in detecting pressure change at high pressure range.

In this section, we investigate the effect of voltage on the sensitivity enhancement. It is demonstrated that a higher voltage leads to an increased sensitivity. However, an elevated voltage beyond a proper scope may lead to electro-mechanical failure of the sensor, which will be systematically discussed in next section.

3.4 DE force sensor with pre-stretch

It has been demonstrated that the sensitivity of a DE sensor can be enhanced by applying a voltage; however, the increase of sensor sensitivity due to the application of the voltage is still not pronounced, exemplified by the fact that the peak sensitivity only changes by a factor of 2.41 when the voltage ramps from $\underline{\tilde{E}}$ =0 to $\underline{\tilde{E}}$ =0.22. To overcome this deficiency, we further propose a strategy to remarkably enhance the sensitivity by pre-stretching the DE sensor prior to the voltage application.

In addition, upon electrical actuation, the DE layer is susceptible to a snap-through phase separation known as electro-mechanical instability[29], [100], [109], [114]. Pre-stretching the DE piece is also proved to be an effective approach to achieving large deformation of dielectric elastomer actuator (DEA) and attenuate the electro-mechanical instability[109].

3.4.1 DE force sensor working range and electro-mechanical instability

Before the application of voltage, a pre-stretched state of the DE sensor can be achieved by equal-biaxially stretching the DE piece in the in-plane directions, as depicted in Figure 3.3b. Due to the incompressibility, the DE layer is squeezed in the thickness direction, and

the compression ratio can be calculated as $\Lambda_{\text{pre}} = \Lambda_1^{(\text{pre})} = \left[\Lambda_{2,3}^{(\text{pre})}\right]^{-2}$. The lateral stress to achieve this pre-stretch can be determined by Eq. (8) with $\underline{S_1} = 0$ and $\underline{\tilde{E}} = 0$,

$$\underline{S_{2,3}} = -\frac{\Lambda_{\text{pre}}{}^{\frac{5}{2}} - \Lambda_{\text{pre}}{}^{-\frac{1}{2}}}{1 - J_{\text{m}}^{-1}\left(\Lambda_{\text{pre}}{}^{2} + 2\Lambda_{\text{pre}}{}^{-1} - 3\right)} \tag{3.14}$$

For example, if $\Lambda_{\text{pre}} = 0.6$, i.e., the thickness becomes 60% during pre-stretch, the required lateral stress is $\underline{S_{2,3}} = 1.02$. The arrow pointing from *a* to *b* indicates this pre-stretch process in Figure 3.3f.

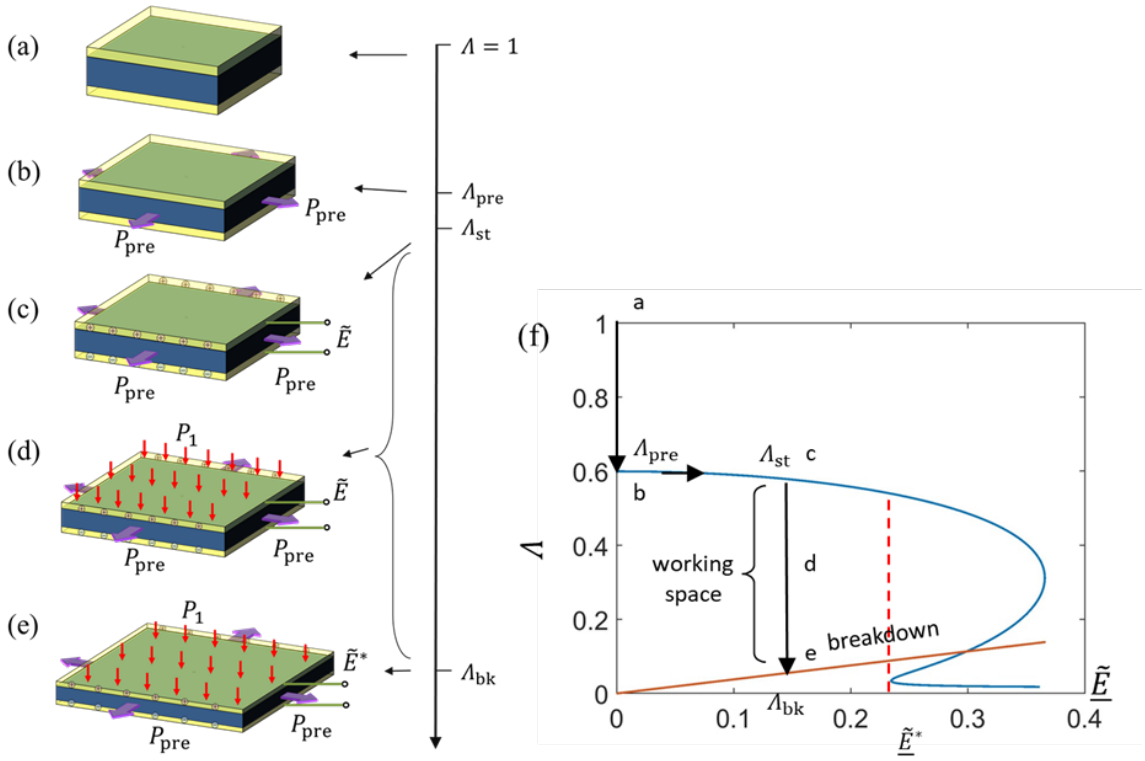

Figure 3.3 Left: Schematic of the states of a DE force sensor in sequence. And right: Sensing procedure from *a* to *e* represented in the Λ~E diagram. From (a) the pristine state, bi-lateral stresses bring the sensor to (b) the pre-strain state Λ_{pre}. The sensor attains its (c) starting state Λ_{st}, after a voltage of $\tilde{E}$ is imposed to the electrodes. Then it deforms further to (d) the working state upon the application of normal pressure. Within the working state, the sensor converts the pressure change into the change of capacitance. The DE sensor fails once it reaches (e) the dielectric breakdown state. (f) Sensing procedure from *a* to *e* represented in the Λ~E diagram, with the actuation curve

(in blue) and the breakdown line (in orange). The critical voltage $\underline{\tilde{E}}^*$ is illustrated by the red dashed line.

To avoid electrical breakdown, it is crucial to identify the maximum voltage that can be exerted to the DE sensor. During actuation process (state *b* to *c*), once the applied voltage $\underline{\tilde{E}}$ increases beyond a threshold value $\underline{\tilde{E}}^*$(indicated by the red dashed line), for a given $\underline{\tilde{E}}$ there exist more than one associated equilibrium states. As shown in Figure 3.4a, at the critical voltage $\underline{\tilde{E}}^* = 0.235$ the two possible equilibriums are Λ=0.54 and Λ=0.06 respectively, which marks a nine-time difference in thickness. When subject to a perturbation, the DE sensor may shift between these co-existing equilibrium states with an abrupt change in the deformation Λ. Such an abrupt change in thickness caused by snap-through instability is generally hazardous for DE, since the collapsed state may fall underneath the breakdown line, as illustrated by the red arrow in Figure 3.4a. In these cases, electrical breakdown fails the DE sensor even prior to the application of any force. In order to avoid such failure, the applied voltage $\underline{\tilde{E}}$ should remain below the critical voltage $\underline{\tilde{E}}^*$.

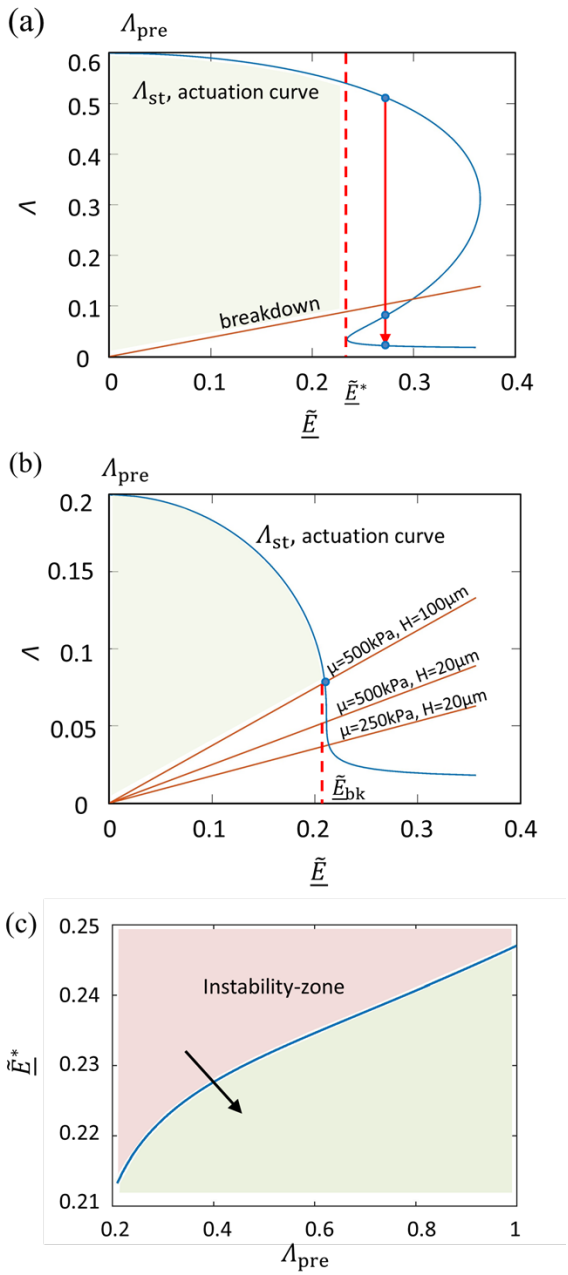

Figure 3.4 Instability and safety zone of the DE sensor. (a) At Λ_{pre}=0.6, the actuated starting states form an S-shaped curve on Λ~E diagram. Beyond the critical voltage $\tilde{E}^*$, snap-through instability occurs and the DE sensor collapses from Λ=0.54 to 0.06 (shown by the red arrow), penetrating the breakdown line, and leading to electrical breakdown. (b) When Λ_{pre}=0.2, the actuation curve of the starting states is single-valued. The breakdown voltage is identified by the point where the actuation curve and breakdown line intersect. The breakdown line varies with material properties and geometric parameters of the DE sensor. (c) Instability critical voltage $\tilde{E}^*$ for given pre-stretch. The

$\underline{\tilde{E}}^*\sim\Lambda_{\text{pre}}$ separates the instability zone from the safe zone. The arrows represent two ways of avoiding instability.

The electro-mechanical instability is mitigated by tuning the pre-stretch level of the DE sensor. Comparing Figure 3.4a with Figure 3.4b, one may conclude that the actuation curve evolves from an S-shaped curve at a modest pre-stretch (Λ_{pre}=0.6) to a monotonously decreasing curve at an elevated pre-stretch (Λ_{pre}=0.2), consequently the electro-mechanical instability disappears. Although critical voltage $\underline{\tilde{E}}^*$ for electro-mechanical instability does not exist for sensors with $\Lambda_{\text{pre}}\leq$0.20, the intersection of breakdown line and actuation curve identifies a breakdown voltage $\underline{\tilde{E}}_{\text{bk}}$, i.e. the highest voltage that can be exerted on the DE sensor with $\Lambda_{\text{pre}}\leq$0.20. Beyond $\underline{\tilde{E}}_{\text{bk}}$, the sensor failures by electrical breakdown before it could reach the starting state.

3.4.2 Deformation behavior and sensitivity performance of a DE force sensor with pre-stretch

Given a combination of Λ_{pre} and $\underline{\tilde{E}}$, upon normal pressure, the continuous deformation of the DE sensor tracks a vertical line connecting the starting state on and the electrical breakdown limit. All the admissible working states of a DE sensor is highlighted by the green region in Figure 3.4a and Figure 3.4b. For pre-stretch Λ_{pre}=0.6, the actuation curve, breakdown curve, and voltage threshold $\underline{\tilde{E}}^*$ demarcate a trapezoid-like region representing the working states. In comparison, if Λ_{pre}=0.20, the working states of the sensor constitute a fan-liked region, as shown in Figure 3.4b. Moreover, since the breakdown line is determined by the original thickness and the material properties, i.e., $\Lambda_{\text{bk}}=\frac{\sqrt{\mu/\varepsilon}}{E_{\text{bk}}}\underline{\tilde{E}}$, the

electrical breakdown line can be tilted by reducing the original thickness or selecting DE material with smaller $\sqrt{\mu/\epsilon}$. Changing these parameters may expand the working zone of the DE sensor as shown in Figure 3.4b. Figure 3.4c shows the critical voltage $\underline{\tilde{E}}^*$ as a function of pre-stretch Λ_{pre}. The green-shaded area beneath the $\underline{\tilde{E}}^* \sim \Lambda_{\text{pre}}$ curve is the safe zone, whereas the red-shaded area is the failure zone where electrical breakdown occurs due to snap-through instability. The arrows in Figure 3.4c indicate two ways of avoiding the abrupt collapse: using a lower voltage or reducing the pre-stretch level.

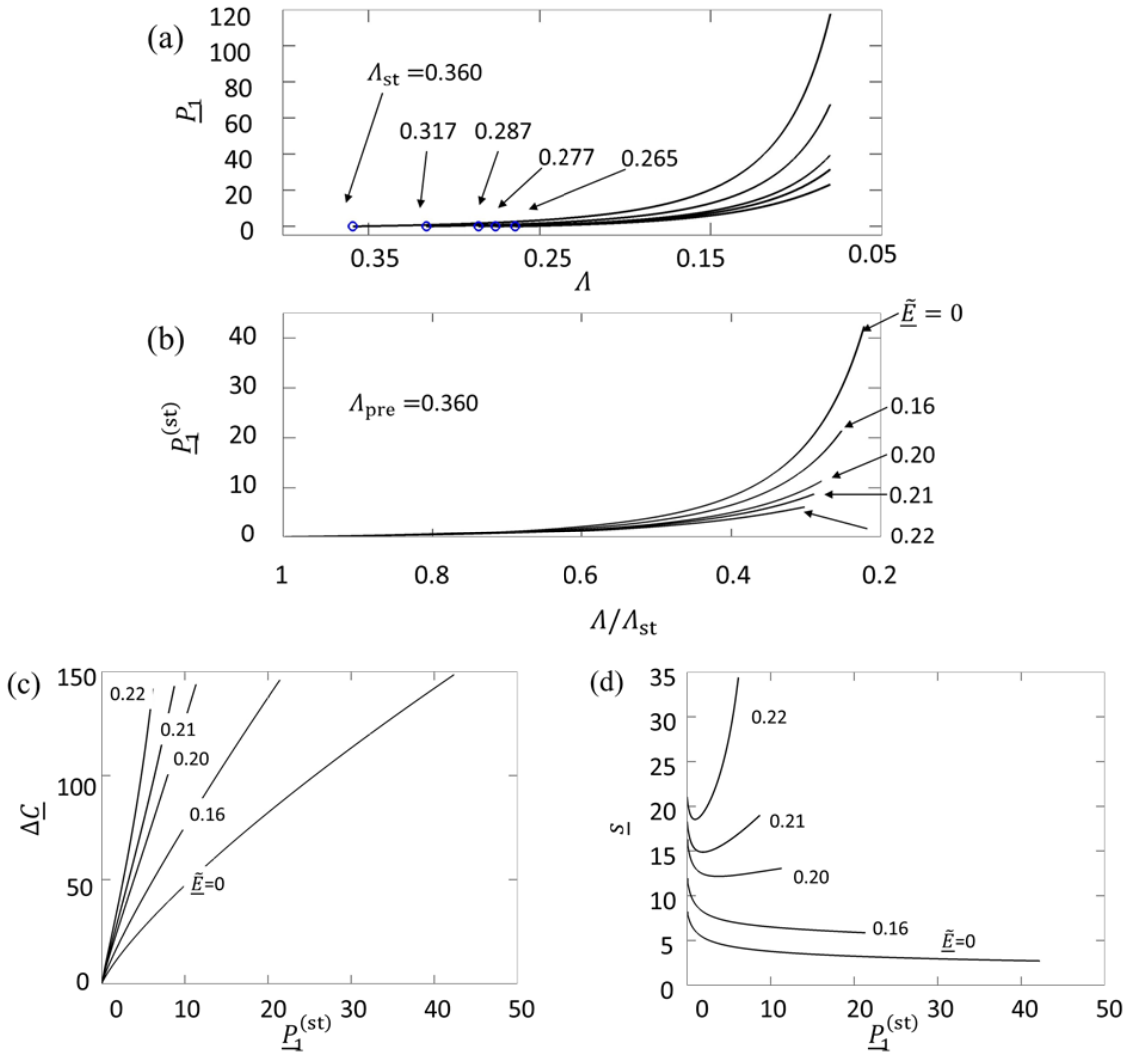

Figure 3.5 Force-deformation relation at Λ_{pre}=0.36 with different applied voltages$\underline{\tilde{E}}$=0, 0.16, 0.20, 0.21, and 0.22, using (a) the original state and (b) the starting state as the reference state. Blue circles mark the starting states. (c) Dimensionless capacitance output signal and (d) sensitivity at Λ_{pre}=0.36.

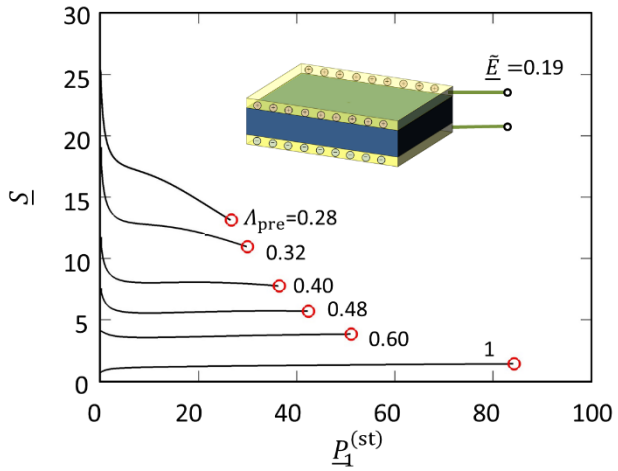

Figure 3.6 Dimensionless sensitivity at various pre-stretch levels with a fixed voltage $\underline{\tilde{E}}$=0.19. The red circles at the end of each curve represent the final states, i.e., at which the sensor fails by electrical breakdown.

We next study the load-deformation relation of DE sensor within the working zone. With a pre-stretch of Λ_{pre}=0.36, the $\underline{P_1}$~Λ characteristic curves are drawn in Figure 3.5a with a series of normalized voltage $\underline{\tilde{E}}$. The blue circles mark the starting states of each sensor. The required normal stress to deform the DE sensor to a certain extent is further reduced compared with cases without pre-stretch as shown in Figure 3.2a; the DE material is made more compliant by pre-stretching the sensor prior to the voltage application. Figure 3.5b plots the pressure/deformation relation with respect to the starting states for each sensor.

The output capacitive signal ΔC is plotted against $\underline{P_1}^{(st)}$ in Figure 3.5c and the sensitivity $\underline{s}$ is shown in Figure 3.5d. $\underline{s}$ varies from 2.73 to 34.4, which is approximately twenty times

as the largest sensitivity in absence of pre-stretch. Figure 3.6 shows how the sensitivity scales up with the pre-stretch level. At same applied voltage $\underline{\tilde{E}}$=0.19, $\underline{s}$ increases by one order of magnitude when pre-strain deformation changes from 1 to 0.28. The sensitivity of the DE normal force sensor fabricated with the identical material can be tuned over a large range ($\underline{s}$=0.73 when no pre-strain and voltage applied; $\underline{s}$=34.4 at $\underline{\tilde{E}}$=0.22 and Λ_{pre}=0.36) through the combination of pre-stretch and applying voltage. As we point out, pre-stretching and applying voltage provides a facile approach to achieving tunable and enhanced sensing capability of DE force sensor.

3.5 Summary of Chapter 3

In conclusion, the present design using dielectric elastomer as the sensing medium has demonstrated the possibility of achieving in situ tunable and enhanced sensitivity, which is in sharp contrast to the traditional force sensor designs with fixed sensitivity. The tunable sensitivity is attributed to the fact that the effective mechanical property of DE sensor can be modulated through pre-stretch and voltage. To characterize the design of the DE force sensor, we identified four stages of such a DE sensor: the pre-stretch state upon the bi-lateral pre-stretch, the starting state upon application of voltage, the working state under normal stress, and the final state at the dielectric breakdown limit. We further investigated the failure mode of the DE sensor by studying the electromechanical instability at the actuation stages and its effect on the working range of the DE sensor. By simply leveraging the combination of pre-stretch and voltage, the *in situ* sensitivity can be enhanced by a factor of 47.12. Moreover, tunable and enhanced sensitivity is achieved by only changing

the voltage and pre-stretch. Such a facile design strategy may find application in robot skins and shed light into using advanced materials in novel tactile sensor designs.

Chapter 4: Deformation of Temperature Sensitive Hydrogel and a Light-Sensitive Morphology Transform Hydrogel[3]

A striking feature of hydrogel is the large deformability inherited from its soft nature. Due to this large deformability, it has been extensively explored as soft actuators to mimic the living organisms. In this chapter, we develop a composite porous hydrogel sheet that can rapidly transform into multiple 3D shapes in response to a near-infrared (NIR) light on-demand. The transformation relies on a photo-thermal-induced asymmetric shrinking of the hydrogel material, which was further verified by finite element modeling.

4.1 Background

4.1.1 Hydrogel material system development and the inspirations from nature

As aforementioned in the introduction chapter, in the past decade hydrogel emerges as an interdisciplinary research frontier where material sciences, medical sciences, bioengineering, and mechanical engineering encounter. The underlying reason why hydrogel is located at the crossroad is manifold. First of all, the hydrogel bears a striking similarity to the material found in natural living organisms: both contains a substantial amount of water as an important constituent. The other constituent phase of hydrogel is a

[3] The main results from this chapter have been published as or submitted for publication

- H. Guo, **J. Cheng**, J. Wang, P. Huang, Y. Liu, Z. Jia, X. Chen, K. Sui, T. Li, Z. Nie Reprogrammable ultra-fast shape-transformation of macroporous composited hydrogel sheets, *Journal of Materials Chemistry* B, 5 (16), 2883-2887 (2017).
- H. Guo, **J. Cheng**, K. Yang, K. Demella, T. Li, S. Raghavan, Z. Nie, Programming the Shape Transformation of Composite Hydrogel Sheet via Erasable and Rewritable Nanoparticle Patterns (2019) *Under review*.

hydrophilic cross-linked polymer network, such a structure into which matters are organized is also an analogy to what possessed by biological materials, for example organ tissues. The similarity entails hydrogel superb bio-compatibility, enabling an array of applications from the everyday necessary contact lenses to drug releasing media for wound healing. Furthermore, living organism tissues function differently from different organs due to the cellular differentiation process from which cells acquire specialized structures and functions. Inspired by nature, hydrogels material can also be engineered with functional molecular groups linked to the polymer network backbones, enriching the applications of hydrogel and broadening the horizon of hydrogel research. For example, azobenzene functional group which undergoes an isomeric transition under UV exposure can be synthesized to the polymer network resulting in a photosensitive hydrogel [127]–[129]. Lastly, both hydrogels and natural biomaterials are easily deformed upon mechanical loadings, making hydrogel material a promising candidate for applications from soft actuators and soft sensors towards an overall integrated technology for soft robots.

Therefore, the inspirations one may get from nature for hydrogel material system design can be categorized into three following aspects:

I. Novel hydrogel material structures inspired by nature biomaterials.

II. Novel hydrogel synthesis and fabrication process inspired by nature biomaterials.

III. Novel hydrogel system functionalities inspired by nature biomaterials.

The purpose and motivation of this chapter is to (1) establish a light-responsive hydrogel material system which mimics the morphological change of nature organisms; (2) develop a multi-physics analytical and simulation capability to unveil the mechanism of morphological change; (3) apply the analytical framework to guide the development of the bio-mimicking hydrogel as well as evaluate the performance of this new hydrogel.

4.1.2 Morphology change strategies in nature

Figure 4.1 Examples of self-adaptive morphological change in nature (a) swimming of a squid in ocean in response to neural signal; (b) blooming of a flower in response to temperature and day light cycle; and (c) closing of a Venus flytrap due to instantaneous water loss triggered by electrical potential change. (Figures used here are obtained from Google and with appropriate reproduction license.)

Form squid swimming (Figure 4.1a), flower blooming (Figure 4.1b), to Venus trap closing (Figure 4.1c), there is a wealth of inspirations soft actuators and soft robots can borrow from nature's self-adaptive morphology transforms [130]–[133]. These strategies share in common two key features. Firstly, multiple patterns can be achieved from a single organism. An octopus is able to conform to almost any arbitrary shape of a container and still functions well to escape. Secondly, these living organisms change the morphology in

quick response to external stimulus in their respective timescales. The squid waves its body fin in a fraction of one second to strike the water. Venus trap closes fast enough to capture the insects who triggered the closing mechanism. However, presently the existing efforts to design and fabricate shape-transforming hydrogel-based actuators are heavily dependent on preprogrammed patterns, limiting the number of target shapes a soft actuator is able to acquire [134]–[140]. In this case, one or more responsive components are patterned in the hydrogel sheet and the target shapes are already determined at the design stage.

In order to address this delinquency, a preprogram-free, strcutre-independent, and reprogrammable poly (N-isopropyl acrylamide) (PNIPAM) Ag nanoparticles (AgNPs) composite hydrogel is proposed. The strategy utilizes light as triggering stimulus [141]–[143], instead of preprogramming the hydrogel structure at the fabrication stage, the patterning which bears the shape transform information can be placed at the light source side.

4.2 *Design of reprogrammable light-responsive hybrid hydrogel system*[4]

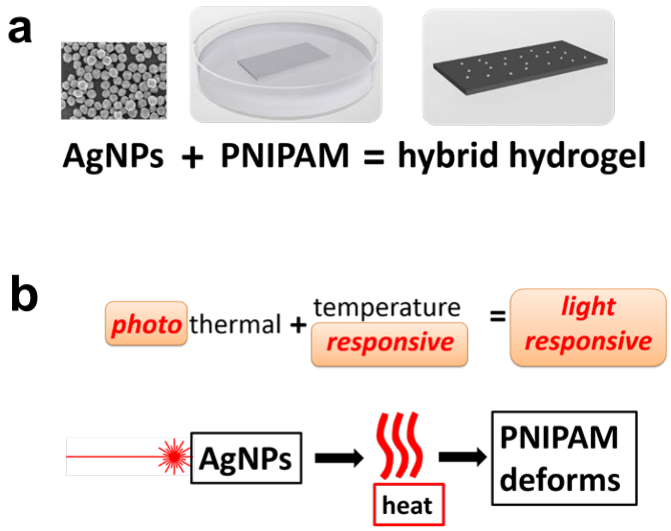

Figure 4.2 (a) Illustration of the PNIPAM/AgNPs hybrid hydrogel system (b) Concept of the light-responsive shape transform mechanism. A combination of the AgNPs' photo-thermal effect and PNIPAM's temperature sensitive phase transition make the hybrid hydrogel light-responsive to NIR exposure.

The structure of the PNIPAM/AgNPs hybrid hydrogel system is illustrated in Figure 4.2a. After gelation the PNIPAM hydrogel piece is immerged in a Ag^+ solution where the Ag nanoparticles are produced through an in-situ reduction process of the Ag^+. The PNIPAM/AgNPs hybrid hydrogel is fabricated. The constituent PNIPAM hydrogel undergoes a coil-to-globule transition at the lower critical solution temperature (LCST) around 32ºC [144]. This molecular transition results in a rapid dehydration of the PNIPAM hydrogel due to the abrupt change in hydrophilicity of the polymer network associated with

[4] Experiments in this section is designed and conducted by Dr. Hongyu Guo from Prof. Zhihong Nie's research group, Department of Chemistry and Biochemistry, University of Maryland, College Park

the phase transition[145]. In addition, the embedded AgNPs transduce near infrared (NIR) photons into heat, serving as localized heat flux sources. A combination of PNIPAM and AgNPs brings together the photothermal effect and the thermal responsiveness, resulting in a light-responsive hydrogel, as shown in Figure 4.2b. By changing the shape of light pattern on the same hybrid hydrogel sheet, various morphology transform can be achieved, as shown in Figure 4.3. Upon the removal of irradiation, the hybrid sheet starts to recover its original flat shape and is ready to transfer into a different shape upon irradiation with another pattern. The porous microscopic structure fosters water transportation inside the hydrogel, enabling a fast light-responsive within several seconds to reach the maximum deformation.

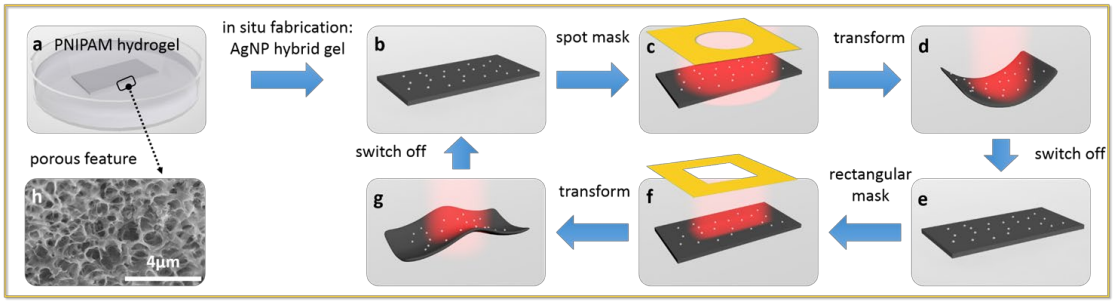

Figure 4.3 Concept of the PNIPAM/AgNPs hybrid hydrogel transforming into different shapes in response to NIR light irradiation. (a) The PNIPAM hydrogel immersed in Ag^{+} solution. (b) the PNIPAM/AgNPs hybrid hydrogel fabricated by in-situ reduction process of Ag^{+}. (c) Under NIR irradiation through a round mask the hybrid hydrogel transforms into a (d) dome shape. (e) Shape recovery when the light is removed. (f) Under NIR irradiation through a rectangular mask the hydrogel piece deforms into a (g) saddle. (h) SEM image of the hybrid unveils porous structure at microscopic scale.

4.3 Deformation mechanics of temperature-sensitive PNIPAM hydrogel

4.3.1 Free energy model of temperature-responsive hydrogel

In our PNIPAM hydrogel, the interacting aggregation of cross-linked polymer chain network and solvent molecules constitutes a thermodynamic system of which the macroscopic behaviors are governed by its thermodynamic energetics. The deformation of PNIPAM hydrogel in balance with mechanical loads and a solvent reservoir can be modeled by the framework developed by Cai and Suo [24]. By thermodynamics consideration, the Helmholtz free energy of a swelling hydrogel arises from two origins: i) the stretching of the polymer network and ii) the mixing of the two species of molecules. Hence the free energy density function takes the form:

$$W = \frac{1}{2}NkT[\mathbf{F}:\mathbf{F} - 3 - 2\log(J)] + kT\left[c\log\left(\frac{vc}{1+vc}\right) + \frac{(A_0 + B_0T)c}{1+vc} + \frac{(A_1 + B_1T)c}{(1+vc)^2}\right] \tag{4.1}$$

where W is the free energy per unit volume in the dry state, N is the number of polymer chains per unit volume in the dry state, k is Boltzmann constant, T is the current temperature at the material point, **F** is the deformation gradient tensor which takes the original dry state as reference frame, J is the Jacobian of deformation gradient tensor, i.e., J=det(**F**), v is the molecular volume of water, c is the relative concentration of solvent molecules in the hydrogel-solvent aggregation, and A_0, B_0, A_1 and B_1 are parameters related to the enthalpy of mixing. The first term in Equation (4-1) denotes that the stretching of polymer chain network obeys a neo-Hookean hyperelastic material law, and the second term implies that

the mixing of PNIPAM polymer and water molecules follows the Flory-Huggins theory of solution [18]. A_0, B_0, A_1 and B_1 in Equation (4-1) are to be fitted to the experimental data for different temperature-responsive hydrogels, as we will identify in the immediate section for our PNIPAM-AgNPs hybrid hydrogel.

Equation (4-1) specifies the explicit expression of the free energy density function which takes the extensive variables **F**, c as well as the intensive variable T as its arguments. In such cases that the hydrogel is put in contact with a stable aqueous reservoir, the chemical potential of solvent molecule μ is constant; then upon Legendre transformation, the free energy density W is carried to its corresponding thermodynamic potential:

$$\widehat{W}(\mathbf{F}, \mu, T|N, A_0, B_0, A_1, B_1) = W(\mathbf{F}, c, T|N, A_0, B_0, A_1, B_1) - \mu c \tag{4.2}$$

thus, $\hat{W}$ is a natural function of **F**, μ and T.

When the stress level is adequately low so that no new void or pore is generated in the hydrogel, the volumetric change of the material solely results from the migration of solvent molecules; hence the deformation **F** and solvent concentration c are correlated by [23]:

$$J = 1 + vc \tag{4.3}$$

Substitute Equations (4.1) and (4.3) into Equation (4.2), one arrives at the explicit form of $\hat{W}$:

$$\widehat{W}(\mathbf{F},\mu,T|N,A_0,B_0,A_1,B_1)$$
$$= \frac{1}{2}NkT[\mathbf{F}:\mathbf{F}-3-2\log(J)]$$
$$+\frac{kT}{v}(J-1)\left[\log\left(\frac{J-1}{J}\right)+\frac{(A_0+B_0T)}{J}+\frac{(A_1+B_1T)}{J^2}\right] \quad (4.4)$$
$$-\frac{\mu}{v}(J-1)$$

4.3.2 Free swelling of PNIPAM hydrogel in water and determination of parameters

When submerged in an aqueous environment with homogeneous temperature field, a piece of free standing PNIPAM hydrogel, in the absence of pre-introduced stress, will swell (or contract) freely in response to the uniformly varying temperature field. The free swelling case satisfies the condition that the hydrogel deforms uniformly in any three orthogonal directions and that the hydrogel retains its stress-free state since neither deformation mismatch nor mechanical constraint exists. For such a homogeneous deformation, the principal stretch ratios have identical value, and the deformation gradient tensor becomes

$$\mathbf{F} = \begin{bmatrix} \lambda & & \\ & \lambda & \\ & & \lambda \end{bmatrix} \quad (4.5)$$

where λ is the uniform stretch ratio. And in this case the volumetric ratio $J=V/V_0=\lambda^3$, where V is the volume of the hydrogel piece in the deformed state and V_0 is the volume in the reference (dry) state.

As discussed above the stress tensor vanishes:

$$S_{ik}(\mathbf{F},\mu,T|N,A_0,B_0,A_1,B_1) = \frac{\partial \widehat{W}}{\partial F_{ik}} = 0 \quad (4.6)$$

Equation (4.6) yields the relation between stretch ratio λ and temperature T in the free swelling case. In addition, if the chemical potential of water is known and set to zero, then T can be readily expressed by the following equation:

$$T = -\frac{Nv(\lambda^5 - \lambda^3) + \lambda^6 \log(1 - \lambda^{-3}) + \lambda^3 + (A_0 + A_1\lambda^{-3})}{B_0 + \lambda^{-3}B_1} \tag{4.7}$$

The equation above dictates the temperature required by the principle of minimum free energy, in free swelling cases, for the temperature-sensitive hydrogel to maintain certain amount of deformation. In other words, it also depicts how the hydrogel deforms in response to the change of the homogeneous temperature field.

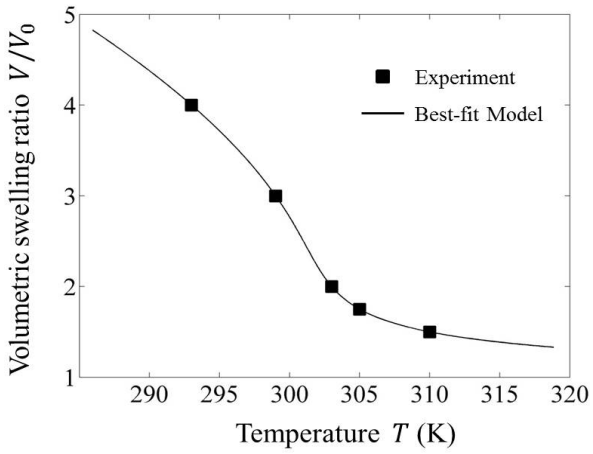

Figure 4.4 Volumetric swelling ratio of porous PNIPAM hydrogel as a function of temperature. This curve is used to determine the parameters used in finite element modeling as described in the text of the supporting information

By fitting the function $T(\lambda|\mathbf{S}=0, \mu=0)$ to the experimentally obtained T~J relation, we determined the parameters Nv, A_0, B_0, A_1 and B_1. Figure 4.4 shows the fitted curve of volumetric ratio $V/V_0 = \lambda^3$ as a function of temperature T, with the specified parameters:

Nv=0.03317, A_0=−2.5418, B_0=0.01081, A_1=0.57099, B_1=−0.000418. We will use this set of parameters for our PNIPAM hydrogel in the following calculations.

4.3.3 Model of heat transfer

When the top surface is exposed to NIR laser, the AgNPs embedded in PNIPAM absorb the photons and convert the light energy into heat, the surrounding hydrogel matrix is thus heated. In order to benchmark the thermal properties of our PNIPAM hydrogel, we setup the transient heat transfer model for a hydrogel piece with length L_d=1.7cm, width w_d=0.85cm and thickness t_d=0.5mm (same dimensions as the hydrogel piece in the NIR light irradiation experiment). The initial temperature of the entire body is the same as ambience temperature T_0=295K. Then the top surface of the hydrogel piece is brought to exposure to two adjacent laser stripes with width w_l=0.2cm and heat flux intensity H=1.2 $J \cdot cm^{-2} \cdot s^{-1}$, and the bottom surface away from the laser irradiation is set to the constant ambience temperature. Laser is switched on for 120 seconds and is shut down thereafter to let the hydrogel cool down through heat dissipation into the ambience. Keeping track of the temporal evolution of the highest temperature on the top surface, we are allowed to compare the temperature response curve with the experimental data and determined the thermal diffusivity of PNIPAM hydrogel $\alpha=K/\rho Cp=2.36\times10^{-5}$ cm^2/s, where K, ρ and Cp denote the thermal conductivity, density, and specific heat of the material respectively. The temperature contour of the top surface and the highest temperature evolution are shown in Figure 4.5b with comparison to the thermography.

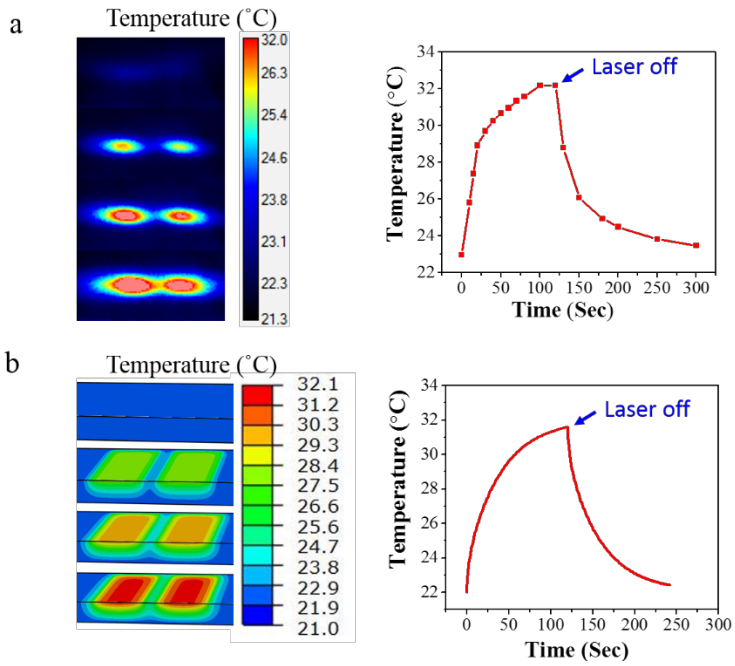

Figure 4.5 Thermography for heat transfer model calibration and a comparison between the experiment and the simulation results. The hybrid sheet is irradiated for 120 seconds and remove the light source. (a) Thermography and the evolution of the maximum surface temperature. (b) Simulation result and the evolution of the maximum surface temperature.

4.3.4 Fully-coupled thermomechanical model of the light-responsive hydrogel

The deformation behavior of a temperature-sensitive hydrogel is governed by a thermodynamic free energy thus resembling a hyperelastic material [23], [24]. Each thermodynamic equilibrium state of temperature-sensitive hydrogel is a local minimum of the system free energy which can be fully defined by the stretch ratios λ and a dependent solvent molecule concentration c as discussed above. Furthermore, the thermodynamic equilibrium is to be altered upon the change of environment variables. Therefore, besides of being able to respond to the conventional mechanical loads, such materials as PNIPAM

hydrogels are also able to deform in accordance with the change in temperature and chemical potential.

Solving for the equilibrium states is a boundary value problem (BVP). For simpler cases, e.g., free swelling hydrogel with homogeneous temperature, analytical solution can be obtained, whereas for more complicated case, e.g., hydrogel swelling in an inhomogeneous temperature field, the BVP can be solved numerically by FEM. We adopted the FEM framework established by Ding et al. for the temperature-responsive hydrogel [25], and prescribed the material properties determined above to the PNIPAM hydrogel used in this study. At this stage we assume that the deformation of PNIPAM hydrogel will not affect the heat transfer processes. A fully coupled thermo-mechanical algorithm is implemented in the commercial FEM package ABAQUS by making use of its temperature-displacement elements.

4.3.5 Deformation of PNIPAM hydrogel in inhomogeneous temperature field

When the hybrid hydrogel is partially exposed to NIR irradiation, the temperature of irradiated region increases due to the photo-thermal effect of the AgNPs, whereas the other areas remains at the ambience water temperature. A non-uniform temperature field is thus established. As shown in the thermography in Figure 4.5a, an in-plane thermal gradient (ranging from 22 ºC to 32 ºC) is created over the hydrogel top surface. In addition, the heat propagation along the thickness direction and come to a thermal equilibrium with the surrounding surfaces, as is confirmed by the cross-sectional temperature profile from the simulation (Figure 4.5b).

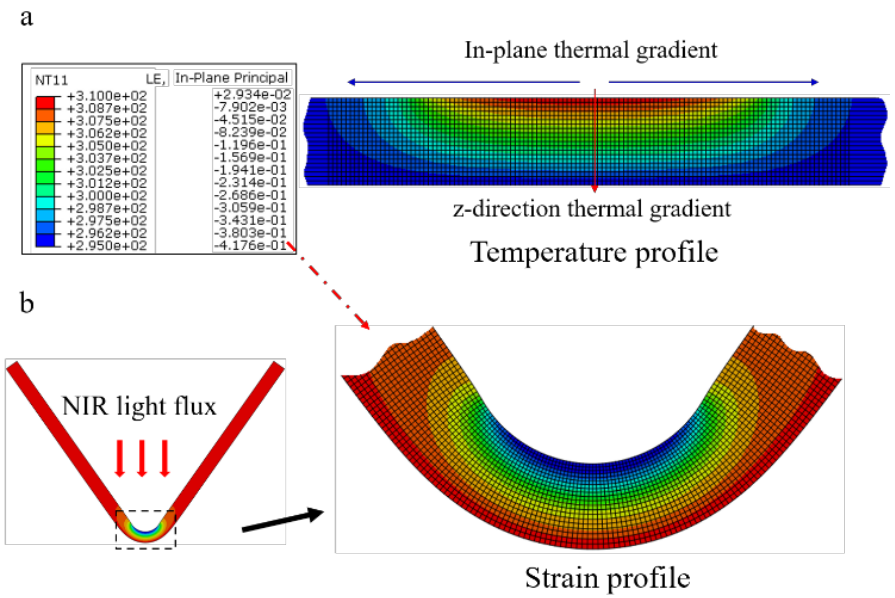

Figure 4.6 Temperature-gradient-induced asymmetric strain field. (a) FEM analysis of temperature distribution within the hybrid sheet upon light irradiation. An infinite convection boundary condition is used in the calculation of the temperature profile. (b) FEM analysis reveals that an asymmetric strain distribution is established within the sheet upon localized light exposure, which essentially actuates the sheet's bending.

Because there are two types of temperature gradients in the hybrid sheet: the in-plane thermal gradient and through-thickness thermal gradient (Figure 4.6a). For the bending shape transformation, the in-plane temperature gradient determines the position of the localized deformation, as the bending tip resides at the center of the in-plane gradient. In contrast, the z-direction thermal gradient causes a larger volumetric change closer to the top-surface, thus breaking the deformation symmetry along the direction of hydrogel thickness and determining the bending direction. For more complicated shape transformations (such as the dome shape and saddle shape under corresponding light masks), each light illumination generates a signature temperature field inside (as well as over the surface of) the hydrogel body. A combination of the in-plane and through-

thickness thermal gradient together determines a unique morphology change. As shown in Figure 4.7, each irradiation shape corresponds to a unique temperature gradient field inside the hydrogel, resulting in a specific deformed shape. The shape transforms predicted by the simulation are in good agreement with the experiment.

The swelling behavior of PNIPAM hydrogel stemming from this microscopic mechanism can be captured by its thermodynamics [146]: the coil-to-globule transition is associated with change in a macroscopic Helmholtz free energy. Moreover, the non-uniform swelling field in the hydrogel body is accompanied by interior stresses, as a result of the swelling difference between the hydrogel and its neighboring material. In such case, the free energy of the hydrogel includes the strain energy in addition to the free energy due to the mixing of PNIPAM network and water molecules. At the presence of a temperature gradient, the equilibrium responses of PNIPAM hydrogel to the inhomogeneous temperature field are governed by the mechanical model which determines the steady states of PNIPAM hydrogel as the Helmholtz free energy minima of the entire system calculated by Equation (4.4). The PNIPAM constitutive model is implemented in ABAQUS user subroutine and the deformation is computed using the directly coupled thermo-mechanical analysis. Without missing the nature of the deformation, the exterior surfaces of the hydrogel sheet are set to be at infinite convection thermal exchange with the ambience in the heat transfer model. (The effects of finite convection boundary condition to the deformation of the hydrogel is studied in section 4.4.) The hydrogel material in the exposed area undergoes a gradual compression-to-stretch change due to the established thermal gradient. The

differential swelling due an asymmetric temperature field in the hydrogel material actuated its bending.

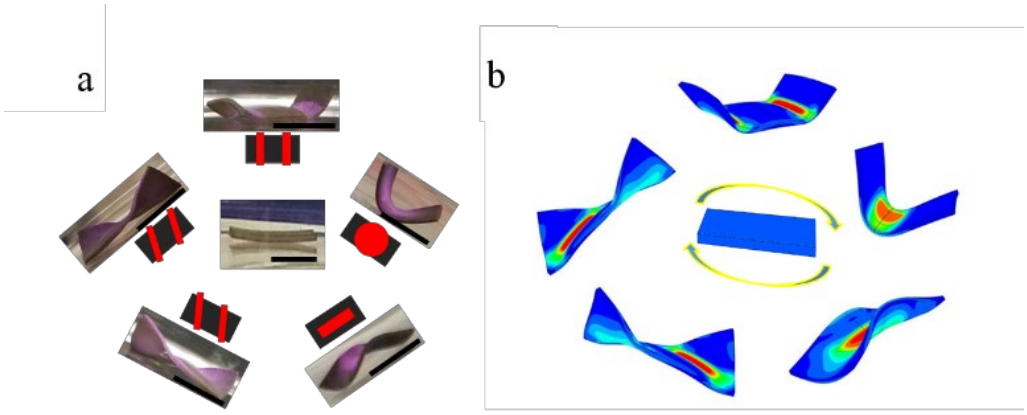

Figure 4.7 Experiment and simulation results of shape transformations of the same hybrid hydrogel sheet into five different shapes. (a) Experiment. (b) Simulation. The red stripes in (a) indicate the shape of light pattern. Scale bar: 0.85cm. The contour in (b) shows the stress level in the hydrogel body, with red and blue representing high and low stress respectively.

4.3.6 Parametric study of the effects of the light irradiation width and power density on the actuated deformation

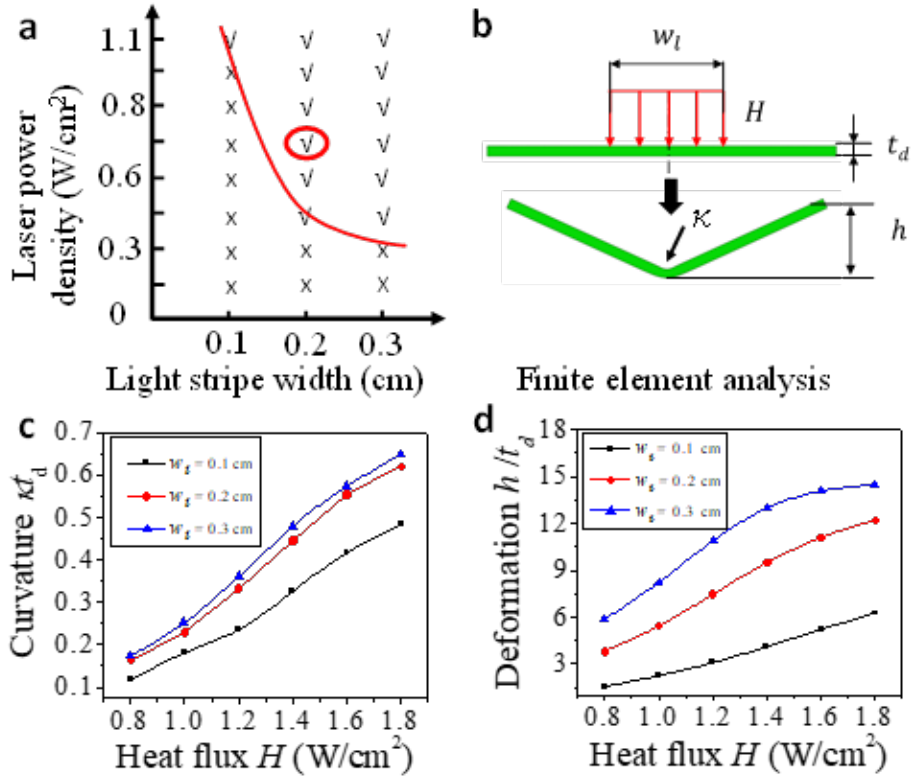

Figure 4.8 Effects of laser power density and laser stripe width on the activated deformation. (a) Experimental study on the bending of the hybrid hydrogel sheet as a function of laser power density and irradiation stripe width. The width of the rectangular irradiation stripe was varied while its length was kept as 0.9 cm. The red circle indicates the irradiation condition used in the current experiment. √: the sheet bent at the applied irradiation. ×: the sheet exhibited no visible bending under the applied irradiation. (b), (c), (d) FEM analysis of the sheet's deflection (h/t_d) and bending curvature (κt_d) with respect to laser power density and irradiation stripe width. The FEM results indicated that the deflection and bending curvature increased with the increase of either laser power density or irradiation stripe width.

In order to investigate the impact of the heat flux intensity H and the laser stripe width w_l on the deformation of the PNIPAM hydrogel piece, a two-dimensional plane strain model

of 1.7cm×0.5mm hydrogel is exposed to a stripe-shaped laser irradiation with heat flux intensity H and width w_l. We plot the dimensionless curvature (κt_d) as the indicator of localized deformation and the dimensionless transverse deflection (h/t_d) as the measurement of overall deformation (Figure 4.9). The simulation confirms such a positive correlation between the bending deformation and the laser power density as well as the stripe width (Figure 4.8c, d, and Figure 4.9). The bending deformation increases with the increase of either the laser power density or the irradiation stripe width. Increasing the laser power density enhances the heat generation. A larger thermal gradient is hence established in the sheet resulting in an increased bending. Moreover, the wider laser stripe makes a larger portion of hydrogel to contribute to the total deformation and as a result, the deflection is larger. The curvature at the tip and the deflection in the lateral direction both increases as H and w_l increase.

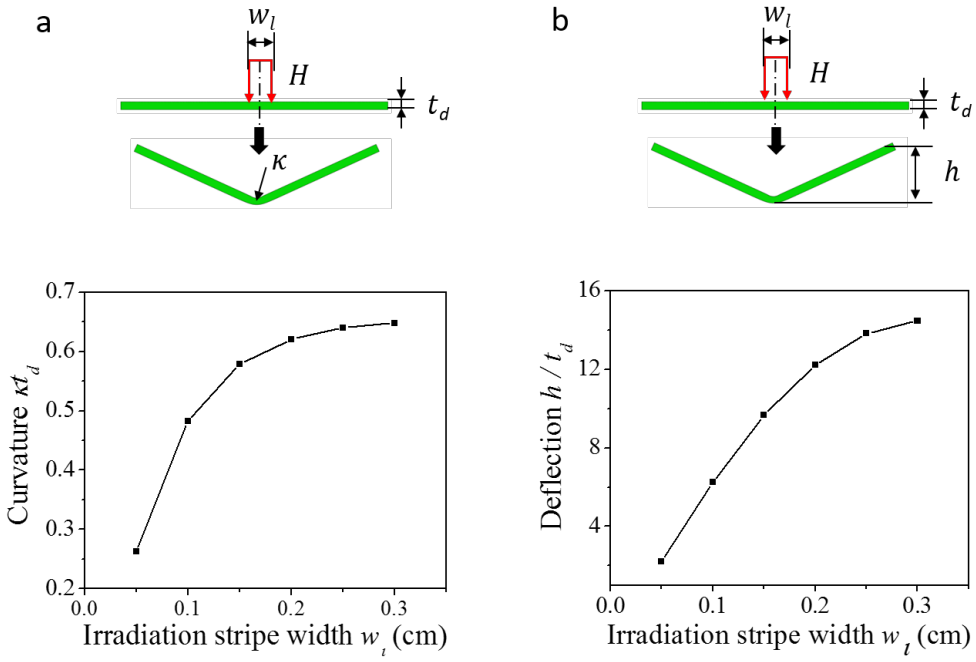

Figure 4.9 Finite element modeling of effects of irradiation stripe width on bending of the hybrid sheet. The bending increases with the increase of irradiation stripe width. a) Normalized curvature κt_d ; b) deflection h/t_d as a function of laser stripe width w_l at heat flux intensity H=1.8 J·cm^{-2}·s^{-1}

We also establish a parametric experimental study using a light irradiation stripe to trigger the bending deformation. As shown in Figure 4.8a, if the total energy provided is low (total energy input $P = H \times w_l$), the dissipation prevails thus no effective thermal gradient is established. The actuation phase diagram in Figure 4.8a has a hyperbola boundary, indicating the activation threshold is in form of a product of laser power density and the strip width. Compared to the simulation, there exists an irresponsive zone in the experimental phase diagram. This can be attributed to the fact that the activation due to thermal input should be at least greater than a threshold dictated by the dragging force from the water environment. That is, the activated deformation is too small to overcome the water resistance at small energy input.

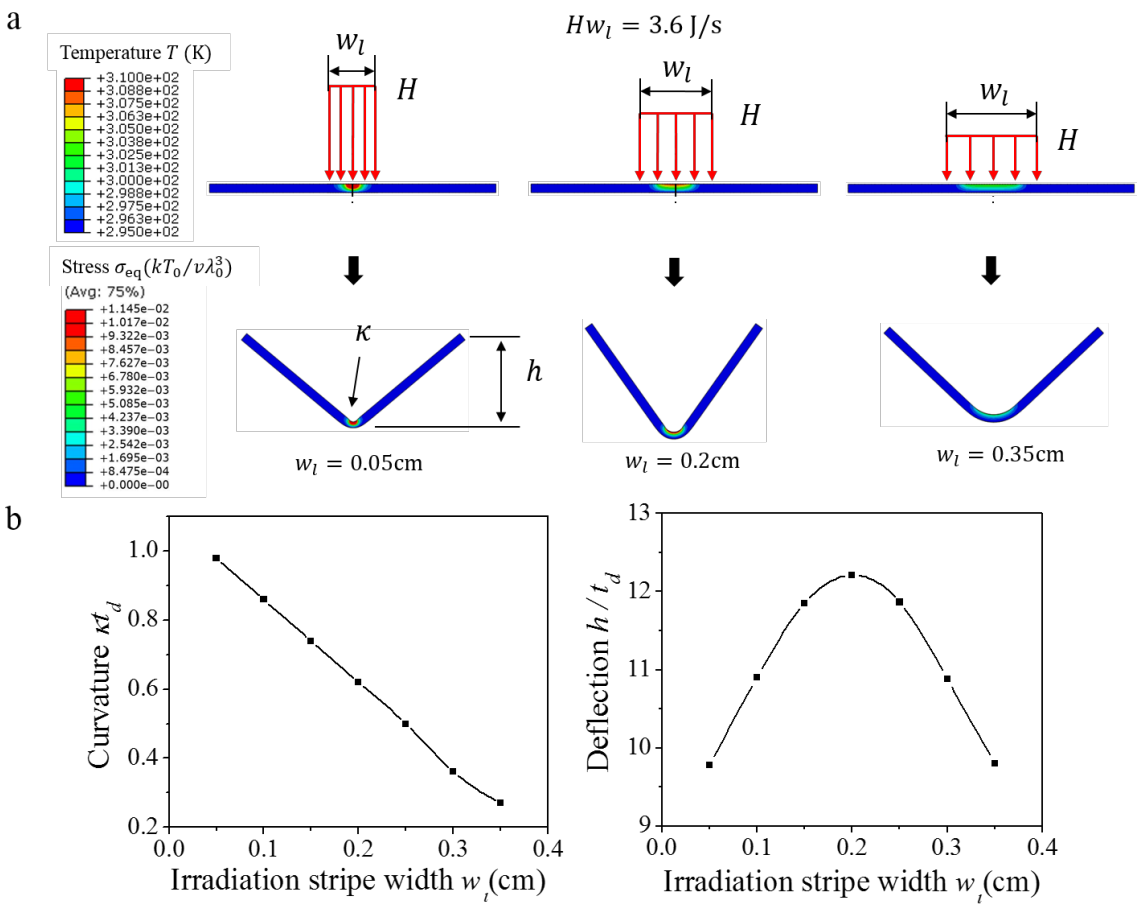

Figure 4.10 Finite element modeling of the bending of the hybrid hydrogel sheet with respect to laser stripe width at a fixed total input energy. (a) The hybrid hydrogel sheet is subject to laser stripes with the light input energy fixed at 3.6 J/s. (b) Normalized curvature κt_d and deflection h/t_d as a function of laser stripe width w_l at a fixed light input energy of 3.6 J/s. t_d is the thickness of the hybrid sheet which is 0.5 mm. The FEM analyses indicates that at a fixed light input energy, the bending curvature decreases with the increase of laser stripe width, while the overall deflection (h/t_d) reaches a maximum when increasing the laser stripe width.

Additionally, if a PNIPAM hydrogel piece is brought to exposure to a fixed power laser source, i.e., the total quantity of energy absorbed by the hydrogel is fixed at certain amount ($P=Hw_l$=const), there exists an optimal combination of H and w_l which yields the largest deflection. As shown in Figure 4.10a, the wider laser stripe comes with a lower intensity

and a narrower one comes with a higher intensity if the laser source power is fixed at $P=Hw_l=3.6$ J/s. Figure 4.10a also shows the temperature field in the reference state and the stress field in the deformed state. The stress scale is normalized by $kT_0/v\lambda_0^3$, where the Boltzmann constant $k=1.3806\times10^{-23}$ $m^2kg\cdot s^{-2}K^{-1}$, the initial temperature $T_0=295$K, the initial stretch ratio $\lambda_0=1.5489$ (at $T_0=295$K and relative to the dry state), and the molecular volume of water $v=2.9922\times10^{-29}$ m^3. Upon the increasing w_l the intensity H decreases, and the resulting localized deformation is deduced (Figure 4.10b). However, the deflection of the hydrogel piece has a maximum at $w_l=0.2$cm, this is because the deflection indicates the level of the total deformation of the entire piece. The increasing w_l brings a larger part of hydrogel into irradiation, while the amount of heat which per unit area of top surface receives is reduced. The tradeoff between the increasing number of contributors and decreasing amount of the contribution per share allows the existence of the maximum deflection.

4.4 Deformation of light-responsive hydrogel with heat transfer model using convective boundary condition

4.4.1 Effects of finite convection

The light responsive deformation behavior of the hybrid hydrogel depends on the heat transfer process inside the hydrogel which establishes an asymmetric temperature field triggering the directional bending towards the laser source side. The heat transfer process is determined by two main factors, namely the energy flux input from the laser and the heat dissipation through convection into the ambience. In the model used in the present sections,

we fixed the temperature on the back surface of the hydrogel at the ambience temperature. This case corresponds to the maximum convection condition on the back surface, i.e., the convection coefficient is infinite so that the energy dissipates at the highest rate. As a result, the back-surface temperature of the hybrid hydrogel sheet equals the temperature of its surrounding water. Such treatment is valid only if approach such as forced convection is implemented.

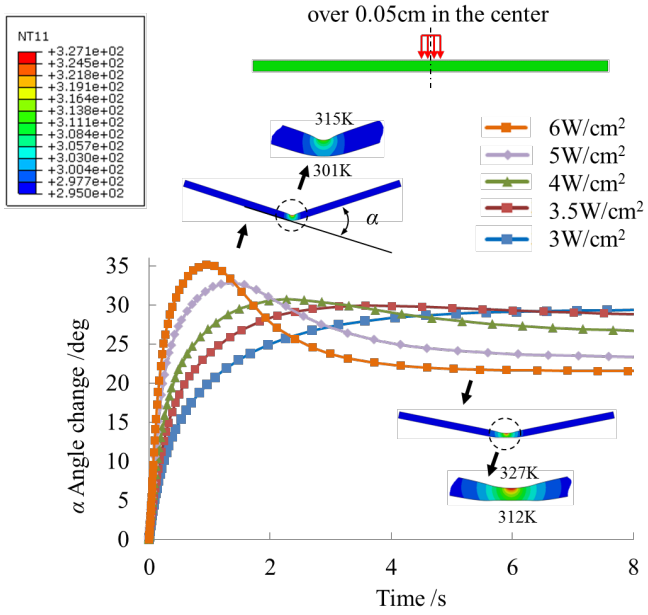

Figure 4.11 Effect of finite convection on the activated deformation. Temporal evolution of the bending angle at various heat fluxes *H* into the center of the hydrogel. The color legend in top left side of the figure showed the temperature distribution at both the peak bending angle state and at the steady state when H=6W/cm^2.

To investigate the effect of finite convection on the evolution of temperature and deformation, we prescribed finite convection boundary condition on the hydrogel surface, in addition to the heat flux over the central section of the top surface. Because the water molecules inside the hydrogel network still retained mobility of migrating back and forth

between the network and the ambience, the convection coefficient was set at a moderate value 700 $Wm^{-2}K^{-1}$, and the ambience temperature was set at the room temperature 295K.

We used the angle change α to quantify the bending deformation. Figure 4.11 shows the temporal evolution of α for different heat flux inputs. When heat flux was comparatively small (H=3 and 3.5W/cm^2), α increased monotonically with time and converged to an equilibrium state value of 29.5° at ~6s. In all the other cases where H>3.5W/cm^2, the angle reached a maximum value and started to decay. For example, when H=3.5W/cm^2, α reached a peak value 35.2° at 1s, then gradually reduced to a steady state value at 21.6°. Compared to the fixed temperature boundary condition, the heat dissipation was smaller for the finite convection case, thus temperature field was established at a higher rate, which resulted in a fast deformation response: at the maximum bending angle, the highest temperature in the center of the top surface was 315K, and the back surface was heated up to 301K. A temperature difference of 14K was developed in ~1s. In addition, with finite convection both the top and back surfaces were heated to a higher temperature. The elevated temperature on the back surface leaded to a reduction of the bending angle. As shown in Figure 4.4, the globule/coil phase transition of PNIPAM was accomplished at ~305K, and the volumetric deformation in the top layers reached its saturation. Therefore, any further temperature increase only resulted in the shrinkage in the back layers, pulling the hydrogel piece away from its initial deformation, which in turn reduced the bending angle. As indicated by the temperature profiles at the equilibrium state in Figure 4.11, even though the temperature difference between the top/back surfaces at the maximum deformation state (14K) was slightly smaller than that at the final state (15K), the bending

angle was 13.6° larger. This was because the increase of the top surface temperature from 315K to 327K was not accompanied with any further shrinkage, whereas the volume of the back-layer reduced as the temperature increased from 301K to 312 K. This resulted in the reduction of bending angle from the maximum bending state.

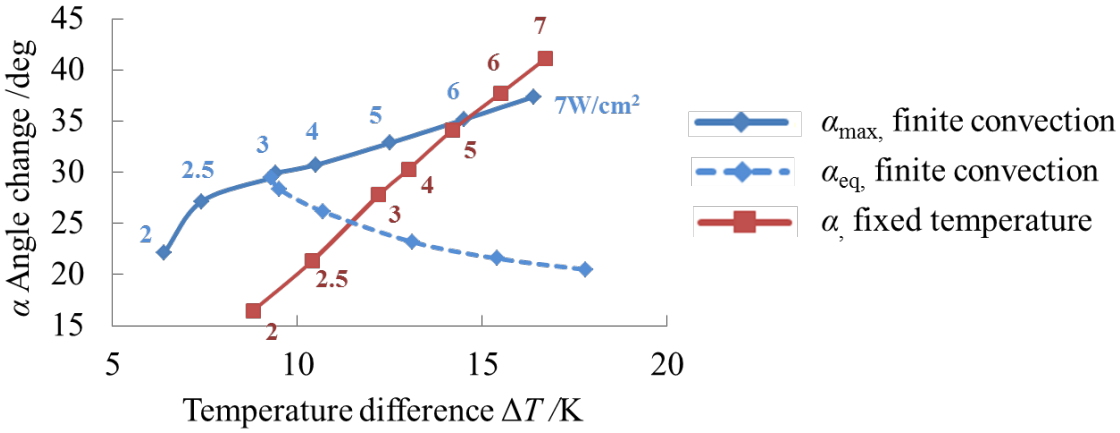

Figure 4.12 Effect of temperature difference between sheet's top and bottom surface on its bending. The solid blue line shows the maximum bending angle under 700 $Wm^{-2}K^{-1}$ surface convection (finite convection condition), and the dashed line represents α in the steady state under same surface convection condition. The red line shows the bending angle for fixed temperature boundary condition. The numbers indicate the heat flux inputs.

To compare the deformation capability of the hydrogel piece under finite and infinite convection boundary conditions, the bending angle was plotted in Figure 4.12 against the top/back surface temperature difference. At first, the hydrogel with finite convection deformed more. This was because (1) the top surface temperature was higher with finite convection, and (2) the heat-affected zone was larger near the top. When ΔT>15K, these two factors were overcome by increased temperature in the back-layer and the deformation was larger for the infinite convection case. The dashed line showed the bending angle in the equilibrium state.

4.4.2 Impact of the non-uniform thermal conductivity

The distribution of AgNPs in the hybrid hydrogel also affected the heat transfer behavior. Our experiments indicate that the AgNPs tend to aggregate at top than at bottom surface of the sheet and might be sparsely distributed within the hybrid sheet. Therefore, there might exist a thermal conductivity difference along the thickness direction. To demonstrate the effect of the non-uniform thermal conductivity on the deformation behavior, the hydrogel piece was partitioned into two layers from the median plane, and the thermal conductivity of the bottom layer was set to 1/3 that of the top layer to mimic the AgNP depletion. The applied 5 W/cm^2 heat flux and the convection on other exterior surfaces were the same as the baseline case, as shown in Figure 4.13a. The calculated bending angle in the steady state was 45.7° while the hydrogel with uniform thermal conductivity only bent 23.2° (Figure 4.13b and d). This was because that the bottom layer with reduced thermal conductivity functioned as a thermal barrier which impeded the heat propagation into the bottom layer. Therefore, the heat was transferred more into the top layer and generated a heat-affected zone with an increased size. As shown in Figure 4.13c and e, the area where T>303K had a width of 2.1mm, in comparison to the baseline case where the width of the same area was 1.6mm. The increased size of heat-affected zone involved more PNIPAM material to contract on the top surface, resulting in a larger deformation.

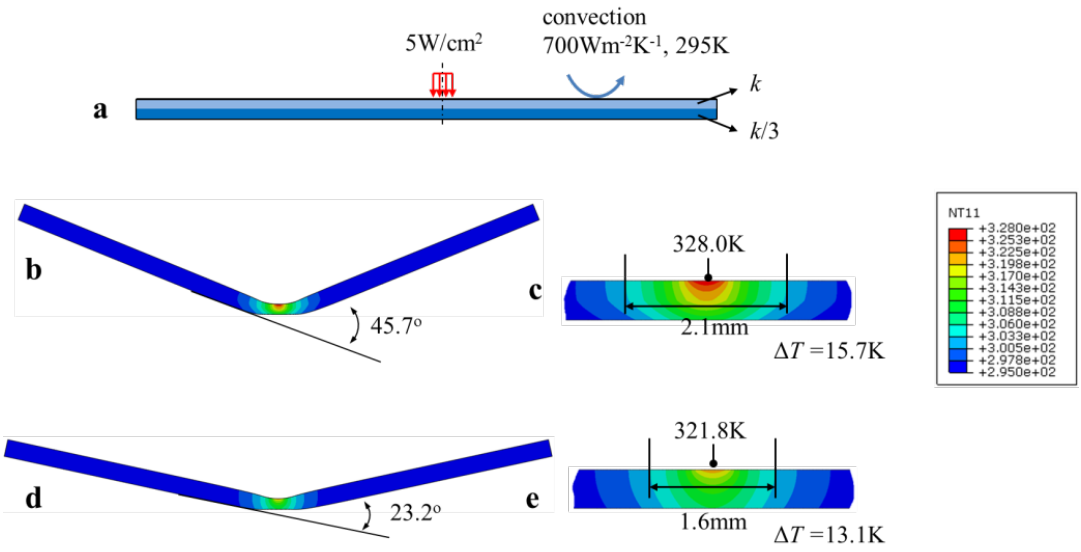

Figure 4.13 Effect of the inhomogeneous thermal properties in the thickness direction. (a) Schematic of a double-layered hydrogel piece with different thermal conductivities k. (b) Bending angle in steady state for double-layered hydrogel and (d) for the baseline case. (c) and (e) The temperature profiles in the reference (undeformed) frame for both cases.

4.4.3 Impact of the ambience temperature

In all the aforementioned calculations, we set the ambience temperature at 295K. Upon further illumination, the local temperature of water near the hydrogel piece will also increase due to its weak absorption of NIR light. To understand the effect of the increased ambience temperature, we set the ambience temperature at 300K over the 3.5mm section in the center of the back surface, and left the ambience temperature around all the other surfaces at 295K. The applied 5W/cm^2 heat flux remains the same as the baseline case. The bending angle declines to 12.7° from 23.2° (Figure 4.14 a and b). This further reduction of deformation corresponds to the dome collapse which was observed in the experiment for the thinner sheet (Figure 4.14c~f). Figure 4.15d~g indicates that at higher power input the heating effect penetrates the entire thickness of the hydrogel piece, resulting in an

elevated back-surface temperature and a reduced activated angle. The thickness-direction thermal gradient is necessary for the hybrid sheet to have a stable shape transformation. The deformation of the hybrid hydrogel system is a result of a fine interplay between the heat transfer in the hydrogel and the dissipation into the environment.

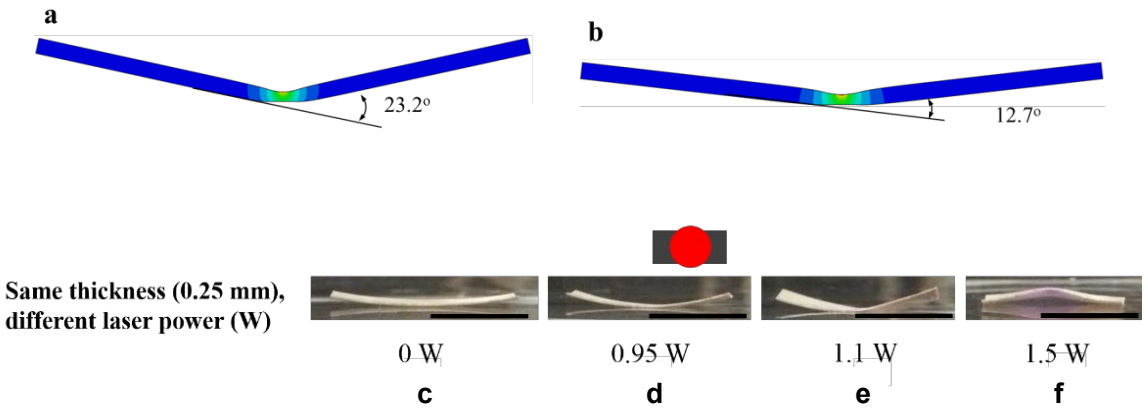

Figure 4.14 Bending instability due to the destruction of thermal gradient. Simulation: Bending angle reduced from (a) 23.2° in the baseline case to (b) 12.7° if the ambience temperature increased to 300K over the center 3.5 mm section of the back surface. Experiment: Shape transformation of the hybrid hydrogel sheet under increasing laser power. (c)~(f) the sheet undergoes a bending instability when the power reaches 1.5W. Scale bar: 0.85cm.

4.5 Summary of Chapter 4

In this chapter, we create a light-responsive hybrid sheet composed of a thermo-responsive polymer (PNIPAM) and silver nanoparticles (AgNPs). The light-responsive behavior is a combination of the photothermal effect of the AgNPs and the temperature-sensitive phase transition of PNIPAM. Upon NIR irradiation, the hydrogel shape transformation is highly reversible and reprogrammable.

From the perspective of thermodynamics, we establish an analytical model for the deformation mechanics of the proposed hybrid hydrogel. Taking advantage of this coupled thermomechanical analytical capability, we shed light on the mechanism of the light-responsive behavior of the new material system. According to the theoretical analysis and FEA results, each shape transformation relies on the unique swelling pattern generated by the specific thermal gradient established by the light pattern. The thermal gradient is created through a delicate balance between the continuous localized heating by the AgNPs under NIR irradiation and the heat dissipation to the aqueous environment.

To guide the design of the hybrid hydrogel, we further evaluate in depth the effects of the light irradiation geometry, power density, and the heat transfer boundary conditions on the morphology transform. We unveil that the most effective shape transformation (measured by the activation angel) is dependent on the z-directional thermal gradient. Finite convection of the surrounding aqueous environment results in an increased back-surface temperature which in turn reduces the thermal gradient and diminishes the activation angle.

Chapter 5: Deformation Mechanics of Microfiber-Reinforced Anisotropic Hydrogel[5]

5.1 Introduction

5.1.1 Anisotropy in the Nature's soft matters

Hydrogel has emerged as one of the most promising bio-mimicking materials, for the sake of its ultrahigh water content and extraordinary bio-compatibility [147], [148]. Inspired by nature's broad lore of deformation mechanisms, in fields such as soft actuators and soft robots, researchers have devoted great attention in reproducing morphology transforming schemes of living organisms by using manmade hydrogels. Even though the living organisms are often characterized by a highly hierarchical, directional and anisotropic microscopic structure (as shown schematically in Figure 5.1), in sharp contrast, their inorganic counterpart hydrogel usually possesses an isotropic architecture, inherited from the conventional polymerization process [147]. However, anisotropic structures has an enabling role in the performance of physiological functions: muscle depends on the uniaxial contractions of the muscle fibers to act (Figure 5.1a); cartilage relies on the

[5] The findings from this chapter have been published or summarized for publication as

- Y. Kuang, C. Chen, **J. Cheng**, G. Pastel, T. Li, J. Song, F. Jiang, Y. Li, Y. Zhang, S. Jang, G. Chen, T. Li, L. Hu, Selectively aligned cellulose nanofibers towards high-performance soft actuators, *Extreme Mechanics Letters* (2019) *Accepted*.
- C. Chen, J. Song, **J. Cheng**, Z. Pang, Y. Kuang, W. Gan, H. Huang, U. Ray, T. Li, L. Hu, All-wood hydrogel with durable elastic compressibility by exposing cellulose nanofibers for structure reformation (2019) *Under review*.
- **J. Cheng**, Z. Jia, T. Li, Modeling the anisotropic mechanical behaviors of microfiber reinforced hydrogels: A constitutive model and its applications (2019) *In preparation*.

anisotropic structure of collagens to provide lubricating intraosseous support (Figure 5.1c); and the directional mass transportation inside plant vascular bundles is realized by the highly aligned cellulose fibers (Figure 5.1b).

5.1.2 Current efforts in designing anisotropic hydrogels and applications

In an attempt to fill this gap, an array of approaches to endowing hydrogel with oriented microstructures were developed within the past decade to mimic the nature's anisotropic soft matters using artificial materials. As summarized by a recent review by Sano et al. [147], these methods can be categorized into three distinctive types: (1) Hybrid hydrogel with interacting micro/nano-fillers[16], [30], [149], [150]; (2) hydrogel with aligned micro-channels resulting from the directional crystallization of solvent [151], [152]. (3) Hydrogel with aligned reinforcement fibers or secondary network [153].

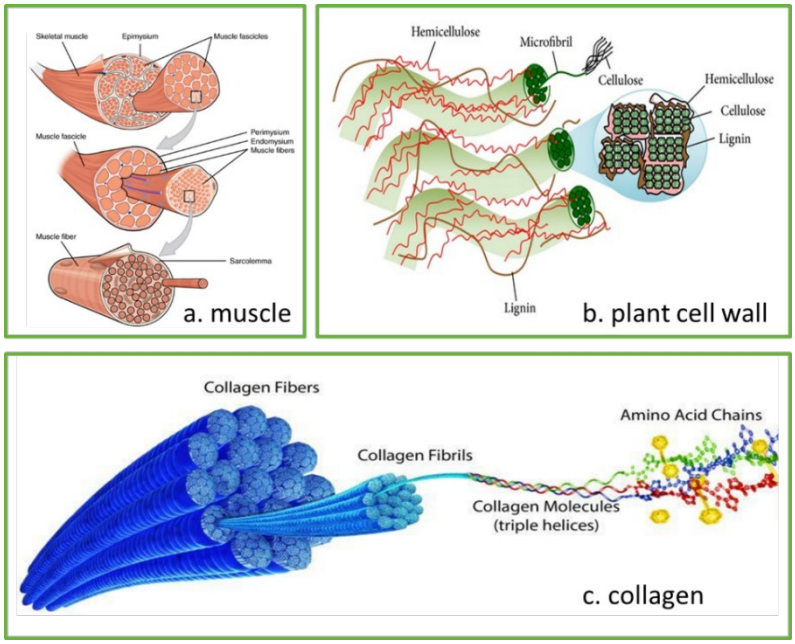

Figure 5.1 Anisotropic, directional, and hierarchical architecture of living organism of nature. (a) Hierarchical structure of muscle. (b) Hierarchical structure of plant cell wall. (c) Hierarchical structure of collagen tissue.

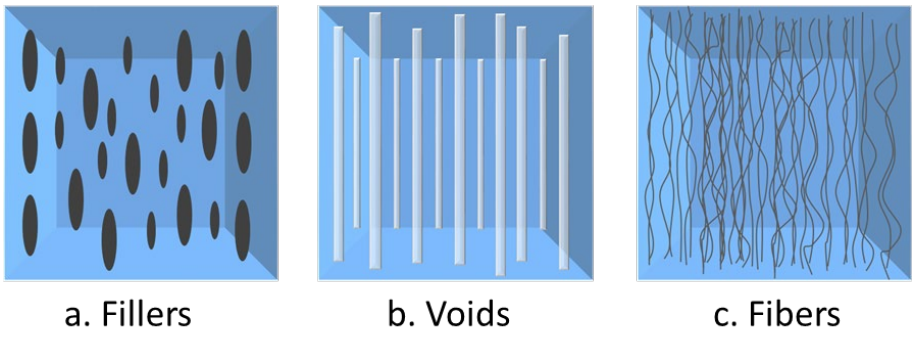

Figure 5.2 Strategies and approaches to introducing directional structures in artificial hydrogel materials[147]. (a) Micro/nano-filler hybrid hydrogel (b) Hydrogel with directional micro-channels. (c) Hydrogel with aligned fibers or network. (Reproduced from the reference)

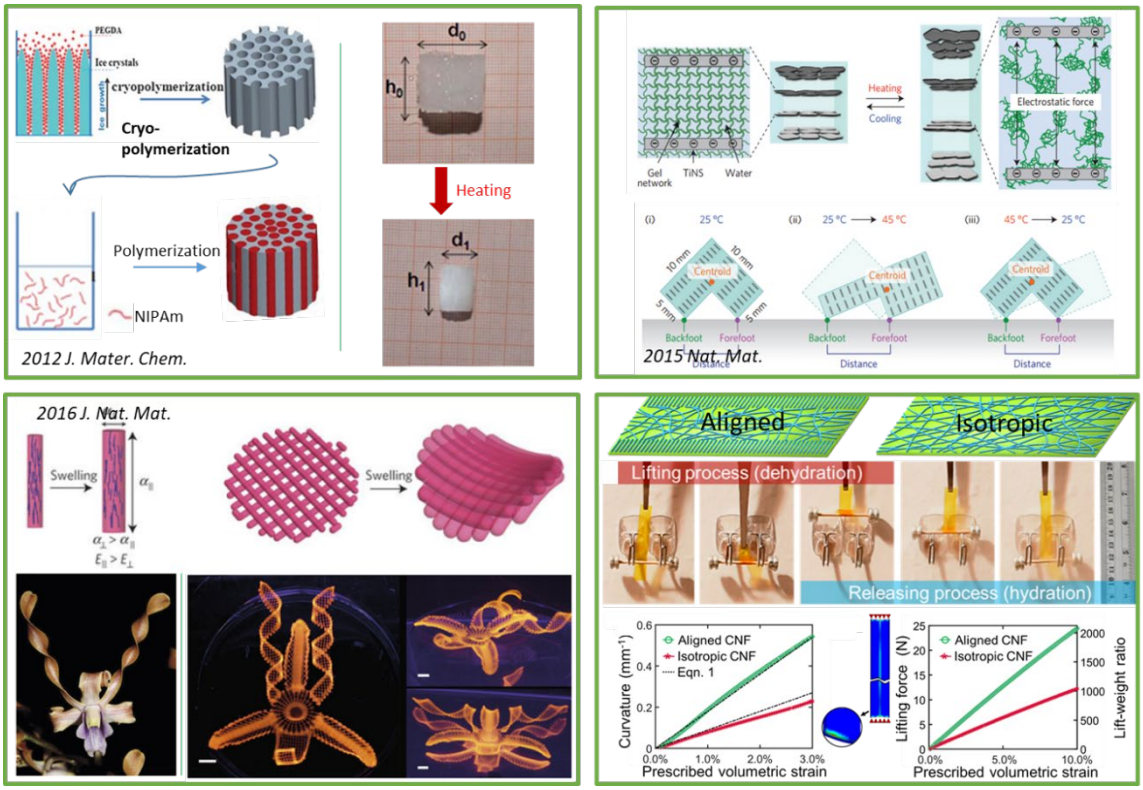

Figure 5.3 Applications of anisotropic hydrogels in bio-mimicking actuation. (a) Anisotropic swelling of a hydrogel with unidirectional dual-network microstructure [154]. (b) Biped hydrogel actuator enabled by unidirectional electrostatic repulsive interaction [30]. (c) 4D-printed hydrogel structure with aligned cellulose fibrils achieving complex deformations [16]. (d) Hygro-sensitive actuator with enhanced lifting performance enabled by selectively aligned cellulose nanofibers.

As a result of the distinctive and intrinsic anisotropy, the novelty and significance of anisotropic hydrogels has been demonstrated in sundry applications such as bio-mimicking actuation. For example, as shown in Figure 5.3a, the anisotropic PEG– PNIPAM hydrogel reported in Ref [154] has an aligned porous PEG scaffold, exhibiting an anisotropy of 2 during swelling/shrinking. Such an anisotropic deformation may simplify the design and fabrication of fluid control systems. Figure 5.3b shows the structure of a hydrogel with electrostatically interacting nano-fillers and demonstrates its application in a unidirectional progressing biped soft robot. Figure 5.3c shows a complicated shape transform achieved by a 4D printed anisotropic hydrogel with aligned cellulose fibers [16]. The deformational behavior of the hydrogel can be modulated by the localized fiber orientation as well as the woven pattern.

5.1.3 Chemically treated cellulose nanofibers (CNF) and anisotropic wood hydrogel

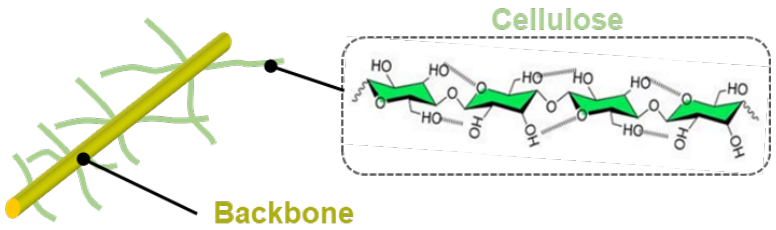

Figure 5.4 Structure of chemically treated cellulose nanofiber (CNF). Bundled CNFs serve as backbone providing strength and stiffness. The exposed CNFs is free to associate water molecules via hydrogen bonds.

Apart from inventing artificial anisotropic hydrogels, a brand-new avenue is directly reorganizing, at the microscopic level, nature's existing organic materials as building blocks to create anisotropic hydrogels which do not otherwise exist in nature. Since the

structures of nature's living organisms are almost anisotropic, anisotropic hydrogel can be made by engineering a hydrophilic polymer network upon the anisotropic structures already existing in the living organisms. Recently, we chemically process nature wood by exposing the hydrophilic cellulose nanofibers naturally bundled within the wood cell walls, and thereafter form a cross-linked cellulose nanofiber network, which in turn becomes a hydrogel in contact with water molecule [155], [156].

The structure of an individual post-treatment CNF is featured by a cellulose bundle serving as the backbone with cellulose molecule chains tethered on the backbone surface, as illustrated in Figure 5.4. Compared to the pristine nature wood cellulose fibers, the treated CNFs possess an increased number of surface molecule chains. Therefore, more hydroxyl functional groups are exposed and become available to form hydrogen bonds. Once immersed in water, a CNF biopolymer network percolates through the material in form of a hydrogen bonding system connecting the intermolecular cellulose hydroxyl groups in assistance of water molecules. The CNF/water system, by nature, is a microfiber reinforced hydrogel: The cellulose fibers packed into the backbone bundle acts as the reinforcement phase who provides stiffness and mechanical strength; the others exposed to the surface forms a hydrophilic network, absorbing and holding water molecules, as illustrated in Figure 5.5.

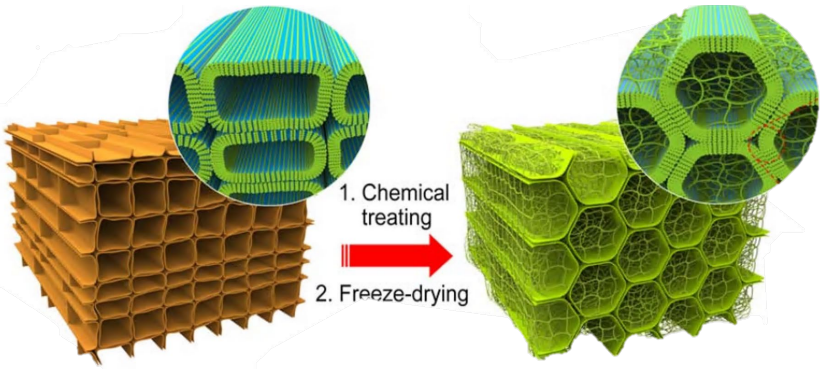

Figure 5.5 Schematic of cellulose hydrogel processed from nature wood. After the chemical treatment, more hydroxyl functional groups are exposed in the wood cell along the free cellulose bundles. Through the formation of hydrogen bonds, the cellulose fibers cross-linked as a biopolymer network.

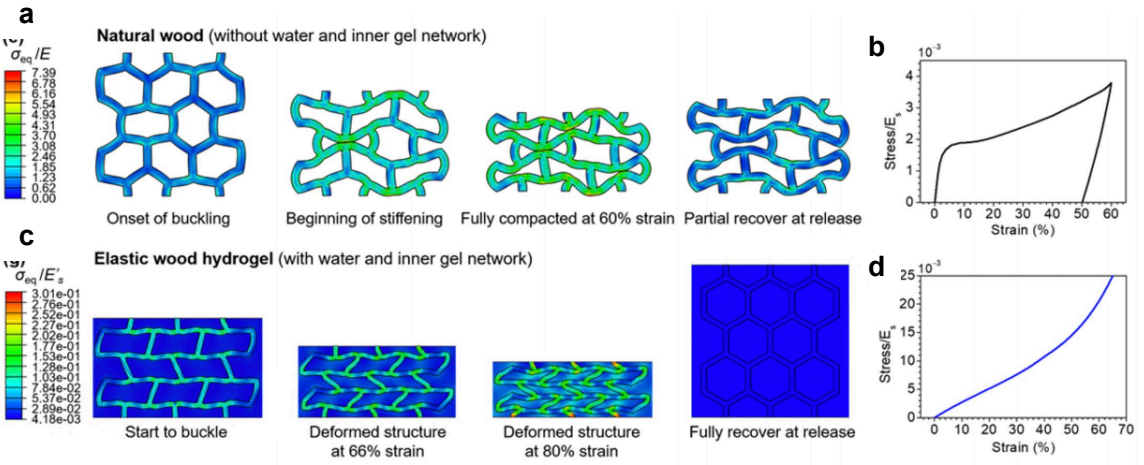

Figure 5.6 Property of super durable elastic wood hydrogel formed by cross-linking the intra-cellular cellulose nanofibers. (a) Deformation sequence of a representative structure of natural wood when compressive force is applied at various strains. Contour shows the von Mises equivalent stress normalized by the elastic modulus of the cell wall constituent material; (b) loading-unloading curve of the natural wood compressed to maximum strain of 60%; (c) deformation sequence of a representative structure of elastic wood when compressive force is applied at various strains - the cell wall starts to buckle at an applied strain of 48%; the deformed structure at an applied strain of 66%; deformed structure at an applied strain of 80%; and the fully recovered structure when fully unload; (d) loading-unloading curve of the elastic wood compressed to a strain of 60%.

The processed wood hydrogel[6] not only inherits the anisotropic nature of the pristine wood, but also has an inner-cellular hydrogel formed by the hydrogen bonds between water molecules and the hydroxyl groups on the free cellulose fibers. Compared to the nature wood featured by a cellular microscopic structure, the hallow cells of the processed wood are filled with the cellulose hydrogel which provide superb elastic properties. As shown in Figure 5.6, the cross-linked cellulose fiber network saturated with water inside open channels is modeled as a hyperelastic material, while the cellular walls are thinner than those in natural wood, given the partial disintegration of the cell wall into cellulose fibers. The deformation sequence of the simulation model of wood hydrogel under lateral compression is shown in Figure 5.6c. The mechanical constraint of the hyperelastic cellulose fiber network inside the open channels leads to a rather regulated and coordinated deformation of the cellular walls to accommodate the lateral compression, in sharp contrast to the random buckling and collapse of the cellular walls in natural wood under compression (Figure 5.6a). The hyperelastic nature of the cellulose fiber network also results in the steady stiffening of the overall structure, as the lateral compressive strain increases (Figure 5.6d). Upon release of the compressive load, the hyperelastic cellulose fiber network can help the wood hydrogel to recover to its original shape, with negligible residue deformation.

Another application of the cellulose nanofiber based anisotropic hydrogel is shown in Figure 5.3d, a hygro-sensitive actuator with selectively aligned cellulose fibers along the

[6] The experiment is conducted by Dr. Chaoji Chen from Prof. Liangbing Hu's research group, Department of Materials Science and Engineering, University of Maryland, College Park.

width of the CNF/Polyimide bilayer[7]. Benefit from its anisotropic microstructure, the present actuator outperforms other designs of its kind in response time and lifting weight ratio and exhibits a doubled lifting force than its isotropic counterpart.

5.1.4 Motivation of the constitutive model for fiber-reinforced hydrogel

Despite its promising outlook in many aspects, there is still a profound lack of well formulated mechanical models to properly model and to predict the deformational behavior of anisotropic hydrogels, especially a class of fiber-reinforced anisotropic hydrogels. Existing modeling techniques tend to fallaciously model the anisotropic swelling in a fiber-reinforced hydrogel by considering an anisotropic thermal expansion of a mechanically isotropic material, or alternatively by combining an isotropic thermal expansion with a mechanically anisotropy [157]. This approach is questionable because in reality not only the solvent uptake/release is affected by the fiber interaction but also the mechanical properties are also altered by the fiber orientation. Another method that entails a free energy density function attempts to incorporate the anisotropy in an anisotropic strain energy density for the polymer network [157]–[159]. Such a treatment appropriately addresses the coupled chemo-mechanical swelling of the material; however, it fails to provide sufficient insight in the microscopic pictures of the fiber by using an invariant-based phenomenological strain energy [158].

[7] The experiment is conducted by Dr. Yudi Kuang from Prof. Liangbing Hu's research group, Department of Materials Science and Engineering, University of Maryland, College Park.

In order to properly quantify the deformational behavior of a class of fiber-reinforced anisotropic hydrogel, we propose a constitutive model in this chapter. The rest of this chapter is organized as follows. In section 5.2, we construct the constitutive models by resorting to a micromechanical treatment of the strain energy associated with the deformed microfibers. The restriction of limited number of microfiber families is relaxed, and the microfibers can be described more precisely by a directional distribution. The equations of states, i.e., the stress-deformation relations are derived in the most generic form. In section 5.3, applications of the FRG constitutive model are explored for hydrogels with different types of fiber distributions. The anisotropic mechanical behaviors of these FRGs are investigated. In section 5.4, the theory is applied to a humidity-sensitive soft actuator where a thin layer of aligned cellulose nanofibers (CNFs) drying on a substrate. The bending actuation due to the dehydration of the aligned CNF film is compared with the isotropic CNF film. Lastly in section 5.5, the main finding of the paper is summarized as a conclusion remark.

5.2 Constitutive model for microfiber reinforced anisotropic hydrogels

Let w_{gel} denote the free energy per unit volume of a deformed fiber reinforced hydrogel. From a thermodynamics perspective, w_{gel} can be postulated as a summation of the strain energy associated with the deformation and the entropic free energy stemming from the mixing of the hydrogel polymer network and the water molecules. In the same vein, the total free energy density of a deformed fiber reinforced can be calculated by adding the free energy stored in the deformed microfibers to the gel matrix, namely,

$$w = (w_{\text{network}} + w_{\text{mix}}) + w_{\text{fiber}} \tag{5.1}$$

where w_{network} stands for the strain energy of the polymer network, w_{network} and w_{mix} add up to the free energy of the hydrogel phase w_{gel}. Since w bears the significance of the total energy per unit volume, it is necessary to identify a reference state based on which quantifications of the hydrogel phase energy and fiber energy both become convenient.

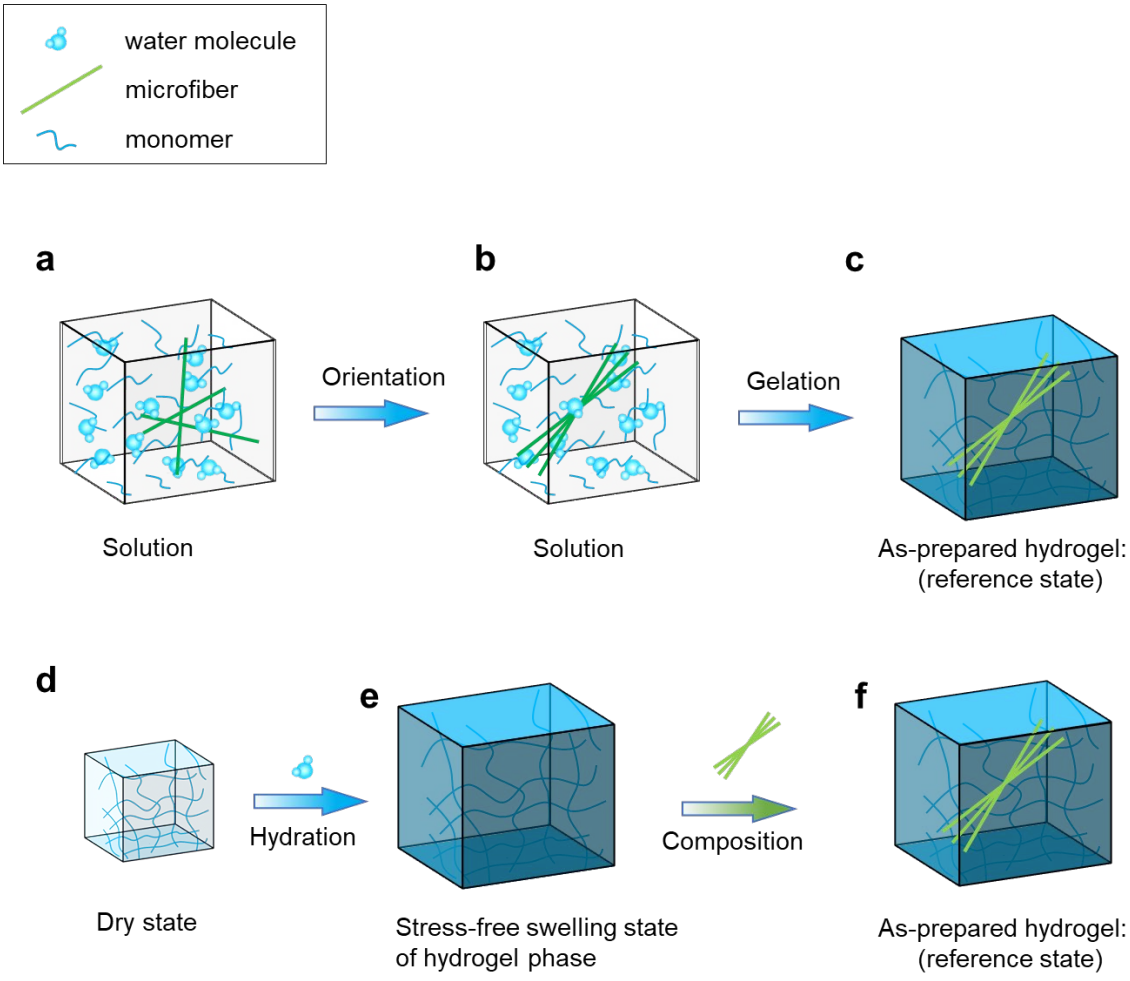

Figure 5.7 Schematic of the structures of a microfiber-reinforced anisotropic hydrogel. (a) ~ (c) A step-by-step representation of fiber reinforced hydrogel preparation processes. (a) A solution mixture of solvent, monomer molecules, and microfibers. (b) Orientation of the fibers. (c) As-prepared FRG. Along with (d) ~ (f) an imaginary composition process of the fiber reinforced hydrogel. (d) The water-free dry state of the hydrogel phase only. (e) The fully hydrated swelling

state of the hydrogel phase. There is no macroscopic net stress in the hydrogel since the stress due to network stretch and osmotic stress balance out. (f) The composition of the hydrogel and fiber phases by replacing fibers back to the stress-free hydrogel matrix.

5.2.1 The as-fabricated hydrogel as the reference state

Figure 5.7a~c describes a representative preparation process of a fiber reinforced hydrogel (FRG): As a first step, monomers and microfibers are mixed in a solution. Then the external driving force is applied to orient the microfiber to the desired direction and extent of dispersion. Lastly, gelation agent is added to the solution to crosslink the monomers into polymeric network. In condition that the monomers are uniformly dissolved in the solvent and each monomer molecule is surrounded by abundant water molecules, it can be assumed that the presence of microfibers does not disturb or alter the gelation of the hydrogel phase. As a result, gelation and cross-linking do not induce any localized stress between the gel and fiber phases.

The above gelation process is easily explicable as a two-step imaginary procedure sketched in Figure 5.7d~f. To arrive at the same fiber reinforced hydrogel in Figure 5.7c which we are concerned with, let us first consider the dry state of the polymer network itself. Next, the hydration step brings the dry polymer network to a free-swelling state of the hydrogel phase. Such a free-swelling state is characterized by zero net stresses through the hydrogel since the stress due to network stretch and osmotic stress balance out. As a last step, the composition of the FRG by replacing the microfiber phase back to the stress-free hydrogel matrix ensures that the as-prepared FRG is consequently stress-free for both hydrogel and fiber phases. In other words, the existence of microfibers in the monomer aqueous solution

does not intervene the gelation process chemically. In reverse, the gelation processes itself is also independent of the microfibers mechanically.

Therefore, it becomes intuitive and convenient to choose the as-prepared state of the FRG as the reference state. Those quantities in Eq. (1) now can be mapped to the as-made free-swelling state and represent the energies per unit volume of the reference state. Because the assumption that the microfibers do not have any chemical or mechanical bearings on the gelation/cross-linking, the reference state can be determined by the free-swelling condition of the pure hydrogel phase. Note that expect for the microfibers, there is no other source of anisotropy in the hydrogel phase. Consequently, the gelation of the hydrogel phase per se is still isotropic. According to [Ref Hong], a freestanding hydrogel immersed in water swells with identical principal stretches $\Lambda_1=\Lambda_2=\Lambda_3=\Lambda_0$ with respect to the dry polymer state, where Λ_0 denotes the isotropic free-swelling stretch for the hydrogel phase.

$$Nv(\Lambda_0^{-1}-\Lambda_0^{-3})+\log(1-\Lambda_0^{-3})+\Lambda_0^{-3}+\chi\Lambda_0^{-6}-\mu/k_{\mathrm{B}}T=0 \qquad (5.2)$$

where N is the number of covalent crosslinks per unit volume of the dry polymer, v is the volume of one water molecule, χ is the Flory-Huggins parameter measuring the hydrophilicity of the polymer network, μ denotes the chemical potential of water, k_{B} is the Boltzmann constant, and T is the temperature in Kelvin scale.

Once the as-fabricated state is determined by $\Lambda 0$, we are ready to construct the total free-energy density function in Eq. (1) with respect to the reference state. Let $\boldsymbol{X}$ denote the coordinate of a material point in the undeformed reference state of FRG. After deformation

it moves to $\boldsymbol{x}$, and the deformation gradient tensor $\mathbf{F}=\mathrm{d}\boldsymbol{x}/\mathrm{d}\boldsymbol{X}$, expressed in the principal coordinates,

$$\mathbf{F}=\begin{bmatrix}\lambda_1 & & \\ & \lambda_2 & \\ & & \lambda_3\end{bmatrix} \tag{5.3}$$

where λ_i is the stretch in the ith principal direction, and the determent of the deformation gradient gives the volume ratio $J=\det(\mathbf{F})$. At the same material point, the deformation gradient tensor for the hydrogel phase is $\mathbf{F}^\mathrm{g}$ and is a function of $\mathbf{F}$,

$$\mathbf{F}^\mathrm{g}=\begin{bmatrix}\lambda_1^\mathrm{g} & & \\ & \lambda_2^\mathrm{g} & \\ & & \lambda_3^\mathrm{g}\end{bmatrix} \tag{5.4}$$

similarly, λ_i^g is the stretch of the hydrogel phase in the ith principal direction of $\mathbf{F}^\mathrm{g}$. Therefore, the free energy of the hydrogel phase per unit volume of the FRG in the reference state takes the form

$$\begin{aligned}\frac{w_\mathrm{gel}}{\frac{k_\mathrm{B}T}{v}}=\frac{Nv(1-\phi)}{2\Lambda_0^3}\left\{\left[\left(\lambda_1^\mathrm{g}\right)^2+\left(\lambda_2^\mathrm{g}\right)^2+\left(\lambda_3^\mathrm{g}\right)^2\right]\Lambda_0^2-3-2\log\eta\right\}\\ -\frac{1-\phi}{\Lambda_0^3}\left[(\eta-1)\log\left(\frac{\eta}{\eta-1}\right)+\frac{\chi}{\eta}+\frac{\mu}{k_\mathrm{B}T}(\eta-1)\right]=0\end{aligned} \tag{5.5}$$

where ϕ stands for the fiber volume fraction so that $(1-\phi)$ the hydrogel volume fraction, $\eta=\Lambda_0^3\lambda_1^\mathrm{g}\lambda_2^\mathrm{g}\lambda_3^\mathrm{g}$ is the volume ratio of the hydrogel phase relative to the completely dehydrated state of the polymer network. If both the polymer network and the water molecules are incompressible, the volume of the swollen hydrogel is simply a summation

of the volume of both parties, the corollary of that is that the volume ratio η can be further expressed as

$$\eta = 1 + vC \tag{5.6}$$

We assume there is no fiber-fiber interaction, thus the strain energy associated with the fiber deformation only stems from the stretch or compression (length change) of fiber. In the language of mechanics of composite materials, the fiber reinforcement phase is dilute. As a single fiber filament must follow the entire FRG deformation in an affine manner, the length change of the fiber can be calculated by projecting **F** to the fiber orientation,

$$\lambda^{\mathrm{f}} = [(\mathbf{F}\boldsymbol{N})^{\mathbf{T}}\mathbf{F}\boldsymbol{N}]^{\frac{1}{2}} = \sqrt{(\lambda_1 \sin\phi\cos\theta)^2 + (\lambda_2 \sin\phi\sin\theta)^2 + (\lambda_3 \cos\phi)^2} \tag{5.7}$$

where $\boldsymbol{N}$=(sinϕcosθ, sinϕsinθ, cosϕ) is the direction normal of the filament. Consequently, the energy stored in one strained fiber can be expressed as a function of the FRG deformation and the fiber orientation, that is, $u_{\mathrm{fiber}} = u_{\mathrm{fiber}}(\mathbf{F}|\boldsymbol{N})$. If the orientation of the fibers follows a distribution, the strain energy per unit volume of the reference state becomes [160], [161]

$$w_{\mathrm{fiber}} = \phi \oiint u_{\mathrm{fiber}}(\mathbf{F}|\boldsymbol{N})\, \rho(\boldsymbol{N}) ds \tag{5.8}$$

To account for the fibers in all possible orientations, the integral extends over a unit sphere in the reference state, $\rho(\boldsymbol{N})$ is the probability density of finding a fiber in $\boldsymbol{N}$ direction, ds= sin$\phi d\phi d\theta$ is the area element.

By assembling Eqs. (5) and (7) into Eq. (1), we arrive at an expression for the total strain energy density of FRG

$$\frac{w}{k_{\mathrm{B}}T/v} = \frac{Nv(1-\phi)}{2\Lambda_0^3}\left\{\left[\left(\lambda_1^{\mathrm{g}}\right)^2 + \left(\lambda_2^{\mathrm{g}}\right)^2 + \left(\lambda_3^{\mathrm{g}}\right)^2\right]\Lambda_0^2 - 3 - 2\log\eta\right\} - \frac{1-\phi}{\Lambda_0^3}\left[(\eta-1)\log\left(\frac{\eta}{\eta-1}\right) + \frac{\chi}{\eta} + \frac{\mu}{k_{\mathrm{B}}T}(\eta-1)\right] + \oiint \phi u_{\mathrm{fiber}}(\mathbf{F}|\boldsymbol{N})\,\rho(\boldsymbol{N})ds \tag{5.9}$$

At this point, we have in the above strain energy function the material property-related parameters: N being the crosslinking density per unit volume of dry polymer, χ being the polymer network hydrophilicity parameter, ϕ being the volume fraction of fibers in the reference state, Λ_0 being the free-swelling ratio of the hydrogel phase at the as-prepared reference state, μ being the solvent chemical potential; and the constants: k_{B} being the Boltzmann constant, v being the water molecule volume; along with the deformation gradient tensors $\mathbf{F}$ and $\mathbf{F}^{\mathrm{g}}$ as variables. The only question left to be answered is how the deformation of the hydrogel phase $\mathbf{F}^{\mathrm{g}}$ is related to the deformation of the entire FRG $\mathbf{F}$. In the next part, we will link $\mathbf{F}^{\mathrm{g}}$ to F under the special case where the reinforcement phase falls into the category of microfibers.

5.2.2 Relation between the deformation of the FRG and the deformation of its constituent phases

For microfiber as a reinforcement phase, its volume is usually much smaller than that of the hydrogel phase[153], [155], [156], [162] , $\phi \to 0$, therefore the microfibers can be modeled as one-dimensional volume-less elastically deformable bodies who experience only length change prescribed by the entire FRG deformation in terms of an affine projection. If the fibers occupy little space, the total volume change of FRG is contributed

by the water take-up or relief of the hydrogel phase, that is, the volume ratio of FRG and the volume ratio of only the hydrogel phase becomes virtually the same, i.e.,

$$J = \eta \tag{5.10}$$

One may further picturize the deformation of the entire FRG as the deformation of a hydrogel and, on top of that, the affine deformation of some volume-less reinforcement fibers. The deformation of the hydrogel phase is the same as the entire FRG.

$$\begin{bmatrix} \lambda_1^{\mathrm{g}} & & \\ & \lambda_2^{\mathrm{g}} & \\ & & \lambda_3^{\mathrm{g}} \end{bmatrix} = \begin{bmatrix} \lambda_1 & & \\ & \lambda_2 & \\ & & \lambda_3 \end{bmatrix} \tag{5.11}$$

In cases where Eqs. (6) and (7) both apply, Eq. (9) can be reduced to:

$$\begin{aligned} \frac{w}{k_{\mathrm{B}}T/v} = \frac{Nv}{2\Lambda_0^3}\{[\lambda_1^2 + \lambda_2^2 + \lambda_3^2]\Lambda_0^2 - 3 - 2\log J\} \\ - \frac{1}{\Lambda_0^3}\left[(J-1)\log\left(\frac{J}{J-1}\right) + \frac{\chi}{J} + \frac{\mu}{k_{\mathrm{B}}T}(J-1)\right] \\ + \frac{1}{k_{\mathrm{B}}T/v}\oiint \tilde{u}_{\mathrm{fiber}}(\mathbf{F}|\boldsymbol{N})\,\rho(\boldsymbol{N})ds \end{aligned} \tag{5.12}$$

Note that $\lim_{\phi\to 0} \phi u_{\mathrm{fiber}}(\mathbf{F}|\boldsymbol{N}) = \tilde{u}_{\mathrm{fiber}}(\mathbf{F}|\boldsymbol{N})$, the fiber strain energy does not vanish, regardless ϕ is efficiently small for volume calculation. In the following discussions, we will focus our attention on the cases of microfiber reinforced hydrogels.

5.2.3 A mechanical model suitable for microfiber as reinforcement phase and the equations of state

Differentiating the free-energy density function expressed in Eq. (12), we obtain the first Piola-Kirchhoff stresses

$$\begin{aligned}\frac{S_i}{k_{\mathrm{B}}T/v} &= \frac{\partial}{\partial\lambda_i}\left(\frac{w}{k_{\mathrm{B}}T/v}\right)\\ &= \frac{Nv}{\Lambda_0^2}\left(\Lambda_0\lambda_i - \Lambda_0^{-1}\lambda_i^{-1}\right)\\ &+ \Lambda_0^{-3}\lambda_i^{-1}\left[J\log\left(1-\frac{1}{J}\right)+1+\frac{\chi}{J}-\frac{\mu}{kT}J\right]\\ &+ \frac{1}{k_{\mathrm{B}}T/v}\oint\iint\frac{\partial\tilde{u}_{\mathrm{fiber}}}{\partial\lambda^{\mathrm{f}}}\frac{\partial\lambda^{\mathrm{f}}}{\partial\lambda_i}\rho ds\end{aligned} \tag{5.13}$$

The first two terms in Eq. (13) are the stress due to hydrogel phase and the last term is contributed by the length change of the microfibers. A common treatment for fiber elasticity is to use a linear elastic model whose stiffness is the same in tensile and compressive regime. However, given its large aspect ratio, the microfibers of concern should be more deformable to compress than to stretch. Hereby, we adopt the two-parameter elastic model for a single microfiber attributed to Fung [163] and originally intended for soft tissue fibers [164],

$$\frac{\partial\tilde{u}_{\mathrm{fiber}}}{\partial\lambda^{\mathrm{f}}} = \frac{E}{B}\left[e^{B(\lambda^{\mathrm{f}}-1)}-1\right] \tag{5.14}$$

where E and B are the two material-property-related parameters: E is the stiffness at infinitesimal strain; and B is a positive shape parameter. The dependence of the fiber stress-stretch relation on parameter B is shown in Figure 5.8a. When B is larger, the stress-stretch

curve becomes curlier and the tensile stiffness is much higher than the compression stiffness. When B is zero, the mechanical behavior of the microfiber reduces to a linear elastic spring. The effect of E is straightforward, as is shown in Figure 5.8b: The higher the E, the stiffer the microfiber. In addition, from Eq. (7) we obtain

$$\frac{\partial \lambda^{\mathrm{f}}}{\partial \lambda_1} = \lambda_1 \sin^2\phi \cos^2\theta / \lambda^{\mathrm{f}} \tag{5.15-1}$$

$$\frac{\partial \lambda^{\mathrm{f}}}{\partial \lambda_2} = \lambda_2 \sin^2\phi \sin^2\theta / \lambda^{\mathrm{f}} \tag{5.15-2}$$

$$\frac{\partial \lambda^{\mathrm{f}}}{\partial \lambda_3} = \lambda_3 \cos^2\phi / \lambda^{\mathrm{f}} \tag{5.15-3}$$

For the sake of simplicity, we define the dimensionless stiffness parameter of the microfiber $\bar{E} = Ev/k_{\mathrm{B}}T$. Upon assembly, we have a generic expression of the first Piola-Kirchhoff stresses for a FRG with arbitrary fiber distributions,

$$\begin{aligned}\frac{S_1}{k_{\mathrm{B}}T/v} = \frac{Nv}{\Lambda_0^2}\left(\Lambda_0\lambda_1 - \Lambda_0^{-1}\lambda_1^{-1}\right) + \Lambda_0^{-3}\lambda_1^{-1}\left[J\log\left(1-\frac{1}{J}\right) + 1 + \frac{\chi}{J} - \frac{\mu}{kT}J\right] \\ + \oiint \frac{\bar{E}}{B}\left[e^{B(\lambda^{\mathrm{f}}-1)} - 1\right]\lambda_1 \sin^2\phi \cos^2\theta/\lambda^{\mathrm{f}}\rho(\phi,\theta)\sin\phi d\phi d\theta\end{aligned} \tag{5.16-1}$$

$$\begin{aligned}\frac{S_2}{k_{\mathrm{B}}T/v} = \frac{Nv}{\Lambda_0^2}\left(\Lambda_0\lambda_2 - \Lambda_0^{-1}\lambda_2^{-1}\right) + \Lambda_0^{-3}\lambda_2^{-1}\left[J\log\left(1-\frac{1}{J}\right) + 1 + \frac{\chi}{J} - \frac{\mu}{kT}J\right] \\ + \oiint \frac{\bar{E}}{B}\left[e^{B(\lambda^{\mathrm{f}}-1)} - 1\right]\lambda_2 \sin^2\phi \sin^2\theta/\lambda^{\mathrm{f}}\rho(\phi,\theta)\sin\phi d\phi d\theta\end{aligned} \tag{5.16-2}$$

$$\begin{aligned}\frac{S_3}{k_{\mathrm{B}}T/v} = \frac{Nv}{\Lambda_0^2}\left(\Lambda_0\lambda_3 - \Lambda_0^{-1}\lambda_3^{-1}\right) + \Lambda_0^{-3}\lambda_3^{-1}\left[J\log\left(1-\frac{1}{J}\right) + 1 + \frac{\chi}{J} - \frac{\mu}{kT}J\right] \\ + \oiint \frac{\bar{E}}{B}\left[e^{B(\lambda^{\mathrm{f}}-1)} - 1\right]\lambda_3 \cos^2\phi/\lambda^{\mathrm{f}}\rho(\phi,\theta)\sin\phi d\phi d\theta\end{aligned} \tag{5.16-3}$$

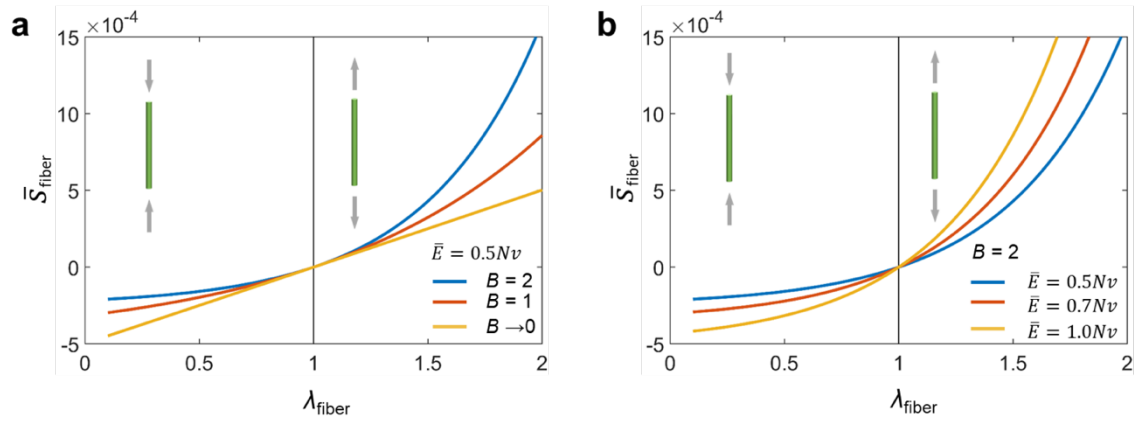

Figure 5.8 Elastic properties of a single microfiber with asymmetric stiffness in tension and in compression. (a) The dependence of the fiber stress-stretch relation on parameter B. (b) The dependence of the fiber stress-stretch relation on parameter $\bar{E}$.

In the next section, we will examine the anisotropic behaviors of FRG for three distinct fiber system configurations: anisotropic hydrogel with perfectly aligned microfibers, anisotropic hydrogel with microfibers uniformly distributed in a plane, and anisotropic hydrogel with microfibers following in-plane von Mises distribution. In all the application cases to come in the following sections, if not otherwise mentioned, we keep the choice of parameters being: Nv=1×10^{-3}, χ=0.2, μ_0=0.

5.3 Applications of the constitutive model and the anisotropic mechanical behaviors of microfiber reinforced hydrogels

5.3.1 Anisotropic hydrogel with perfectly aligned microfibers

The configuration of the hydrogel with perfectly aligned microfibers are depicted schematically in Figure 5.9a. The fibers are arranged in parallel in the material direction 1. In the two transverse directions 2 and 3, the material is isotropic. The equations of states take the form:

$$\frac{S_1}{k_B T/v} = \frac{Nv}{\Lambda_0^2}\left(\Lambda_0\lambda_1 - \Lambda_0^{-1}\lambda_1^{-1}\right) + \Lambda_0^{-3}\lambda_1^{-1}\left[J\log\left(1-\frac{1}{J}\right) + 1 + \frac{\chi}{J} - \frac{\mu}{kT}J\right] + \frac{\bar{E}\left[e^{B(\lambda_1-1)} - 1\right]}{B} \tag{5.17-1}$$

$$\frac{S_2}{k_B T/v} = \frac{Nv}{\Lambda_0^2}\left(\Lambda_0\lambda_2 - \Lambda_0^{-1}\lambda_2^{-1}\right) + \Lambda_0^{-3}\lambda_2^{-1}\left[J\log\left(1-\frac{1}{J}\right) + 1 + \frac{\chi}{J} - \frac{\mu}{kT}J\right] \tag{5.17-2}$$

$$\frac{S_3}{k_B T/v} = \frac{Nv}{\Lambda_0^2}\left(\Lambda_0\lambda_3 - \Lambda_0^{-1}\lambda_3^{-1}\right) + \Lambda_0^{-3}\lambda_3^{-1}\left[J\log\left(1-\frac{1}{J}\right) + 1 + \frac{\chi}{J} - \frac{\mu}{kT}J\right] \tag{5.17-2}$$

We first study the stress-free swelling and dehydration behavior of such a FRG from its as-synthesized reference state. This problem can be modeled using the stress-free conditions in all material directions, i.e,

$$s_i = 0 \tag{5.18}$$

with *i*=1, 2, and 3. The above Eq. (18) has virtually three equations for solving the three principal stretches.

As a demonstration, the stress-free swelling/dehydration is solved at $\bar{E} = Nv$, $B = 1$. With the chemical potential of the solvent μ/kT varying from 0~−0.05, the FRG exhibits an anisotropic contraction, as shown in Figure 5.9b. Due to the existence of the microfibers, the stiffness in direction 1 is reinforced, therefore the deformation is less when compared to the contraction in the two transverse directions. In Figure 5.9b it is also plotted as a baseline case the swelling curve of an isotropic hydrogel by taking the stiffness of the microfiber $\bar{E} = 0$. When $\bar{E}$ increases from 0, the FRG starts to acquire anisotropic behavior and swelling curve diverges into two distinct curves: λ_1 located above and $\lambda_{2,3}$ below the baseline.

Next, we study the anisotropic uniaxial tensile behavior of this FRG. Stretching in microfiber direction (Figure 5.10a), the stress condition for the problem is represented by,

$$s_1 \neq 0, s_2 = s_3 = 0 \tag{5.19}$$

Similarly, in the transverse direction (Figure 5.10b), the equations are,

$$s_2 \neq 0, s_1 = s_3 = 0 \tag{5.20}$$

The stress-stretch relations in both 1 and 2 directions are solved for four combinations of the microfiber properties as shown in Figure 5.10c~f. The stress in the microfiber direction is higher than in the transverse direction due to the reinforcement effect. Moreover, the anisotropy becomes more pronounced for microfibers with higher tensile stiffness, i.e., higher E and B. However, no apparent difference is observed between the transverse stress-stretch relations in all these four cases. This can be attributed to the fact that there is no intrinsic inter-fiber interaction in the transverse direction and in such direction the material property is exclusively dictated by the hydrogel phase. One can therefore use the stress-stretch curve in the transverse direction to calibrate the material parameters for the hydrogel phase, and then use the data in the fiber direction to determine the fiber stiffness.

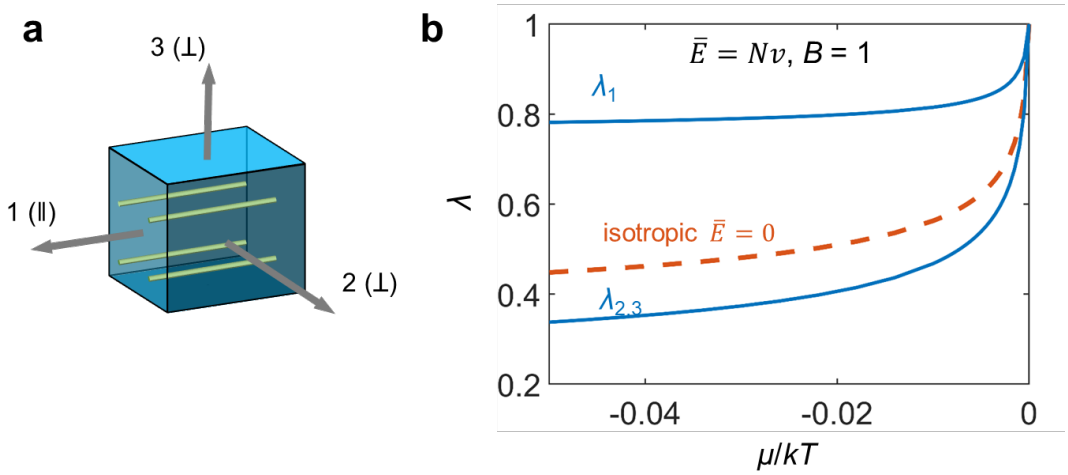

Figure 5.9 Anisotropic free-swelling of an anisotropic hydrogel with microfibers perfectly aligned in one direction. (a) Schematic of the anisotropic hydrogel with microfibers perfectly aligned in one direction. (b) Anisotropic deformation due to stress-free dehydration with comparison to the isotropic hydrogel. The case is calculated with fiber property parameter $\bar{E} = Nv, B = 1$.

Another aspect of the FRG anisotropic mechanical behavior is the contraction of the perpendicular cross-section during the uniaxial tension test. When subjected to tension in direction 2, the cross-section is the 3-1 plane. According to the FRG material coordinates (shown in Figure 5.11a), direction 1 is the direction in which all the microfibers are oriented, whereas direction 3 is a transverse direction. Therefore, the contraction of 3-1 plane is anisotropic when elongate the FRG in direction 2. The shape of the cross-section is represented by the trajectory of λ_3-λ_1 as λ_2 increases from 1 to 6 (arrow direction). A family of these trajectories are parametrized by the stiffness of microfibers E. The baseline case of isotropic hydrogel (E=0) exhibits an equal contraction since λ_3-λ_1 extends along the 45° line. Once the microfiber stiffness becomes positive, the λ_3-λ_1 curve deviates from the isotropic case. The contraction in the fiber direction is smaller compared to the contraction in the transverse direction, thus for E>0 the λ_3-λ_1 curves appear below the isotropic line. Figure 5.11c plots the volumetric ratio as a function of the applied stretch in

the transverse direction 1, the monotonically increasing J indicates that the FRG continues to absorb water as it gets elongated. The FRG with stiffer microfibers tends to be more capable of water uptake at same λ_2.

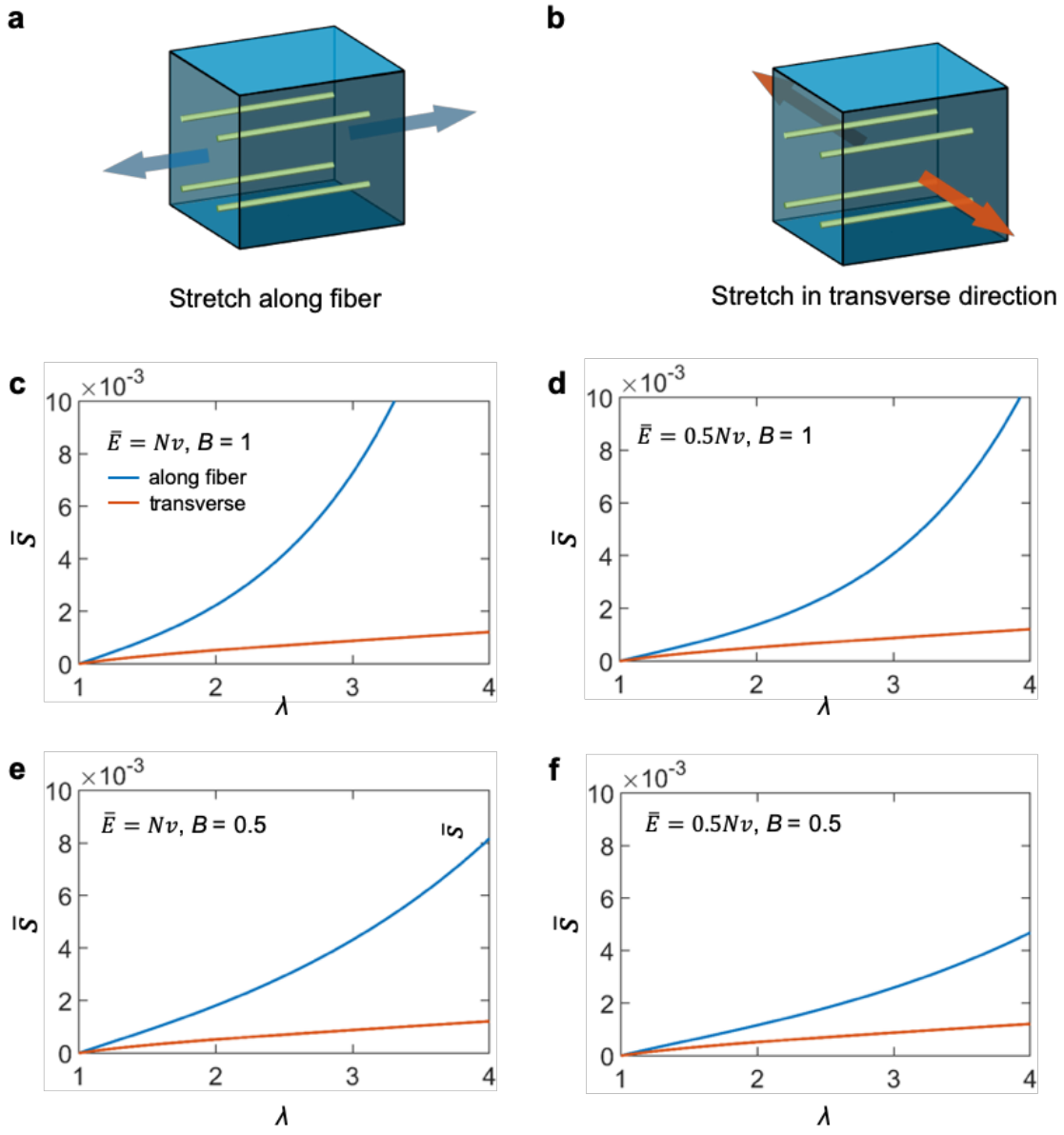

Figure 5.10 Uniaxial tensile behavior of anisotropic hydrogel with microfibers perfectly aligned in one direction. Schematic of uniaxial loading (a) along the fiber distribution direction and (b) in the transverse direction. Relations between the dimensionless nominal stress and stretch along the fiber

distribution plane and along the transverse direction for hydrogels with different fiber properties: (c) $\bar{E} = Nv$, $B = 1$, (d) $\bar{E} = 0.5Nv$, $B = 1$, (e) $\bar{E} = Nv$, $B = 0.5$, and (f) $\bar{E} = 0.5Nv$, $B = 0.5$.

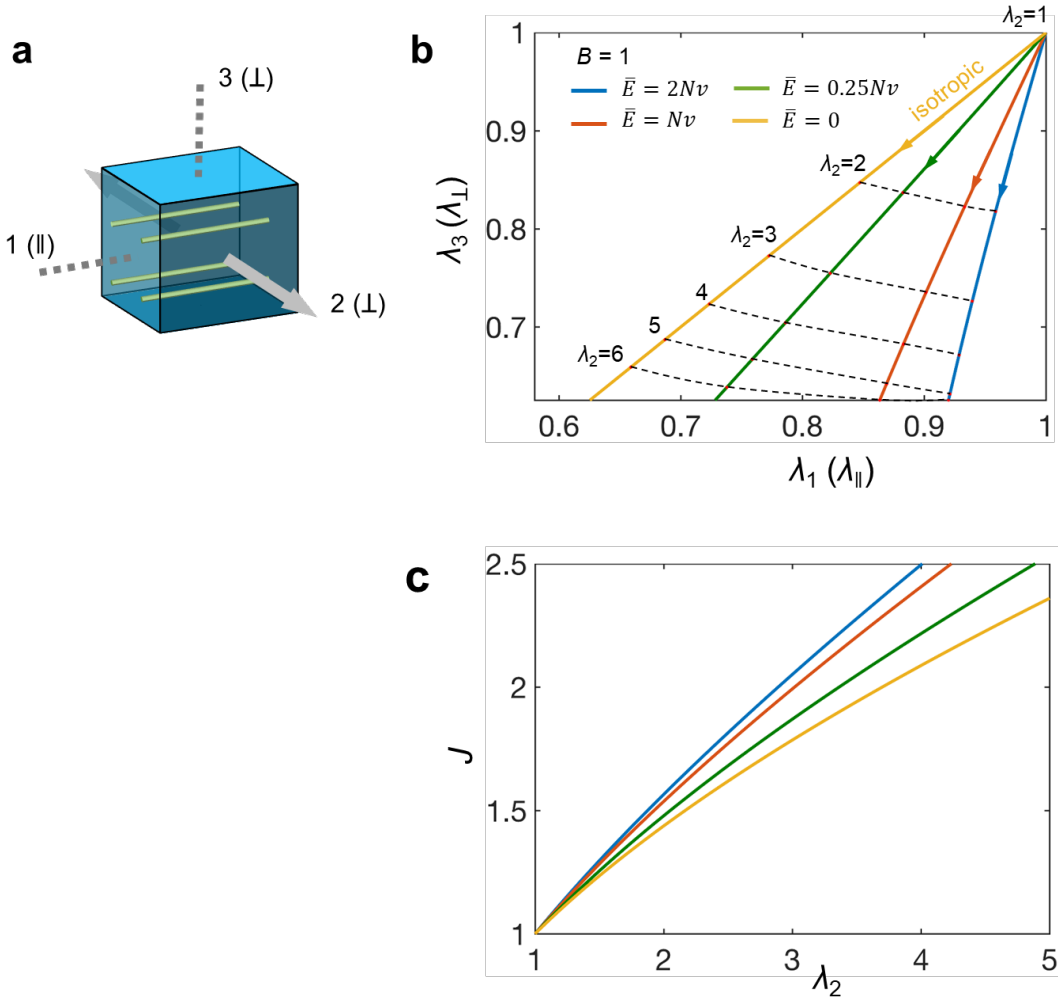

Figure 5.11 Anisotropic contraction of the cross-section perpendicular to the loading direction. (a) Schematic of uniaxial loading in the transverse direction 2. (b) Contraction in direction 1 (along the fiber) and in direction 3 (another transverse direction) for four cases: $\bar{E} = 2Nv$, $\bar{E} = Nv$, $\bar{E} = 0.25Nv$, and $\bar{E} = 0$ (isotropic hydrogel without microfibers). (c) Volume ratio as a function of applied stretch λ_2.

5.3.2 Anisotropic hydrogel with microfibers uniformly distributed in a plane

The configuration of the hydrogel with uniformly distributed microfibers in a plane are depicted schematically in Figure 5.12a. The fiber arrangement is confined within plane 1-

2. In this plane the FRG material property is isotropic and the probability of find a fiber at any orientation in-plane is $\rho = 1/2\pi$. For an arbitrary single fiber oriented to $\boldsymbol{N} = (\cos\theta, \sin\theta, 0)$ in the reference state, after the deformation the fiber length becomes $\lambda_f = [\lambda_1^2 \cos^2\theta + \lambda_2^2 \sin^2\theta]^{\frac{1}{2}}$. The equations of states take the form:

$$\frac{S_1}{k_B T/v} = \frac{Nv}{\Lambda_0^2}(\Lambda_0\lambda_1 - \Lambda_0^{-1}\lambda_1^{-1}) + \Lambda_0^{-3}\lambda_1^{-1}\left[J\log\left(1-\frac{1}{J}\right) + 1 + \frac{\chi}{J} - \frac{\mu}{kT}J\right] + \frac{\bar{E}}{2\pi B}\oint\left[e^{B(\lambda^f-1)} - 1\right]\lambda_1\cos^2\theta/\lambda^f\, d\theta \tag{5.21-1}$$

$$\frac{S_2}{k_B T/v} = \frac{Nv}{\Lambda_0^2}(\Lambda_0\lambda_2 - \Lambda_0^{-1}\lambda_2^{-1}) + \Lambda_0^{-3}\lambda_2^{-1}\left[J\log\left(1-\frac{1}{J}\right) + 1 + \frac{\chi}{J} - \frac{\mu}{kT}J\right] + \frac{\bar{E}}{2\pi B}\oint\left[e^{B(\lambda^f-1)} - 1\right]\lambda_2\sin^2\theta/\lambda^f\, d\theta \tag{5.21-2}$$

$$\frac{S_3}{k_B T/v} = \frac{Nv}{\Lambda_0^2}(\Lambda_0\lambda_3 - \Lambda_0^{-1}\lambda_3^{-1}) + \Lambda_0^{-3}\lambda_3^{-1}\left[J\log\left(1-\frac{1}{J}\right) + 1 + \frac{\chi}{J} - \frac{\mu}{kT}J\right] \tag{5.21-3}$$

The stress-free swelling and dehydration behavior of such a FRG can be again modeled using the stress-free conditions stated in Eq. (18).

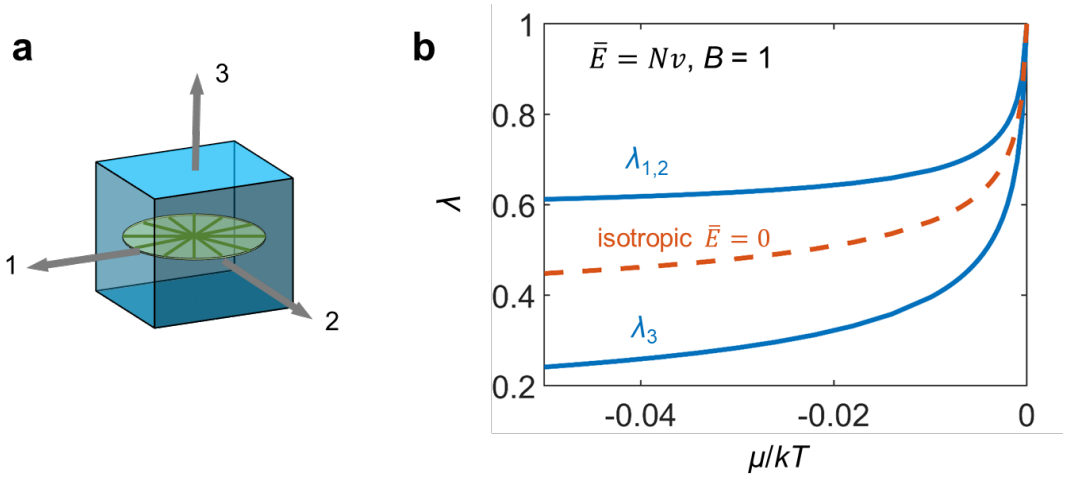

Figure 5.12 Anisotropic free-swelling of an anisotropic hydrogel with microfibers uniformly distributed in a plane. (a) Schematic of the anisotropic hydrogel with microfibers uniformly

distributed in a plane. (b) Anisotropic deformation due to stress-free dehydration with comparison to the isotropic hydrogel. The case is calculated with fiber property parameter $\bar{E} = Nv$, $B = 1$.

To demonstrate the anisotropic behavior of FRG with in-plane uniformly distributed microfibers, its swelling/dehydration deformation is solved at parameter combination $\bar{E} = Nv$, $B = 1$. With the chemical potential of the solvent μ/kT varying from 0~−0.05, the λ–μ curve splits from its isotropic counterpart, as shown in Figure 5.12b. Because microfibers distribute in 1-2 plane, the in-plane stiffness is reinforced. The FRG material experiences less contraction in plane 1-2 when compared to the transverse direction 3. The baseline case where $\bar{E} = 0$ is plotted in the orange dashed line. If $\bar{E}$ diminishes from Nv to zero, both the in-plane and out-of-plane contraction curves will merge to the baseline curve.

In Figure 5.13c~f, we plot the in-plane and out-of-plane uniaxial stress-stretch relations for four combinations of the microfiber properties. Because of the existence of the microfibers, the in-plane stress is higher than the out-of-plane stress at the same deformation. Moreover, the anisotropy becomes more pronounced for microfibers with higher tensile modulus, i.e., higher E and B. Again, in the direction where there is no fiber (the out-of-plane direction), the material mechanical properties are determined by the hydrogel phase itself. Therefore, even though the fibers stiffnesses are different in the four cases shown in Figure 5.13c~f, the stress-stretch curves are the same in the out-of-plane directions. A comparison between the Figure 5.10 and Figure 5.13 shows that the FRGs with planar distribution microfibers are more deformable than the FRGs with perfectly aligned fibers.

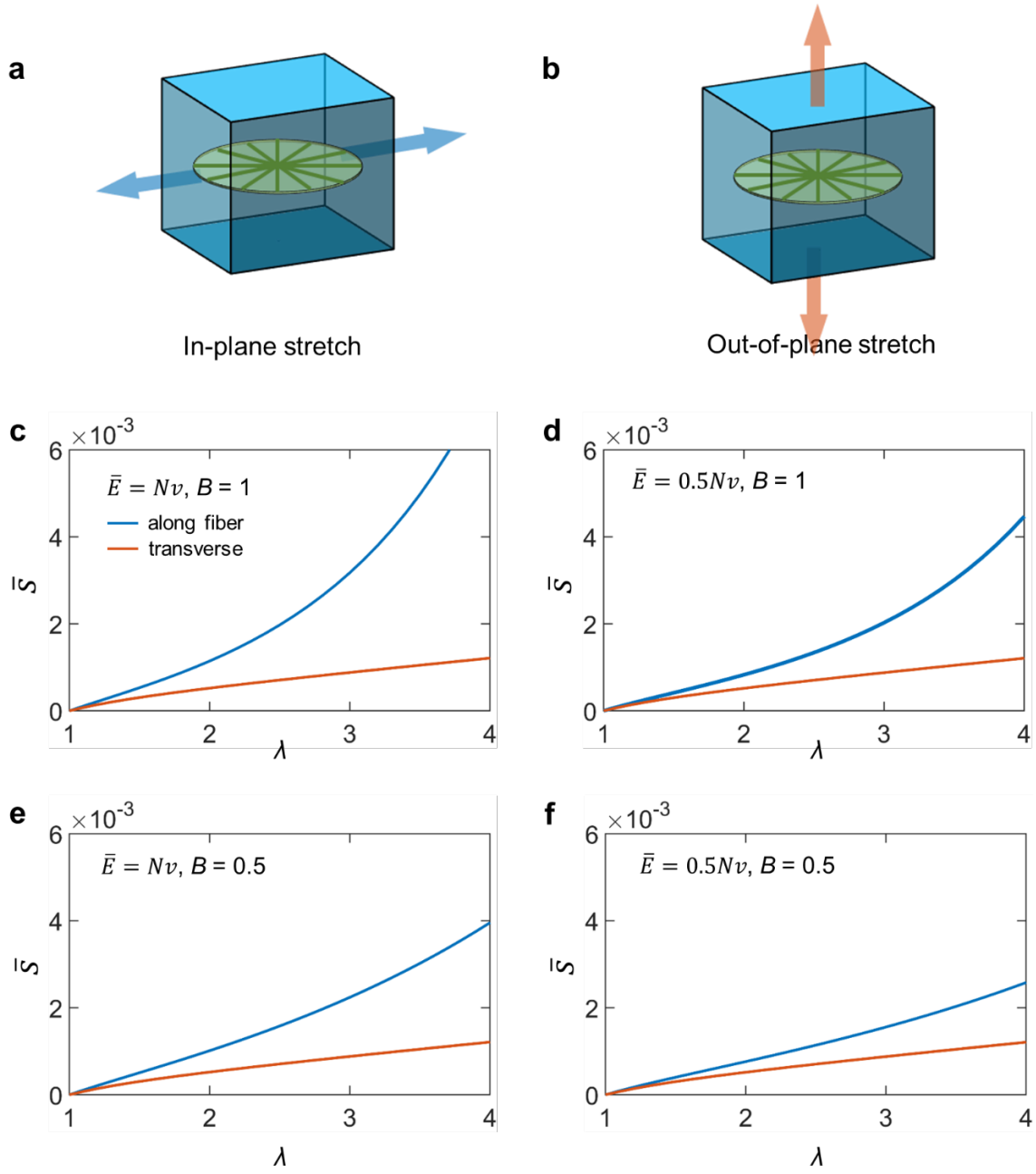

Figure 5.13 Uniaxial tensile behavior of anisotropic hydrogel with microfibers uniformly distributed in a plane. Schematic of uniaxial loading cases: (a) along the fiber distribution plane and (b) in the transverse direction. Relations between the dimensionless nominal stress and stretch along the fiber distribution plane and along the transverse direction for hydrogels with different fiber properties: (c) $\bar{E} = Nv$, $B = 1$, (d) $\bar{E} = 0.5Nv$, $B = 1$, (e) $\bar{E} = Nv$, $B = 0.5$, and (f) $\bar{E} = 0.5Nv$, $B = 0.5$.

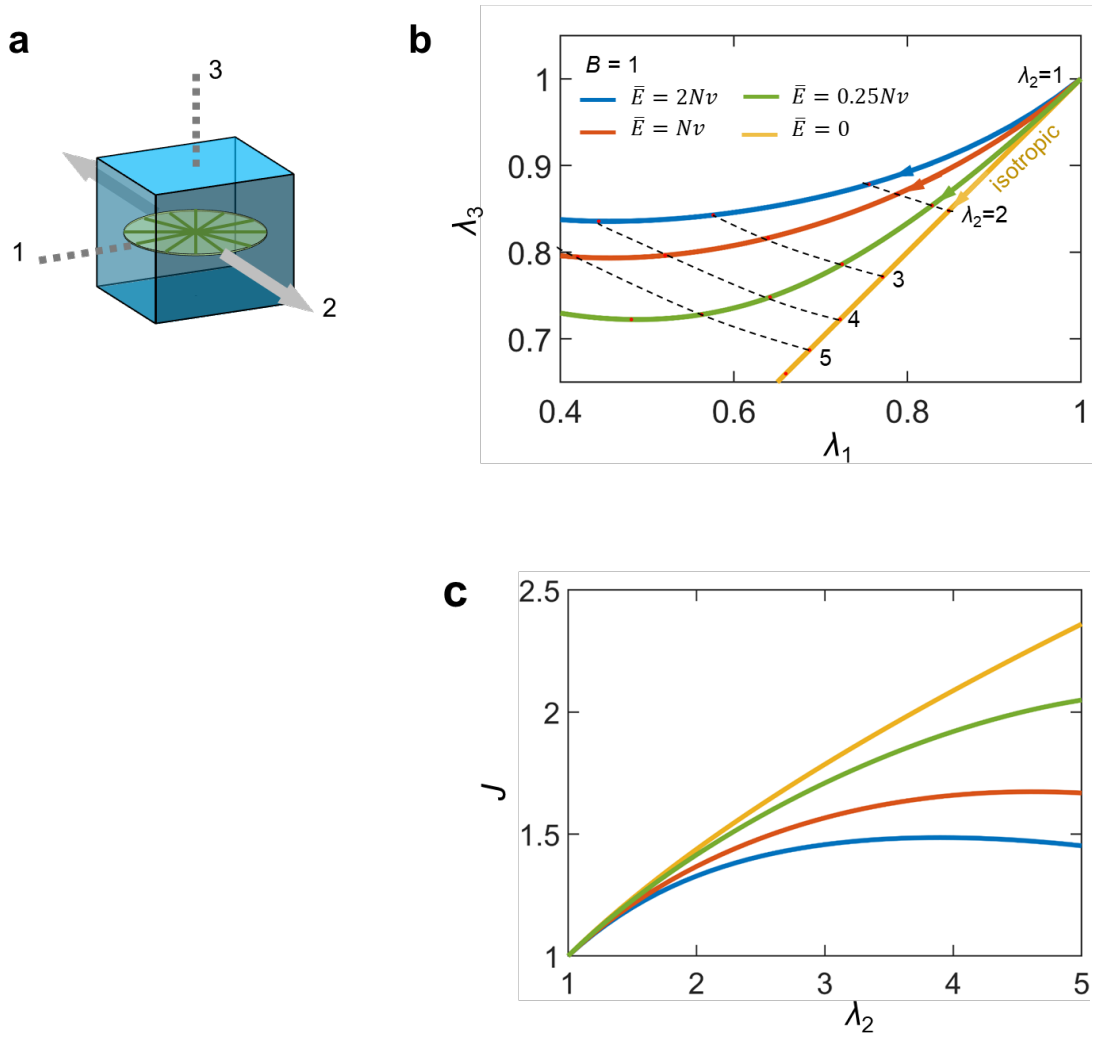

Figure 5.14 Anisotropic contraction of the cross-section perpendicular to the loading direction. (a) Schematic of uniaxial loading in the in-plane direction 2. (b) Contraction of the cross-section 3-1 for four cases: $\bar{E} = 2Nv$, $\bar{E} = Nv$, $\bar{E} = 0.25Nv$, $\bar{E} = 0.06Nv$, and $\bar{E} = 0$ (isotropic hydrogel without microfibers). (c) Volume ratio as a function of applied stretch λ_2.

When stretched in the in-plane direction 2, the perpendicular plane 3-1 is an anisotropic cross-section. In Figure 5.14b, the λ_3-λ_1 curves show the cross-section shape evolution as λ_2 increases from 1 to 5 (arrow direction). The baseline case of isotropic hydrogel (E=0) still extends along the 45° line. Even though direction 1 is parallel to the fiber distribution plane and is consequently reinforced, in this direction the FGR is rather more deformable

than in direction 3 under this specific loading condition. All λ_3-λ_1 curves for the worked-out cases are located above the isotropic line, indicating that the out-of-plane shrinkage is smaller than that in the in-plane direction. When uniaxially elongate a piece of hydrogel, there are two competing mechanisms. The axial stretch causes the transverse cross-section to contract due to Poisson's effect. However, the contraction is compensated by the further water absorption under the uniaxial loading condition. The existence of microfiber alters the competition of these two mechanisms and find a new balance between them. As in the case in section 3.1, the resistance of contraction contributed by the aligned microfibers is high, so that the material contracts more in the transverse direction. In comparison, when the microfibers are uniformly distributed in the 1-2 plane, the resistance against the contraction diminishes. As a result, the water absorption in the out-of-plane direction is the dominating factor against the contraction which in turn make the overall out-of-plane deformation less than direction 1. More intriguingly, the out-of-plane dimension of the cross-section does not deform monotonically as the FRG gets stretched in direction 1, it shrinks at the beginning but then starts to recover its original dimension. The volume ratio J is plotted in Figure 5.14c: It can be concluded from the J-λ_2 relations that the water absorption is bounded, in contrast to the case in section 3.1. In addition, the FRG reinforced with stiffer microfibers tends to absorb less water. This is another different behavior from the FRG with perfectly aligned fibers.

5.3.3 Anisotropic hydrogel with microfibers following in-plane von Mises distribution

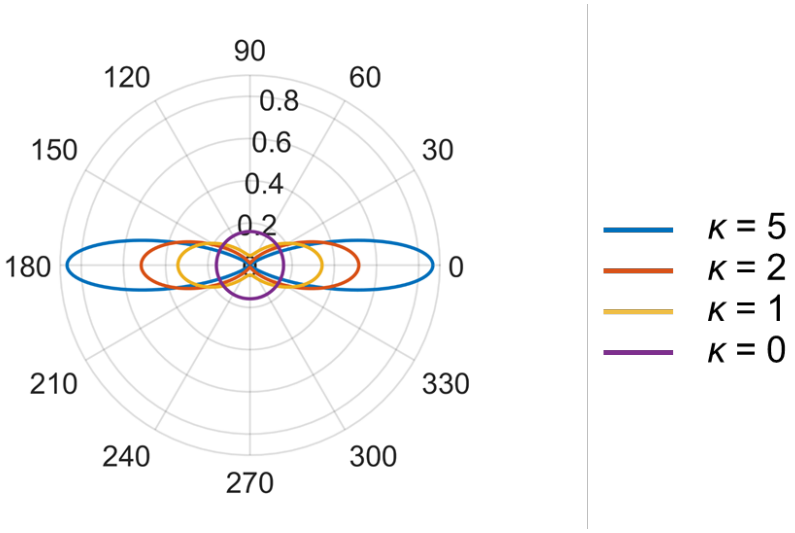

Figure 5.15 Von Mises-type directional distribution of microfibers with concentration parameter κ=5, 2, 1, and 0 (uniform distribution in plane). The fiber mean direction is oriented along 0°/180° line.

As a more general case, we next examine the FRG with microfibers following a planar von Mises-Fisher distribution. The von Mises-Fisher distribution is analogous to the Gaussian distribution wrapped over a unit circle, the probability distribution function f is

$$f(\theta|\theta_0,\kappa) = \frac{e^{\kappa\cos(\theta-\theta_0)}}{2\pi I_0(\kappa)} \tag{5.22}$$

where angle θ ranges from 0° to 360, θ_0 is the mean direction, κ is the concentration factor, and $I_0(\kappa)$ is the first-type hyperbolic Bessel function of order zero, $I_0(\kappa)$ is a constant at a given κ. Since a microfiber extends in both directions along its axis and is indistinguishable in either direction, the distribution of the microfibers has central symmetry. The von Mises-Fisher-type distribution of microfiber should take the form of $\rho_{\text{vms}} = 1/2\,[f(\theta|\theta_0,\kappa) + f(-\theta|-\theta_0,\kappa)]$, i.e.,

$$\rho_{\mathrm{vms}}(\theta|\theta_0,\kappa)=\frac{e^{\kappa\cos 2(\theta-\theta_0)}}{2\pi I_0(\kappa)} \tag{5.23}$$

Plotted in Figure 5.15 is the microfiber distribution at different concentration factors. When κ is higher the fibers are more concentrated and approaches the perfectly aligned case as in section 3.1. When κ is zero the distribution recovers the case of uniformly oriented microfibers discussed in section 3.2. The configuration of the hydrogel with von Mises-Fisher distribution at κ=2 is depicted schematically in Figure 5.16a. The fiber arrangement is confined in plane 1-2 and the mean distribution is along material coordinate direction 1. Similarly, inserting Eq. (23) into Eq. (13), we have the equations of states in the following form:

$$\begin{aligned}\frac{S_1}{k_{\mathrm{B}}T/v}=&\frac{Nv}{\Lambda_0^2}\left(\Lambda_0\lambda_1-\Lambda_0^{-1}\lambda_1^{-1}\right)+\Lambda_0^{-3}\lambda_1^{-1}\left[J\log\left(1-\frac{1}{J}\right)+1+\frac{\chi}{J}-\frac{\mu}{kT}J\right]\\&+\frac{\bar{E}}{2\pi I_0(\kappa)B}\oint\left[e^{B(\lambda^{\mathrm{f}}-1)}-1\right]e^{\kappa\cos 2\theta}\,\lambda_1\cos^2\theta/\lambda^{\mathrm{f}}\,d\theta\end{aligned} \tag{5.24-1}$$

$$\begin{aligned}\frac{S_2}{k_{\mathrm{B}}T/v}=&\frac{Nv}{\Lambda_0^2}\left(\Lambda_0\lambda_2-\Lambda_0^{-1}\lambda_2^{-1}\right)+\Lambda_0^{-3}\lambda_2^{-1}\left[J\log\left(1-\frac{1}{J}\right)+1+\frac{\chi}{J}-\frac{\mu}{kT}J\right]\\&+\frac{\bar{E}}{2\pi I_0(\kappa)B}\oint\left[e^{B(\lambda^{\mathrm{f}}-1)}-1\right]e^{\kappa\cos 2\theta}\,\lambda_2\sin^2\theta/\lambda^{\mathrm{f}}\,d\theta\end{aligned} \tag{5.24-2}$$

$$\frac{S_3}{k_{\mathrm{B}}T/v}=\frac{Nv}{\Lambda_0^2}\left(\Lambda_0\lambda_3-\Lambda_0^{-1}\lambda_3^{-1}\right)+\Lambda_0^{-3}\lambda_3^{-1}\left[J\log\left(1-\frac{1}{J}\right)+1+\frac{\chi}{J}-\frac{\mu}{kT}J\right] \tag{5.24-3}$$

The stress-free swelling and dehydration behavior of such a FRG can be solved by setting the stresses in Eq. (24) to zero. The free-swelling stretches are shown in Figure 5.16b with the comparison to the isotropic hydrogel. Since the FRG has all the three different material directions, the free-swelling curves splits into three unique curves. Lacking fiber reinforcement, the out-of-plane direction is the most deformable direction when the FRG

is subjected to chemical potential change. Furthermore, as the fibers prefers to orient in direction 1 rather than 2, the shrinkage in direction 1 is accordingly smaller.

The uniaxial tensile stretch along the microfiber distribution mean direction at finite κ is plotted in Figure 5.17b. As the figure shows, the stress-stretch curves are bounded by the perfectly aligned case where $\kappa=\infty$ and the in-plane uniform distribution case where $\kappa=0$. The more fibers orient along the loading direction, the stiffer the FRG becomes.

The cross-section shape evolution also exhibits a transitional behavior as the microfibers becomes more uniformly scattered from perfect aligned, as described in Figure 5.18b. As the preceding discussion has mentioned, if the fiber distribution is more concentrated, the stiffening effect in the fiber mean direction dominates so that the deformation is less than in the transverse directions. As the microfibers get more dispersed, the reinforcement is gradually overcome by the swelling-induced elongation of the out-of-plane dimension. As a result, as κ becomes smaller, the λ_3-λ_1 curve transits from the lower side of the isotropic contraction line to the above side.

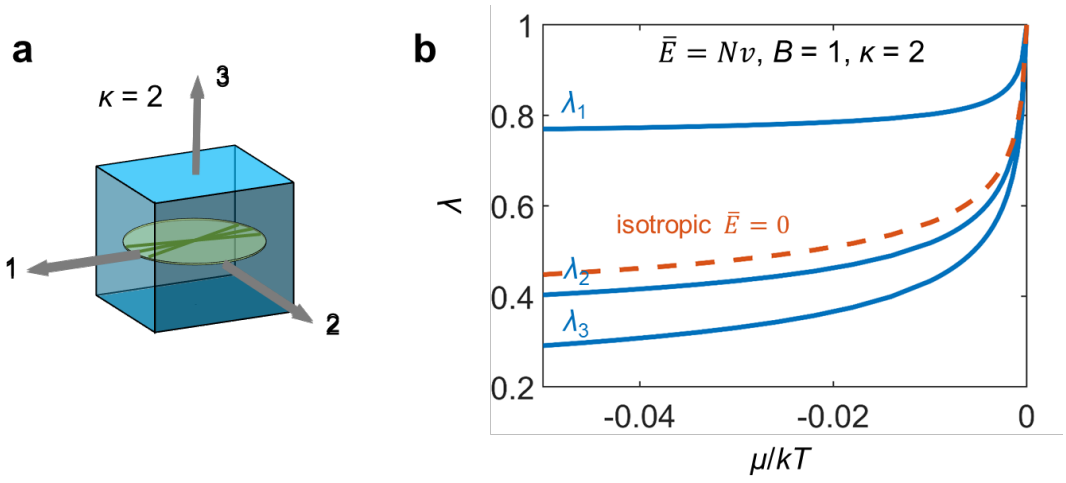

Figure 5.16 Anisotropic free-swelling of an anisotropic hydrogel with microfibers following in-plane von Mises distribution. (a) Schematic of the anisotropic hydrogel with microfibers following

in-plane von Mises distribution. (b) Anisotropic deformation due to stress-free dehydration with comparison to the isotropic hydrogel. The case is calculated with fiber property parameter $\bar{E} = Nv$, $B = 1$, and κ=2.

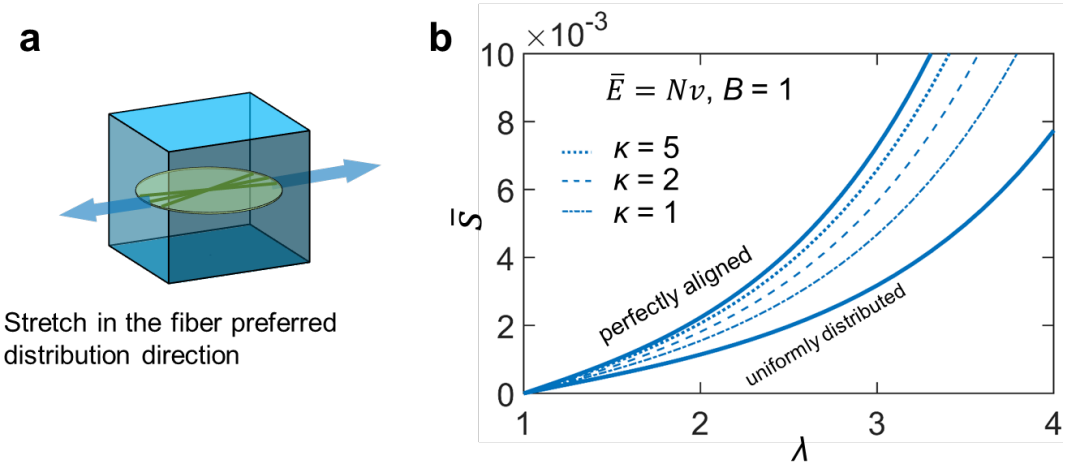

Figure 5.17 Uniaxial tensile behavior of anisotropic hydrogel with microfibers following in-plane von Mises distribution. Schematic of uniaxial loading (a) along the fiber preferred distribution. (b) Relations between the dimensionless nominal stress and stretch with different fiber distribution parameters: κ=1, 2, and 5. Comparison with the perfectly aligned and uniformly distributed cases.

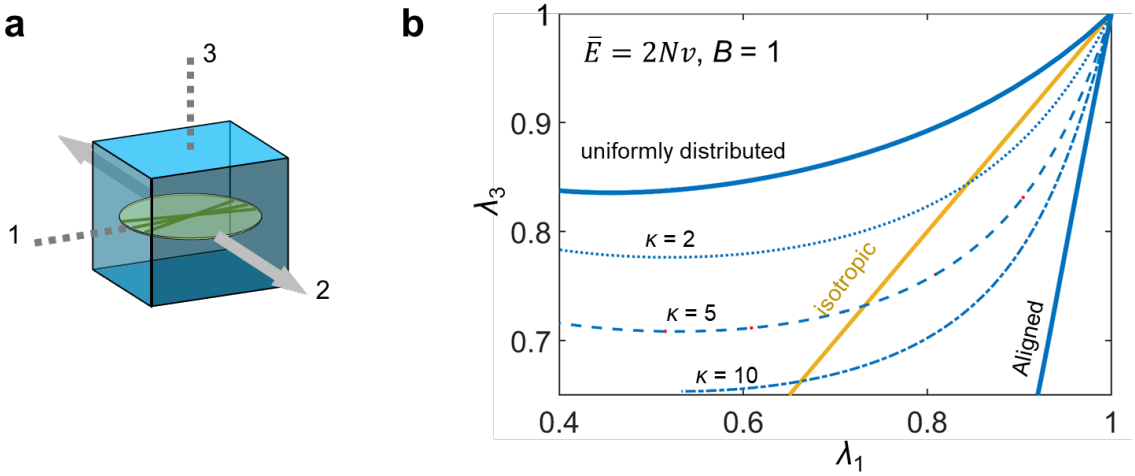

Figure 5.18 Anisotropic contraction of the cross-section perpendicular to the loading direction. (a) Schematic of uniaxial loading in material direction 2 of a FRG with von-Mises-type distribution in 1-2 plane. (b) Contraction of the cross-section 3-1 for three different distributions: κ=2, 5, 10, with comparison to the perfectly aligned, uniformly distributed, and isotropic cases.

In this section, we have explored the basic aspects of FGR with various fiber configurations, including the anisotropic stress-free swelling/dehydration, as well as the uniaxial tension performances in different material directions. It has been demonstrated that the composition of microfibers into the hydrogel matrix promises an array of anisotropic mechanical behaviors in addition to its already rich multi-physics behaviors. The next section is dedicated to a discussion of the application of the proposed constitutive framework to model the mechanical performance of a cellulose-nanofiber-based soft actuator.

5.4 Soft actuator driven by the drying of a cellulose nanofiber film on a polyimide substrate

5.4.1 Cellulose nanofibers (CNF) and the CNF/PI bilayer actuator

Among the myriad potentials and applications of anisotropic soft materials, soft actuators capitalizing the anisotropy to achieve optimized actuation performances have attracted tremendous attentions. Recently, we have developed a bilayer soft actuator based on the drying of a cellulose nanofiber (CNF) film with selectively aligned cellulose fibers.

When a fiber reinforced hydrogel thin film formed by the CNF/water network is deposited on a polyimide (PI) substrate, this bilayer structure becomes a humidity responsive actuator, as shown in Figure 5.19a and b. Since the CNF hydrogel is prepared in an aqueous solution where the relative humidity (*RH*) is 100%, if exposed in room condition where the relative humidity is less than 100%, the water molecules inside the CNF hydrogel will flow downhill energetically to the ambience (recall the chemical potential of water is related to

RH through $\mu = k_B T \log RH$). The drying of the CNF top layer is accompanied by a significant amount of volume shrinkage, enabling the actuation of the bilayer to scroll up into a ring. Depending on the fabrication process, the CNF/PI actuator can be made either with aligned CNFs oriented along the width of the film or randomly distributed CNFs in all in-plane directions. It is indicated in Figure 5.19b that the soft actuator with aligned CNF possesses an enhanced actuation performance.

5.4.2 Model and the results

The bilayer bending problem driven by differential deformation is a classic topic of solid mechanics. An analytical solution was provided by Timoshenko to the CTE-mismatch-induced bilayer bending made of linear elastic materials [165]. Although it is a common practice to represent (and misrepresent) the hygro-mechanical swelling process using a thermo-mechanical expansion analogy, this specific problem of CNF drying on a PI substrate is not one of the perfectly suitable cases for Timoshenko's approach. Firstly, thermo-mechanical analysis requires a reference temperature to begin with. It remains an open question how to estimate the initial dimensions of the CNF layer corresponding to such a reference temperature to set up the model. More importantly, in order to introduce the anisotropy and further investigate the actuation performance enhancement due to CNF alignment, different coefficients of thermal expansion (CTEs) have to be prescribed to different material directions. However, the proportion in which the total volumetric deformation is divided into each material direction cannot be prescribed in an *a priori* manner. It is even more problematic to assign a fixed value of this proportion at all strain levels.

The proposed constitutive model of fiber reinforced hydrogel overcomes these limitations. As discussed in section 2, the water concentration at the stress-free reference state of the as-synthesized CNF hydrogel can be determined by the material parameter Nv and χ. Furthermore, the present constitutive framework enables the capability of linking the material anisotropy directly to its microscopic structure, rather than a phenomenological prescription of CTE which does not provide any insight into the origin of the anisotropic CTE. The evaporation process is modeled by varying the chemical potential as a boundary condition, consequently, the water loss is solved as a field variable. Therefore, it is physically more rigorous to apply the FRG model to study the deformation mechanics of the CNF/PI soft actuator.

We first focus our attention to the situation where the thickness of the CNF layer is relatively thin compared to the thickness of the PI substrate. When this condition holds applicable, we immediately, have the following simplifications:

I. The material state variables (strain, stress, and water concentration etc.) are the same through the thickness direction;
II. The out-of-plane stress component (stress normal to the CNF surface) becomes negligible when compared to the in-plane components.
III. The mechanical interaction between the CNF and PI layer is the interfacial tangent stress, which can be lumped into an axial force P along the interface, as shown in Figure 5.19c.

For the CNF/PI bilayer actuator, the width is also substantially smaller than the longitudinal dimension in order to make sure that the bending deformation is preferred in the longitudinal direction. Thus, we have another simplification:

IV. The deformation in the width direction can be neglected, i.e., $\varepsilon_1=0$ or $\lambda_1=1$.

The moment resulting from translating the axial force P from the interface to the PI substrate neutral plane activates the bending of the entire bilayer structure. The moment is

$$M = Ph_s/2 \tag{5.25}$$

where h_s denotes the thickness of the PI substrate. Invoking the pure bending deformation of a Euler beam (Figure 5.19d), we have the bending radius

$$\frac{1}{R} = \frac{6P}{E_s h_s^2 b} \tag{5.26}$$

The deformation compatibility requires that at the interface length of the CNF film equals the length of the PI substrate, providing an additional equation for the CNF deformation:

$$\lambda_2 = -\frac{3P}{E_s h_s b} + 1 \tag{5.27}$$

The force balance of the CNF layer dictates that

$$P = s_2 b h_f \tag{5.28}$$

Combining Eqs. (26) ~ (28), we obtain

$$s_2 = \frac{1-\lambda_2}{\frac{3}{E_s}\frac{h_f}{h_s}} \tag{5.29}$$

Including the constitutive model of the FGR with perfectly aligned microfibers,

$$\frac{S_2}{k_B T/v} = \frac{Nv}{\Lambda_0^2}\left(\Lambda_0\lambda_2 - \Lambda_0^{-1}\lambda_2^{-1}\right) + \Lambda_0^{-3}\lambda_2^{-1}\left[J\log\left(1-\frac{1}{J}\right) + 1 + \frac{\chi}{J} - \frac{\mu}{kT}J\right] = \frac{1-\lambda_2}{\frac{k_B T}{v}\left(\frac{3}{E_s}\frac{h_f}{h_s}\right)} \tag{5.30-1}$$

$$\frac{S_3}{k_B T/v} = \frac{Nv}{\Lambda_0^2}\left(\Lambda_0\lambda_3 - \Lambda_0^{-1}\lambda_3^{-1}\right) + \Lambda_0^{-3}\lambda_3^{-1}\left[J\log\left(1-\frac{1}{J}\right) + 1 + \frac{\chi}{J} - \frac{\mu}{kT}J\right] = 0 \tag{5.30-2}$$

The above analysis introduces two extra parameters to the model, $E_s v/k_B T$ being the Young's modulus of the elastic PI substrate normalized by $k_B T/v$, and h_f/h_s being the thickness ratio between the CNF film and the substrate. Similarly, for the CNF film layer with randomly distributed fibers,

$$\frac{S_2}{k_B T/v} = \frac{Nv}{\Lambda_0^2}\left(\Lambda_0\lambda_2 - \Lambda_0^{-1}\lambda_2^{-1}\right) + \Lambda_0^{-3}\lambda_2^{-1}\left[J\log\left(1-\frac{1}{J}\right) + 1 + \frac{\chi}{J} - \frac{\mu}{kT}J\right] + \frac{\bar{E}}{2\pi B}\oint\left[e^{B(\lambda^f-1)} - 1\right]\lambda_2 \sin^2\theta/\lambda^f \, d\theta = \frac{1-\lambda_2}{\frac{k_B T}{v}\left(\frac{3}{E_s}\frac{h_f}{h_s}\right)} \tag{5.31-1}$$

$$\frac{S_3}{k_B T/v} = \frac{Nv}{\Lambda_0^2}\left(\Lambda_0\lambda_3 - \Lambda_0^{-1}\lambda_3^{-1}\right) + \Lambda_0^{-3}\lambda_3^{-1}\left[J\log\left(1-\frac{1}{J}\right) + 1 + \frac{\chi}{J} - \frac{\mu}{kT}J\right] = 0 \tag{5.31-2}$$

Solving Eqs. (30) and (31) for λ_2 and λ_3 at varying chemical potential μ, then the bending curvature is calculated using Eq. (26) and the volume ratio can be evaluated using $J=\lambda_1\lambda_2\lambda_3$ as a measurement of the water loss level. The actuation performance of the CNF/PI bilayer

is plotted in Figure 5.19e ~ h. A comparison between the aligned CNF actuator with its isotropic counterpart shows that the anisotropic CNF configuration enables a bending curvature 2 to 2.5 times higher at the same chemical potential or moisture loss level. Since the CNFs are aligned along the actuator width, the contraction in the longitudinal direction of the active CNF film is not confined. However, if the CNFs are randomly oriented in all possible in-plane directions, the contraction of the actuator causes energy penalty due to the compression of the microfibers. The water content loss will introduce more deformation in the out-of-plane normal direction to compensate the less contraction in the longitudinal direction. All the cases are solved at various geometry factor h_f/h_s, as expected, a thicker CNF film leads to a larger activated deformation. As the chemical potential decreases, the CNF hydrogel continues to lose water but the deformation approaches to a final shape as water content has been depleted. The final curvature is evaluated at $\mu/k_BT=-1$. The dependence of the bending curvature on h_f/h_s is also shown in Figure 5.20b, for both aligned CNF and randomly distributed CNF actuators.

Next, we can also calculate the lifting force by clamping the CNF/PI bilayer stripe in the axial direction. The lifting force is the reaction force induced over the two ends where the fixed boundary condition is applied. Figure 5.20a plots the lifting forces as a function of the volume ratio. It can be concluded that the anisotropic actuator has a lifting capacity approximately 1.5 times higher than the actuator with randomly distributed fibers.

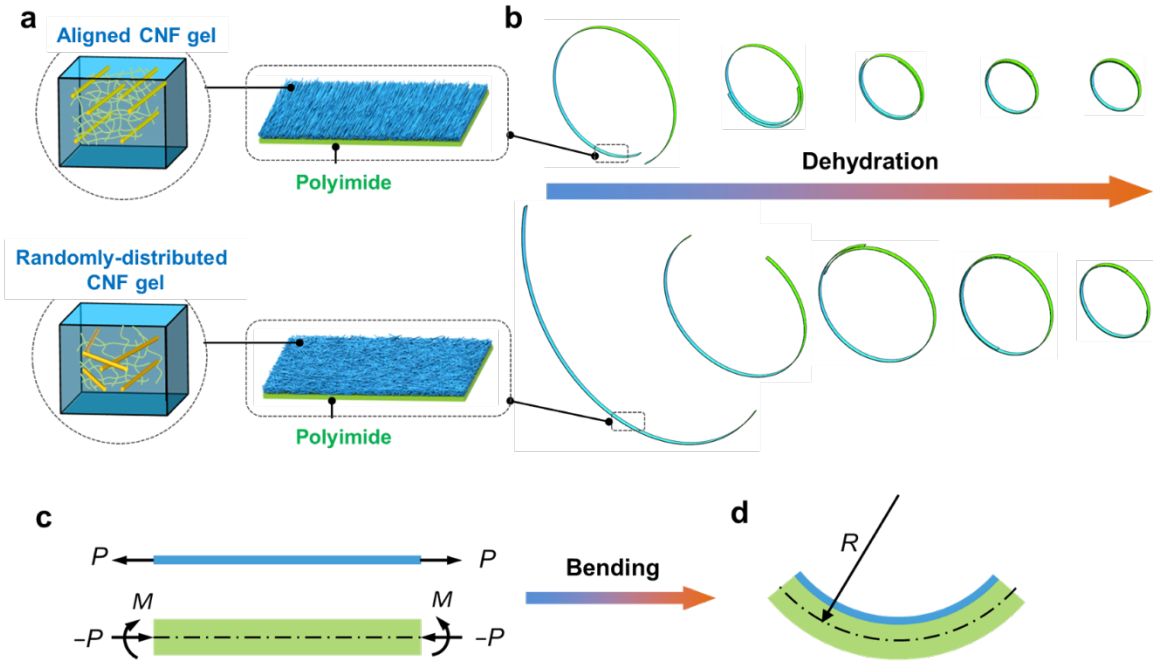
a
Aligned CNF gel
Polyimide
Randomly-distributed CNF gel
Polyimide
b
Dehydration
c
P
P
M
M
-P
-P
Bending
d
R

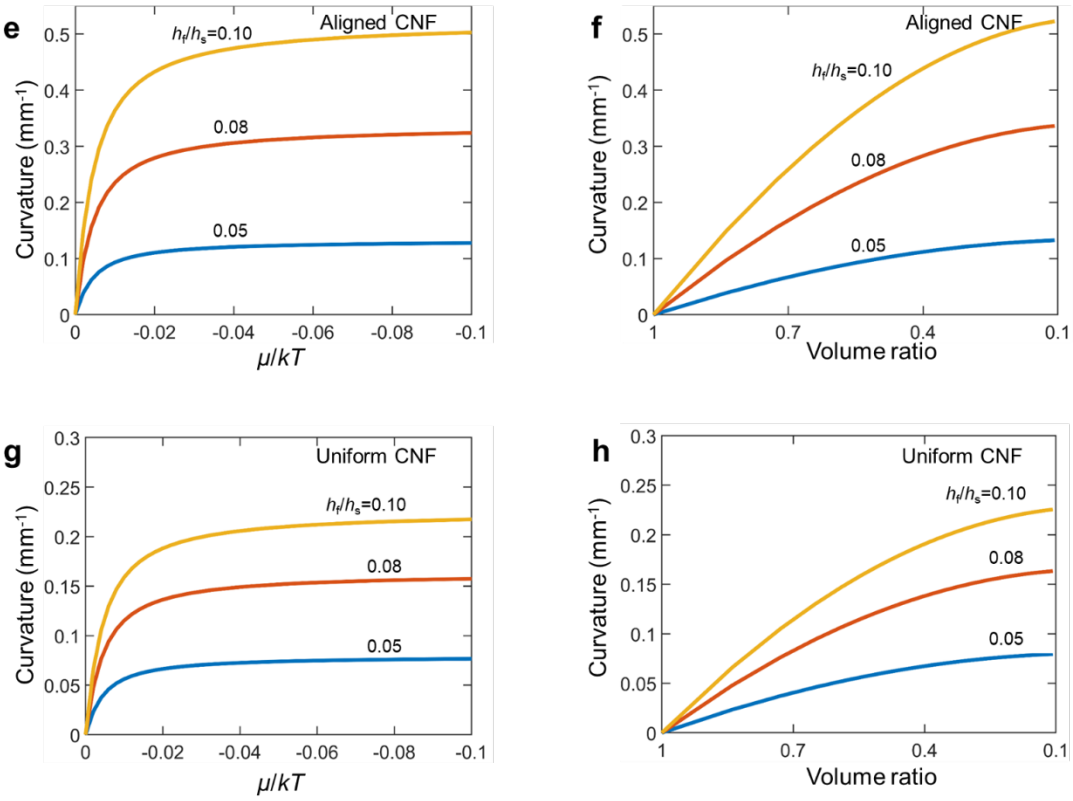
e
Aligned CNF
h_f/h_s=0.10
0.08
0.05
Curvature (mm^{-1})
μ/kT
f
Aligned CNF
h_f/h_s=0.10
0.08
0.05
Curvature (mm^{-1})
Volume ratio
g
Uniform CNF
h_f/h_s=0.10
0.08
0.05
Curvature (mm^{-1})
μ/kT
h
Uniform CNF
h_f/h_s=0.10
0.08
0.05
Curvature (mm^{-1})
Volume ratio

Figure 5.19 Analysis of a cellulose nanofiber (CNF) film drying on a polyimide (PI) substrate. (a) Schematic of aligned and isotropic CNF films. (b) An illustration of the deformation sequence of the CNF thin films drying on polyimide substrate at various water loss levels. (c) Free body diagram of the bilayer upon CNF film shrinkage. (d) Schematic of the bending of the bilayer. Deformation of the aligned CNF/PI bilayer: (e) Bending curvature as a function of chemical potential and (f) bending curvature as a function of volume ratio. Deformation of the isotropic CNG /PI bilayer at (g) various chemical potentials and (h) volume ratios.

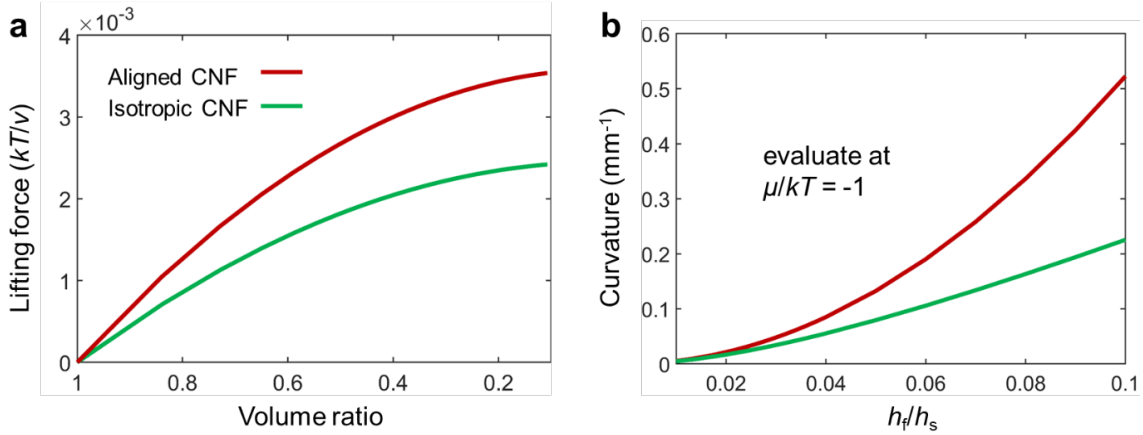

Figure 5.20 Lifting force and the final deformation of the CNF/PI actuator (a) Lifting force of the CNF/PI actuator as a function of volume ratios for aligned CNF active layer and isotropic CNF active layer. (b) Final bending curvature as a function of thickness ratio h_f/h_s evaluated at μ/k_BT=−1.

5.5 Summary of Chapter 5

From the perspective of micromechanics, we establish a physics-based constitutive suitable for microfiber reinforced anisotropic hydrogels. The hydrogel/fiber material system can be described by a thermodynamics free energy composed of three terms: the strain energy related to the polymer network deformation, the mixing energy due to the water association with hydrophilic polymer chains, in addition to the deformation energy stemming from the microfibers. On condition that the volume fraction of the microfiber phase is small, we further delineate a mapping between the deformation of the entire fiber reinforced hydrogel

and the deformation of its constituent phases. The hydrogel phase shares the same deformation of the entire composite material, while the one-dimensional microfibers experience length change. The proposed constitutive model provides a framework to account for microfiber directional distributions, enabling the capability to investigate hydrogels with different fiber configurations. The fiber reinforced hydrogel anisotropic behaviors are examined in terms of anisotropic swelling/dehydration, uniaxial tensile stress-strain relations, as well as the anisotropic cross-section contraction under uniaxial tensile loading.

Moreover, we demonstrate the FRG constitutive law is advantageous over the previous linear elastic model and more suitable for the anisotropic soft materials. we analyze the microstructure of chemically treated cellulose nanofibers, and the CNF hydrogel crosslinked via a percolating network of hydrogen bonds. The FRG constitutive model is applied to the CNF hydrogel to evaluate the actuation performance of CNF based bilayer actuators with aligned CNF film and uniformly distributed CNF active layer. We expect the propose model to provide insight into the deformation mechanics of fiber reinforced anisotropic hydrogels and promote the development of this novel type of anisotropic soft materials towards soft machines with functional applications.

Chapter 6: Conclusions and Outlook

6.1 Summary and Concluding Remarks

Under the topic of *Deformation Mechanics of soft Matter under External Stimuli*, this doctorate research is dedicated to push the boundary of the advanced topics in the mechanics of soft matters, specifically in attempts to:

I. Study the chemo-mechanical interaction of the solvent molecules and the polymeric network in a hydrogel and its impacts on the failure mechanics of a hydrogel thin-walled structure under internal inflation.

II. Apply the dielectric elastomer in soft sensor technology and propose a facile and powerful force sensor with in-situ tunable sensitivity,

III. Develop a novel light-responsive hydrogel material system with the application of bio-mimicking shape change and develop a corresponding deformation mechanics analytical framework to guide the material design.

IV. As well as enrich the theoretical scheme formulated by thermodynamics theory to model the behavior of a type of fiber-reinforce anisotropic hydrogel.

The contributions and importance of each chapter are summarized as follows.

6.1.1 Novelty and significance of Chapter 2: Deformation of a hydrogel balloon and the delayed burst of a hydrogel balloon subjected to inflation

The past decade has witnessed great research interests in hollow thin-shell structures of soft material. In applications such as soft actuator and soft robots, the shell is inflated by inner pressure to deliver swift deformation; when used as drug delivery systems, the shell is fractured by burst in a controllable fashion to release its encapsulated content. Even though the inflation and burst of an elastomeric thin shell has long been a canonical topic of solid mechanics, insights still remain elusive for the instabilities of its hydrogel-based counterparts whose burst behavior diverges from that of rubber thin shells.

In this chapter, we report for the first time the delayed burst phenomenon of a hydrogel balloon. That is, when a hydrogel balloon is subject to a subcritical pressure less than the instantaneous burst pressure, the hydrogel balloon remains stable for a span of time, and then burst suddenly. We refer to such a failure mode as delayed burst to highlight its delayed onset. Such a counterintuitive failure mode is more detrimental owing to its latent nature, and therefore, its understanding is of crucial importance in the mechanics of hydrogels as well as in the aforementioned applications. The study provides a systematic account of the delayed burst mechanism and indicates that the delayed burst hinges upon the physics of interaction between the solvent and the polymer network. The novelty and theoretical significance of the present study include:

I. Reveal the delayed burst of hydrogel thin-shell structures as a new failure mechanism, which is dissimilar from the instantaneous burst of a rubber shell: at a subcritical applied pressure the burst occurs with a delay in time. The delayed burst

failure mode is attributed to the unbounded swelling which accompanies the inflation process.

II. Predict the existence of three distinct inflation modes: equilibrium inflation, delayed burst, and instantaneous burst. Delineate a map of the three inflation modes of a thin-shell structure in the space of applied pressure and initial material stiffness by identifying the critical pressures for delayed and instantaneous burst.

III. Investigate the inflation of thick hydrogel balloons and find that the prominence of delayed burst diminishes as the wall thickness increases. Further predict that the delayed cavitation failure becomes irrelevant for a small void defect under inner pressurization.

The research findings have a significant impact in the theoretical understandings of the failure mechanics of hydrogel thin-shell structures and also in the development of soft actuators.

6.1.2 Novelty and significance of Chapter 3: Deformation of dielectric elastomer under through-thickness voltage and a DE-based force sensor

Enhanced and *in situ* tunable sensitivity is highly desirable for force sensors, but has been proved challenging. Existing force sensors depends heavily on ingenious but complex structural designs, imposing tremendous difficulty in fabrication and usually featuring a fixed sensitivity. To fill this gap, we propose for the first time a facile design of capacitive tactile force sensor with an enhanced and tunable sensitivity using electro-mechanically responsive dielectric elastomer (DE) as the sensing medium. Results from this chapter

indicates that, by leveraging the tunable mechanical behaviors of dielectric elastomer in response to a pre-stretch and a voltage, the effective sensitivity of the present dielectric elastomer force sensor can be continuously increased for over 40 times, which is otherwise prohibitively challenging. The novelty and significance of the present study include:

I. Present a facile design of capacitive tactile force sensor using a dielectric elastomer subjected to a modest voltage and a pre-stretch.

II. Demonstrate that the effective sensitivity of the abovementioned force sensor is enhanced by more than one order of magnitude compared to conventional polymer-based force sensor, and is *in situ* tunable by simply varying the applied voltage.

III. Define the safety working range of the dielectric elastomer force sensor by investigating the hazardous electrical breakdown complicated by the electromechanical instability of dielectric elastomers.

The research findings described in this chapter have a significant impact in the development of soft robot skins and open a broad avenue of using advanced materials in novel tactile sensor designs. It is believed that the significance and content of this chapter should be of wide interest in the community of theoretical solid mechanics as well as experimental solid mechanics.

6.1.3 Novelty and significance of Chapter 4: Deformation of light-responsive hydrogel

Existing soft matter based shape transform strategy are limited by patterning the desired deformed shape at design and fabrication stage, which is remove from Nature's living

organism shape transform. Inspired by the Nature's rich morphological transform strategies of living organisms, we propose a novel hydrogel material system composed of thermos-sensitive PNIPAM hydrogel and photo-thermal AgNPs. The hybrid hydrogel is featured by (1) light-responsive deformation (2) reprogrammable deformation (3) fast morphology transformation.

We developed for a theoretical framework to simulate the light-responsive deformation of the proposed hybrid hydrogel system. The analytical capability is a coupled thermos-mechanical model and is implemented in finite element analysis package ABAQUS. This is the first time that the thermodynamic of the deformation mechanics of temperature sensitive hydrogel is applied to a coupled thermos-mechanical analysis and is used for providing guidance to develop a novel hybrid hydrogel. Our research shed light on the mechanism of the shape transform of the PNIPAM/AgNPs hydrogel. We have found that:

I. The photo-thermal effect of the AgNPs induced an asymmetric temperature field inside the hydrogel body in both in-plane directions and through thickness directions

II. The temperature gradient established through the photo-thermal effects further causes differential swelling behavior of the temperature-sensitive PNIPAM hydrogel, which in turn activate the shape transform of the hydrogel sheet.

III. The temperature gradient relies on a delicate balance between the laser power input into the hybrid hydrogel and the heat dissipation through convection. Therefore, convection has a bearing on the activated deformation. In case of destruction of the thermal gradient caused by finite convection, the activated deformation diminishes.

The research findings described in this chapter have a significant impact in the development of soft-matter-based biomimicking shape transform strategies, as well as the development of mechanics theories on multi-physics deformation behavior of advanced functional hydrogels.

6.1.4 Novelty and significance of Chapter 5: Deformation of fiber-reinforced anisotropic hydrogel

The most recent years has witness a surging growth in research interests in anisotropic hydrogel, in an attempt to mimic Nature soft materials anisotropic behavior and further the applications of hydrogel. Despite its promising outlook in many aspects, there is still a profound lack of well formulated mechanical models to properly capture and to quantify the deformational behavior of anisotropic hydrogels. Existing constitutive models on fiber-reinforced hydrogels are either phenomenological in which the origin and physics of the fiber reinforcement effect is elusive or fallaciously based on the traditional composite material theories where the large deformation and mass transport of water are not accounted for. Either approach lacks a proper treatment addressing the coupled chemo-mechanical swelling of the material and a sufficient insight in the microscopic pictures of the fiber. Motivated by this delinquency in the theoretical efforts, we have established a physics-based constitutive model suitable for microfiber-reinforced anisotropic hydrogels. The novelties of this chapter are:

I. From the perspective of micromechanics, large deformation, mass transportation, and the origin of anisotropy are intrinsically relevant in the proposed model.

II. A fiber directional distribution can be naturally included in the proposed constitutive framework, which makes possible the investigation of various fiber reinforcement configurations.

III. Using this model, we explore several important anisotropic mechanical behaviors of the hydrogel, including the anisotropic swelling, and anisotropic stress-strain relation in uniaxial tensile loading.

IV. Moreover, we have successfully applied the present model to a type of cellulose-nanofiber-based wood hydrogels, and have analyzed the performance of a CNF/Polyimide bilayer humidity-active actuator.

We believe the research findings and the proposed constitutive model in this chapter to be impactful in the development of anisotropic hydrogels, both experimentally and theoretically.

6.2 Future work

Standing at this point and looking around the landscape of the current research efforts within the regime deformation mechanics of soft matters, the author has identified and suggested the following research proposals which can be made as extensions of the scope of this dissertation.

I. Developing and synthesizing hydrogels with superb mechanical properties, for example: tough hydrogels which are based on double-network microscopic topology; hydrogel with high fatigue life and fatigue limits. Developing the

corresponding solid mechanics framework to help unveil the mechanisms of the bestowed extreme mechanical performance.

II. Extending the current failure mechanics theory into the realm of soft material systems. Among fatigue, fracture, cavitation, damage, plasticity, visco-plasticity and Mullins effect, some of the failure mechanics are established upon conventional metallic materials, and the others are related to soft materials. The extension should be based on extensive experiment evidences or molecular simulation to shed light on the underlying physics of these phenomena.

III. Extending the current thermodynamics-based deformation mechanics theory of hydrogel to physically cross-linked hydrogels, such as those formed by hydroxyl bonds, in order to account for the dissipative energy lost into bond reorganization.

IV. Combining molecular dynamics simulation into the current continuum mechanics framework to establish a multi-scale mechanics model, in order to include multi-physics behaviors of the soft matter.

Reference

[1] W. Richtering and B. R. Saunders, “Gel architectures and their complexity,” *Soft Matter*, vol. 10, no. 21, pp. 3695–3702, May 2014.

[2] Y. Zhang, J. Wu, H. Wang, J. C. Meredith, and S. H. Behrens, “Stabilization of Liquid Foams through the Synergistic Action of Particles and an Immiscible Liquid,” *Angew. Chemie*, vol. 126, no. 49, pp. 13603–13607, Dec. 2014.

[3] S. Lam, E. Blanco, S. K. Smoukov, K. P. Velikov, and O. D. Velev, “Magnetically Responsive Pickering Foams,” *J. Am. Chem. Soc.*, vol. 133, no. 35, pp. 13856–13859, Sep. 2011.

[4] O. A. Araromi, I. Gavrilovich, J. Shintake, S. Rosset, M. Richard, V. Gass, and H. R. Shea, “Rollable Multisegment Dielectric Elastomer Minimum Energy Structures for a Deployable Microsatellite Gripper,” *IEEE/ASME Trans. Mechatronics*, vol. 20, no. 1, pp. 438–446, Feb. 2015.

[5] G. Kovacs, L. Düring, S. Michel, and G. Terrasi, “Stacked dielectric elastomer actuator for tensile force transmission,” *Sensors Actuators A Phys.*, vol. 155, no. 2, pp. 299–307, Oct. 2009.

[6] G. Kofod, “The static actuation of dielectric elastomer actuators: how does pre-stretch improve actuation?,” *J. Phys. D. Appl. Phys.*, vol. 41, no. 21, p. 215405, Nov. 2008.

[7] M. D. Konieczynska, J. C. Villa-Camacho, C. Ghobril, M. Perez-Viloria, K. M. Tevis, W. A. Blessing, A. Nazarian, E. K. Rodriguez, and M. W. Grinstaff, “On-Demand Dissolution of a Dendritic Hydrogel-based Dressing for Second-Degree Burn Wounds through Thiol-Thioester Exchange Reaction,” *Angew. Chemie Int. Ed.*, vol. 55, no. 34, pp. 9984–9987, Aug. 2016.

[8] J.-Y. Sun, X. Zhao, W. R. K. Illeperuma, O. Chaudhuri, K. H. Oh, D. J. Mooney, J. J. Vlassak, and Z. Suo, “Highly stretchable and tough hydrogels,” *Nature*, vol. 489, no. 7414, pp. 133–136, Sep. 2012.

[9] Y. Shin, S. Han, J. S. Jeon, K. Yamamoto, I. K. Zervantonakis, R. Sudo, R. D. Kamm, and S. Chung, “Microfluidic assay for simultaneous culture of multiple cell types on surfaces or within hydrogels,” *Nat. Protoc.*, vol. 7, no. 7, pp. 1247–1259, Jun. 2012.

[10] H. Geckil, F. Xu, X. Zhang, S. Moon, and U. Demirci, “Engineering hydrogels as extracellular matrix mimics,” *Nanomedicine*, vol. 5, no. 3, pp. 469–484, Apr. 2010.

[11] A. P. Wong, R. Perez-Castillejos, J. Christopher Love, and G. M. Whitesides,

"Partitioning microfluidic channels with hydrogel to construct tunable 3-D cellular microenvironments," *Biomaterials*, vol. 29, no. 12, pp. 1853–1861, Apr. 2008.

[12] Y. Ling, J. Rubin, Y. Deng, C. Huang, U. Demirci, J. M. Karp, and A. Khademhosseini, "A cell-laden microfluidic hydrogel," *Lab Chip*, vol. 7, no. 6, p. 756, May 2007.

[13] S.-Y. Cheng, S. Heilman, M. Wasserman, S. Archer, M. L. Shuler, and M. Wu, "A hydrogel-based microfluidic device for the studies of directed cell migration," *Lab Chip*, vol. 7, no. 6, p. 763, May 2007.

[14] J. L. Drury and D. J. Mooney, "Hydrogels for tissue engineering: scaffold design variables and applications," *Biomaterials*, vol. 24, no. 24, pp. 4337–4351, Nov. 2003.

[15] J. Li and D. J. Mooney, "Designing hydrogels for controlled drug delivery," *Nat. Rev. Mater.*, vol. 1, no. 12, 2016.

[16] A. Sydney Gladman, E. A. Matsumoto, R. G. Nuzzo, L. Mahadevan, and J. A. Lewis, "Biomimetic 4D printing," *Nat. Mater.*, vol. 15, no. 4, pp. 413–418, Apr. 2016.

[17] Z. L. Wu, M. Moshe, J. Greener, H. Therien-Aubin, Z. Nie, E. Sharon, and E. Kumacheva, "Three-dimensional shape transformations of hydrogel sheets induced by small-scale modulation of internal stresses," *Nat. Commun.*, vol. 4, p. 1586, 2013.

[18] P. J. Flory and J. Rehner, "Statistical Mechanics of Cross-Linked Polymer Networks I. Rubberlike Elasticity," *J. Chem. Phys.*, vol. 11, no. 11, pp. 512–520, Nov. 1943.

[19] C. J. Durning and K. N. Morman, "Nonlinear swelling of polymer gels," *J. Chem. Phys.*, vol. 98, no. 5, pp. 4275–4293, Mar. 1993.

[20] K. Sekimoto, "Thermodynamics and hydrodynamics of chemical gels," *J. Phys. II*, vol. 1, no. 1, pp. 19–36, Jan. 1991.

[21] L. R. G. Treloar, "physics of rubber elasticity." Clarendon Press, 1949.

[22] X. Zhao, W. Hong, and Z. Suo, "Inhomogeneous and anisotropic equilibrium state of a swollen hydrogel containing a hard core," *Appl. Phys. Lett.*, vol. 92, no. 5, p. 051904, Feb. 2008.

[23] W. Hong, Z. Liu, and Z. Suo, "Inhomogeneous swelling of a gel in equilibrium with a solvent and mechanical load," *Int. J. Solids Struct.*, vol. 46, no. 17, pp. 3282–3289, Aug. 2009.

[24] S. Cai and Z. Suo, "Mechanics and chemical thermodynamics of phase transition in temperature-sensitive hydrogels," *J. Mech. Phys. Solids*, vol. 59, no. 11, pp. 2259–2278, Nov. 2011.

[25] Z. Ding, Z. Liu, J. Hu, S. Swaddiwudhipong, and Z. Yang, "Inhomogeneous large

deformation study of temperature-sensitive hydrogel," *Int. J. Solids Struct.*, vol. 50, no. 16–17, pp. 2610–2619, Aug. 2013.

[26] J. Li, Z. Suo, and J. J. Vlassak, "A model of ideal elastomeric gels for polyelectrolyte gels.," *Soft Matter*, vol. 10, no. 15, pp. 2582–90, 2014.

[27] R. Marcombe, S. Cai, W. Hong, X. Zhao, Y. Lapusta, and Z. Suo, "A theory of constrained swelling of a pH-sensitive hydrogel," *Soft Matter*, vol. 6, no. 4, p. 784, Feb. 2010.

[28] Z. Suo, "Theory of dielectric elastomers," *Acta Mech. Solida Sin.*, vol. 23, no. 6, pp. 549–578, 2010.

[29] X. Zhao and Z. Suo, "Electrostriction in elastic dielectrics undergoing large deformation," *J. Appl. Phys.*, vol. 104, no. 12, pp. 1–7, 2008.

[30] Y. S. Kim, M. Liu, Y. Ishida, Y. Ebina, M. Osada, T. Sasaki, T. Hikima, M. Takata, and T. Aida, "Thermoresponsive actuation enabled by permittivity switching in an electrostatically anisotropic hydrogel," *Nat. Mater.*, vol. 14, no. 10, pp. 1002–1007, Oct. 2015.

[31] Y. Yao, M. T. McDowell, I. Ryu, H. Wu, N. Liu, L. Hu, W. D. Nix, and Y. Cui, "Interconnected silicon hollow nanospheres for lithium-ion battery anodes with long cycle life," *Nano Lett.*, vol. 11, no. 7, pp. 2949–2954, Jul. 2011.

[32] L. A. Godoy, "Buckling of vertical oil storage steel tanks: Review of static buckling studies," *Thin-Walled Struct.*, vol. 103, pp. 1–21, Jun. 2016.

[33] A. Nemiroski, Y. Y. Shevchenko, A. A. Stokes, B. Unal, A. Ainla, S. Albert, G. Compton, E. MacDonald, Y. Schwab, C. Zellhofer, and G. M. Whitesides, "Arthrobots," *Soft Robot.*, p. soro.2016.0043, May 2017.

[34] A. Ainla, M. S. Verma, D. Yang, and G. M. Whitesides, "Soft, rotating pneumatic actuator," *Soft Robot.*, vol. 4, no. 3, pp. 297–304, May 2017.

[35] R. F. Shepherd, F. Ilievski, W. Choi, S. A. Morin, A. A. Stokes, A. D. Mazzeo, X. Chen, M. Wang, and G. M. Whitesides, "Multigait soft robot," *Proc. Natl. Acad. Sci. U. S. A.*, vol. 108, no. 51, pp. 20400–3, Dec. 2011.

[36] N. W. Bartlett, M. T. Tolley, J. T. B. Overvelde, J. C. Weaver, B. Mosadegh, K. Bertoldi, G. M. Whitesides, and R. J. Wood, "A 3D-printed, functionally graded soft robot powered by combustion.," *Science*, vol. 349, no. 6244, pp. 161–5, Jul. 2015.

[37] H. Yuk, S. Lin, C. Ma, M. Takaffoli, N. X. Fang, and X. Zhao, "Hydraulic hydrogel actuators and robots optically and sonically camouflaged in water," *Nat. Commun.*, vol. 8,

p. 14230, Feb. 2017.

[38] A. D. Marchese, C. D. Onal, and D. Rus, “Autonomous soft robotic fish capable of escape maneuvers using fluidic elastomer actuators,” *Soft Robot.*, vol. 1, no. 1, pp. 75–87, Mar. 2014.

[39] E. Acome, S. K. Mitchell, T. G. Morrissey, M. B. Emmett, C. Benjamin, M. King, M. Radakovitz, and C. Keplinger, “Hydraulically amplified self-healing electrostatic actuators with muscle-like performance.,” *Science*, vol. 359, no. 6371, pp. 61–65, Jan. 2018.

[40] M. Wehner, R. L. Truby, D. J. Fitzgerald, B. Mosadegh, G. M. Whitesides, J. A. Lewis, and R. J. Wood, “An integrated design and fabrication strategy for entirely soft, autonomous robots,” *Nature*, vol. 536, no. 7617, pp. 451–455, Aug. 2016.

[41] D.-H. Kim, N. Lu, R. Ghaffari, Y.-S. Kim, S. P. Lee, L. Xu, J. Wu, R.-H. Kim, J. Song, Z. Liu, J. Viventi, B. de Graff, B. Elolampi, M. Mansour, M. J. Slepian, S. Hwang, J. D. Moss, S.-M. Won, Y. Huang, B. Litt, and J. A. Rogers, “Materials for multifunctional balloon catheters with capabilities in cardiac electrophysiological mapping and ablation therapy,” *Nat. Mater.*, vol. 10, no. 4, pp. 316–323, Apr. 2011.

[42] S. Zhao, P. Agarwal, W. Rao, H. Huang, R. Zhang, Z. Liu, J. Yu, N. Weisleder, W. Zhang, and X. He, “Coaxial electrospray of liquid core–hydrogel shell microcapsules for encapsulation and miniaturized 3D culture of pluripotent stem cells,” *Integr. Biol.*, vol. 6, no. 9, pp. 874–884, Aug. 2014.

[43] W. Song, Y. Lu, A. S. Frankel, D. An, R. E. Schwartz, and M. Ma, “Engraftment of human induced pluripotent stem cell-derived hepatocytes in immunocompetent mice via 3D co-aggregation and encapsulation,” *Sci. Rep.*, vol. 5, no. 1, p. 16884, Dec. 2015.

[44] S. Mytnyk, I. Ziemecka, A. G. L. Olive, J. W. M. van der Meer, K. A. Totlani, S. Oldenhof, M. T. Kreutzer, V. van Steijn, and J. H. van Esch, “Microcapsules with a permeable hydrogel shell and an aqueous core continuously produced in a 3D microdevice by all-aqueous microfluidics,” *RSC Adv.*, vol. 7, no. 19, pp. 11331–11337, Feb. 2017.

[45] Y. Lu, W. Song, D. An, B. J. Kim, R. Schwartz, M. Wu, and M. Ma, “Designing compartmentalized hydrogel microparticles for cell encapsulation and scalable 3D cell culture,” *J. Mater. Chem. B*, vol. 3, no. 3, pp. 353–360, Dec. 2015.

[46] K. Alessandri, B. R. Sarangi, V. V. Gurchenkov, B. Sinha, T. R. Kießling, L. Fetler, F. Rico, S. Scheuring, C. Lamaze, A. Simon, S. Geraldo, D. Vignjevic, H. Doméjean, L. Rolland, A. Funfak, J. Bibette, N. Bremond, and P. Nassoy, “Cellular capsules as a tool for multicellular spheroid production and for investigating the mechanics of tumor

progression in vitro," *Proc. Natl. Acad. Sci. U. S. A.*, vol. 110, no. 37, pp. 14843–8, Sep. 2013.

[47] R. M. Olabisi, Z. W. Lazard, C. L. Franco, M. A. Hall, S. K. Kwon, E. M. Sevick-Muraca, J. A. Hipp, A. R. Davis, E. A. Olmsted-Davis, and J. L. West, "Hydrogel microsphere encapsulation of a cell-based gene therapy system increases cell survival of injected cells, transgene expression, and bone volume in a model of heterotopic ossification," *Tissue Eng. Part A*, vol. 16, no. 12, pp. 3727–3736, Dec. 2010.

[48] Y. Wang and J. Wang, "Mixed hydrogel bead-based tumor spheroid formation and anticancer drug testing," *Analyst*, vol. 139, no. 10, pp. 2449–2458, Apr. 2014.

[49] A. C. Lima, P. Batista, T. A. M. Valente, A. S. Silva, I. J. Correia, and J. F. Mano, "Novel methodology based on biomimetic superhydrophobic substrates to immobilize cells and proteins in hydrogel spheres for applications in bone regeneration," *Tissue Eng. Part A*, vol. 19, no. 9–10, pp. 1175–1187, May 2013.

[50] R. Luo, Y. Cao, P. Shi, and C.-H. Chen, "Near-infrared light responsive multi-compartmental hydrogel particles synthesized through droplets assembly induced by superhydrophobic surface," *Small*, vol. 10, no. 23, pp. 4886–4894, Dec. 2014.

[51] K. Yoshida and H. Onoe, "Functionalized core-shell hydrogel microsprings by anisotropic gelation with bevel-tip capillary," *Sci. Rep.*, vol. 7, p. 45987, Apr. 2017.

[52] J. Li and D. J. Mooney, "Designing hydrogels for controlled drug delivery," *Nature Reviews Materials*. 2016.

[53] D. R. Griffin, W. M. Weaver, P. O. Scumpia, D. Di Carlo, and T. Segura, "Accelerated wound healing by injectable microporous gel scaffolds assembled from annealed building blocks," *Nat. Mater.*, vol. 14, no. 7, pp. 737–744, Jul. 2015.

[54] J. Alijotas-Reig, M. T. Fernández-Figueras, and L. Puig, "Late-onset inflammatory adverse reactions related to soft tissue filler injections," *Clin. Rev. Allergy Immunol.*, vol. 45, no. 1, pp. 97–108, Aug. 2013.

[55] V. I. Feodos'ev, "On equilibrium modes of a rubber spherical shell under internal pressure," *J. Appl. Math. Mech.*, vol. 32, no. 2, pp. 339–344, Jan. 1968.

[56] H. Alexander, "Tensile instability of initially spherical balloons," *Int. J. Eng. Sci.*, vol. 9, no. 1, pp. 151–160, Jan. 1971.

[57] A. Needleman, "Inflation of spherical rubber balloons," *Int. J. Solids Struct.*, vol. 13, no. 5, pp. 409–421, Jan. 1977.

[58] D. R. Merritt and F. Weinhaus, "The pressure curve for a rubber balloon," *Am. J. Phys.*,

vol. 46, no. 10, pp. 976–977, Oct. 1978.

[59] D. K. Bogen and T. A. McMahon, “Do cardiac aneurysms blow out?,” *Biophys. J.*, vol. 27, no. 2, pp. 301–316, Aug. 1979.

[60] G. deBotton, R. Bustamante, and A. Dorfmann, “Axisymmetric bifurcations of thick spherical shells under inflation and compression,” *Int. J. Solids Struct.*, vol. 50, no. 2, pp. 403–413, Jan. 2013.

[61] Y. Chen and T. J. Healey, “Bifurcation to pear-shaped equilibria of pressurized spherical membranes,” *Int. J. Non. Linear. Mech.*, vol. 26, no. 3–4, pp. 279–291, Jan. 1991.

[62] J. T. B. Overvelde, T. Kloek, J. J. A. D’haen, and K. Bertoldi, “Amplifying the response of soft actuators by harnessing snap-through instabilities.,” *Proc. Natl. Acad. Sci. U. S. A.*, vol. 112, no. 35, pp. 10863–8, Sep. 2015.

[63] T. Li, C. Keplinger, R. Baumgartner, S. Bauer, W. Yang, and Z. Suo, “Giant voltage-induced deformation in dielectric elastomers near the verge of snap-through instability,” *J. Mech. Phys. Solids*, vol. 61, no. 2, pp. 611–628, Feb. 2013.

[64] F. Wang, C. Yuan, T. Lu, and T. J. Wang, “Anomalous bulging behaviors of a dielectric elastomer balloon under internal pressure and electric actuation,” *J. Mech. Phys. Solids*, vol. 102, pp. 1–16, May 2017.

[65] T. Lu, L. An, J. Li, C. Yuan, and T. J. Wang, “Electro-mechanical coupling bifurcation and bulging propagation in a cylindrical dielectric elastomer tube,” *J. Mech. Phys. Solids*, vol. 85, pp. 160–175, Dec. 2015.

[66] H. Wang and S. Cai, “Drying-induced cavitation in a constrained hydrogel,” *Soft Matter*, vol. 11, no. 6, pp. 1058–1061, Jan. 2015.

[67] V. Zamani and T. J. Pence, “Swelling, inflation, and a swelling-burst instability in hyperelastic spherical shells,” *Int. J. Solids Struct.*, vol. 125, pp. 134–149, Oct. 2017.

[68] X. Wang and W. Hong, “Delayed fracture in gels,” *Soft Matter*, vol. 8, no. 31, pp. 8171–8178, Jul. 2012.

[69] J. Tang, J. Li, J. J. Vlassak, and Z. Suo, “Fatigue fracture of hydrogels,” *Extrem. Mech. Lett.*, vol. 10, pp. 24–31, Jan. 2017.

[70] D. Bonn, H. Kellay, M. Prochnow, K. Ben-Djemiaa, and J. Meunier, “Delayed fracture of an inhomogeneous soft solid,” *Science*, vol. 280, no. 5361, pp. 265–7, Apr. 1998.

[71] Y. Mao and L. Anand, “A theory for fracture of polymeric gels,” *J. Mech. Phys. Solids*, vol. 115, pp. 30–53, Jun. 2018.

[72] P. J. Skrzeszewska, J. Sprakel, F. A. de Wolf, R. Fokkink, M. A. Cohen Stuart, and J. van

der Gucht, “Fracture and self-healing in a well-defined self-assembled polymer network,” *Macromolecules*, vol. 43, no. 7, pp. 3542–3548, Apr. 2010.

[73] M. K. Chaudhury, “Rate-dependent fracture at adhesive interface,” *J. Phys. Chem. B*, vol. 103, no. 31, pp. 6562–6566, 1999.

[74] S. B. Lindström, T. E. Kodger, J. Sprakel, and D. A. Weitz, “Structures, stresses, and fluctuations in the delayed failure of colloidal gels,” *Soft Matter*, vol. 8, no. 13, p. 3657, Mar. 2012.

[75] T. Baumberger, C. Caroli, and D. Martina, “Solvent control of crack dynamics in a reversible hydrogel,” *Nat. Mater.*, vol. 5, no. 7, pp. 552–555, Jul. 2006.

[76] J. Marthelot, F. López Jiménez, A. Lee, J. W. Hutchinson, and P. M. Reis, “Buckling of a pressurized hemispherical shell subjected to a probing force,” *J. Appl. Mech.*, vol. 84, no. 12, p. 121005, Oct. 2017.

[77] M. Curatolo, P. Nardinocchi, E. Puntel, and L. Teresi, “Transient instabilities in the swelling dynamics of a hydrogel sphere,” *J. Appl. Phys.*, vol. 122, no. 14, p. 145109, Oct. 2017.

[78] T. Bertrand, J. Peixinho, S. Mukhopadhyay, and C. W. MacMinn, “Dynamics of swelling and drying in a spherical gel,” *Phys. Rev. Appl.*, vol. 6, no. 6, p. 064010, Dec. 2016.

[79] A. Lee, F. López Jiménez, J. Marthelot, J. W. Hutchinson, and P. M. Reis, “The geometric role of precisely engineered imperfections on the critical buckling load of spherical elastic shells,” *J. Appl. Mech.*, vol. 83, no. 11, p. 111005, Sep. 2016.

[80] H. Wang and S. Cai, “Cavitation in a swollen elastomer constrained by a non-swellable shell,” *J. Appl. Phys.*, vol. 117, no. 15, p. 154901, Apr. 2015.

[81] G. W. Scherer and D. M. Smith, “Cavitation during drying of a gel,” *J. Non. Cryst. Solids*, vol. 189, no. 3, pp. 197–211, Sep. 1995.

[82] S. Kundu and A. J. Crosby, “Cavitation and fracture behavior of polyacrylamide hydrogels,” *Soft Matter*, vol. 5, no. 20, p. 3963, Oct. 2009.

[83] W. Hong, X. Zhao, J. Zhou, and Z. Suo, “A theory of coupled diffusion and large deformation in polymeric gels,” *J. Mech. Phys. Solids*, vol. 56, pp. 1779–1793, 2008.

[84] M. Fujine, T. Takigawa, and K. Urayama, “Strain-driven swelling and accompanying stress reduction in polymer gels under biaxial stretching,” *Macromolecules*, vol. 48, no. 11, pp. 3622–3628, Jun. 2015.

[85] X. Wang and W. Hong, “A visco-poroelastic theory for polymeric gels,” *Proc. R. Soc. A Math. Phys. Eng. Sci.*, vol. 468, no. 2148, pp. 3824–3841, Dec. 2012.

[86] Y. Hu and Z. Suo, "Viscoelasticity and poroelasticity in elastomeric gels," *Acta Mech. Solida Sin.*, vol. 25, no. 5, pp. 441–458, Oct. 2012.

[87] J. Dervaux, Y. Couder, M.-A. Guedeau-Boudeville, and M. Ben Amar, "Shape transition in artificial tumors: from smooth buckles to singular creases," *Phys. Rev. Lett.*, vol. 107, no. 1, p. 018103, Jul. 2011.

[88] X. Hu, Z. Tong, and L. A. Lyon, "Multicompartment core/shell microgels," *J. Am. Chem. Soc.*, vol. 132, no. 33, pp. 11470–11472, Aug. 2010.

[89] H. M. Pan, M. Seuss, M. P. Neubauer, D. W. Trau, and A. Fery, "Tuning the mechanical properties of hydrogel core–shell particles by inwards interweaving self-assembly," *ACS Appl. Mater. Interfaces*, vol. 8, no. 2, pp. 1493–1500, Jan. 2016.

[90] S. Mytnyk, I. Ziemecka, A. G. L. Olive, J. W. M. van der Meer, K. A. Totlani, S. Oldenhof, M. T. Kreutzer, V. van Steijn, and J. H. van Esch, "Microcapsules with a permeable hydrogel shell and an aqueous core continuously produced in a 3D microdevice by all-aqueous microfluidics," *RSC Adv.*, vol. 7, no. 19, pp. 11331–11337, Feb. 2017.

[91] J. M. Ball, "Discontinuous equilibrium solutions and cavitation in nonlinear elasticity," *Philos. Trans. R. Soc. A Math. Phys. Eng. Sci.*, vol. 306, no. 1496, pp. 557–611, Oct. 1982.

[92] J. Sivaloganathan, "Uniqueness of regular and singular equilibria for spherically symmetric problems of nonlinear elasticity," *Arch. Ration. Mech. Anal.*, vol. 96, no. 2, pp. 97–136, Jun. 1986.

[93] C. O. Horgan, "Void nucleation and growth for compressible non-linearly elastic materials: An example," *Int. J. Solids Struct.*, vol. 29, no. 3, pp. 279–291, Jan. 1992.

[94] D.-T. Chung, C. O. Horgan, and R. Abeyaratne, "The finite deformation of internally pressurized hollow cylinders and spheres for a class of compressible elastic materials," *Int. J. Solids Struct.*, vol. 22, no. 12, pp. 1557–1570, Jan. 1986.

[95] P. Podio-Guidugli, G. V. Caffarelli, and E. G. Virga, "Discontinuous energy minimizers in nonlinear elastostatics: an example of J. Ball revisited," *J. Elast.*, vol. 16, no. 1, pp. 75–96, 1986.

[96] H.-H. Dai and Z. Song, "Some analytical formulas for the equilibrium states of a swollen hydrogel shell," *Soft Matter*, vol. 7, no. 18, p. 8473, Sep. 2011.

[97] O. Lopez-Pamies, T. Nakamura, and M. I. Idiart, "Cavitation in elastomeric solids: II—Onset-of-cavitation surfaces for Neo-Hookean materials," *J. Mech. Phys. Solids*, vol. 59, no. 8, pp. 1488–1505, Aug. 2011.

[98] T. Nakamura and O. Lopez-Pamies, “A finite element approach to study cavitation instabilities in non-linear elastic solids under general loading conditions,” *Int. J. Non. Linear. Mech.*, vol. 47, no. 2, pp. 331–340, Mar. 2012.

[99] M. H. Dickinson, C. T. Farley, R. J. Full, M. A. R. Koehl, R. Kram, and S. Lehman, “Animals Move : An Integrative View,” vol. 288, no. 5463, pp. 100–106, 2013.

[100] I. A. Anderson, T. A. Gisby, T. G. McKay, B. M. O’Brien, and E. P. Calius, “Multi-functional dielectric elastomer artificial muscles for soft and smart machines,” *J. Appl. Phys.*, vol. 112, no. 4, 2012.

[101] K. G. Pearson, J. E. Misiaszek, and K. Fouad, “Enhancement and resetting of locomotor activity by muscle afferents,” *Ann. N. Y. Acad. Sci.*, pp. 203–215, 1998.

[102] J. Duysens, F. Clarac, and H. Cruse, “Load-regulating mechanisms in gait and posture: comparative aspects.,” *Physiol. Rev.*, vol. 80, no. 1, pp. 83–133, 2000.

[103] L. Skedung, M. Arvidsson, J. Y. Chung, C. M. Stafford, B. Berglund, and M. W. Rutland, “Feeling small: exploring the tactile perception limits.,” *Sci. Rep.*, vol. 3, p. 2617, 2013.

[104] R. Okazaki, M. Sato, S. Fukushima, M. Furukawa, and H. Kajimoto, “Tactile enhancement structure mimicking hair follicle receptors,” in *2011 IEEE World Haptics Conference*, 2011, pp. 335–337.

[105] S. Tsuji, “A tactile and proximity sensor by optical and electrical measurement,” in *2012 IEEE Sensors*, 2012, pp. 1–4.

[106] S. Yao and Y. Zhu, “Wearable multifunctional sensors using printed stretchable conductors made of silver nanowires,” *Nanoscale*, vol. 6, no. 4, pp. 2345–2352, Jan. 2014.

[107] Youngseok Kim, Namsun Chou, and Sohee Kim, “Highly sensitive capacitive tactile sensor based on silver nanowire using parylene-C stencil patterning method,” in *2015 IEEE SENSORS*, 2015, pp. 1–3.

[108] R. E. Pelrine, R. D. Kornbluh, and J. P. Joseph, “Electrostriction of polymer dielectrics with compliant electrodes as a means of actuation,” *Sensors Actuators A Phys.*, vol. 64, no. 1, pp. 77–85, 1998.

[109] R. Pelrine, R. Kornbluh, Q. Pei, and J. Joseph, “High-speed electrically actuated elastomers with strain greater than 100%,” *Science (80-.).*, vol. 287, no. 5454, pp. 836–839, 2000.

[110] M. Duduta, R. J. Wood, and D. R. Clarke, “Multilayer Dielectric Elastomers for Fast, Programmable Actuation without Prestretch,” *Adv. Mater.*, 2016.

[111] C. Keplinger, J.-Y. Sun, C. C. Foo, P. Rothemund, G. M. Whitesides, and Z. Suo,

"Stretchable, Transparent, Ionic Conductors," *Science (80-.).*, vol. 341, no. 6149, pp. 984–987, 2013.

[112] S. Kim, C. Laschi, and B. Trimmer, "Soft robotics: A bioinspired evolution in robotics," *Trends Biotechnol.*, vol. 31, no. 5, pp. 287–294, 2013.

[113] K. Jung, J. C. Koo, J. Nam, Y. K. Lee, and H. R. Choi, "Artificial annelid robot driven by soft actuators.," *Bioinspir. Biomim.*, vol. 2, no. 2, pp. S42–S49, 2007.

[114] M. T. Petralia and R. J. Wood, "Fabrication and analysis of dielectric-elastomer minimum-energy structures for highly-deformable soft robotic systems," *IEEE/RSJ 2010 Int. Conf. Intell. Robot. Syst. IROS 2010 - Conf. Proc.*, pp. 2357–2363, 2010.

[115] T. A. Gibsy, S. Xie, E. P. Calius, and I. A. Anderson, "Integrated sensing and actuation of muscle-like actuators," in *Proc. SPIE 7287, Electroactive Polymer Actuators and Devices (EAPAD) 2009*, 2009, p. 728707.

[116] Q. Pei, M. Rosenthal, S. Stanford, H. Prahlad, and R. Pelrine, "Multiple-degrees-of-freedom roll actuators," *Smart Mater. Struct.*, vol. 13, pp. N86–N92, 2004.

[117] S. Son and N. C. Goulbourne, "Dynamic response of tubular dielectric elastomer transducers," *Int. J. Solids Struct.*, vol. 47, no. 20, pp. 2672–2679, 2010.

[118] T. A. Gisby, B. M. O'Brien, S. Q. Xie, E. P. Calius, and I. A. Anderson, "Closed loop control of dielectric elastomer actuators," in *Proc. SPIE 7976, Electroactive Polymer Actuators and Devices (EAPAD)*, 2011, pp. 797620–797628.

[119] K. Jung, K. J. Kim, and H. R. Choi, "A self-sensing dielectric elastomer actuator," *Sensors Actuators, A Phys.*, vol. 143, no. 2, pp. 343–351, 2008.

[120] A. N. Gent, "A New Constitutive Relation for Rubber," *Rubber Chem. Technol.*, vol. 69, no. 1, pp. 59–61, 1996.

[121] J. Huang, T. Li, C. C. Foo, J. Zhu, D. R. Clarke, and Z. Suo, "Giant, voltage-actuated deformation of a dielectric elastomer under dead load," *Appl. Phys. Lett.*, vol. 1001, no. 10, pp. 41911–71101, 2012.

[122] R. Kaltseis, C. Keplinger, S. J. Adrian Koh, R. Baumgartner, Y. F. Goh, W. H. Ng, A. Kogler, A. Tröls, C. C. Foo, Z. Suo, and S. Bauer, "Natural rubber for sustainable high-power electrical energy generation," *RSC Adv.*, vol. 4, no. 53, pp. 27905–27913, Jun. 2014.

[123] J. Huang, S. Shian, R. M. Diebold, Z. Suo, and D. R. Clarke, "The thickness and stretch dependence of the electrical breakdown strength of an acrylic dielectric elastomer," *Appl. Phys. Lett.*, vol. 101, no. 12, 2012.

[124] T. G. McKay, E. Galius, and I. A. Anderson, “The dielectric constant of 3M VHB: a parameter in dispute,” in *Proc. SPIE 7287, Electroactive Polymer Actuators and Devices (EAPAD)*, 2009, pp. 72870–72879.

[125] J. J. Sheng, H. L. Chen, J. H. Qiang, B. Li, and Y. Q. Wang, “Thermal, Mechanical, and Dielectric Properties of a Dielectric Elastomer for Actuator Applications,” *J. Macromol. Sci. Part B-Physics*, vol. 51, no. 10, pp. 2093–2104, 2012.

[126] G. Kofod, P. Sommer-Larsen, R. Kornbluh, and R. Pelrine, “Actuation Response of Polyacrylate Dielectric Elastomers,” *J. Intell. Mater. Syst. Struct.*, vol. 14, no. 12, pp. 787–793, Dec. 2003.

[127] M. R. Shankar, M. L. Smith, V. P. Tondiglia, K. M. Lee, M. E. McConney, D. H. Wang, L.-S. Tan, and T. J. White, “Contactless, photoinitiated snap-through in azobenzene-functionalized polymers.,” *Proc. Natl. Acad. Sci. U. S. A.*, vol. 110, no. 47, pp. 18792–7, Nov. 2013.

[128] D. E. Hagaman, S. Leist, J. Zhou, and H.-F. Ji, “Photoactivated Polymeric Bilayer Actuators Fabricated via 3D Printing,” *ACS Appl. Mater. Interfaces*, no. 10, pp. 27308–27315, 2018.

[129] A. A. Skandani, S. Chatterjee, M. L. Smith, J. Baranski, D. H. Wang, L.-S. Tan, T. J. White, and M. R. Shankar, “Discrete-state photomechanical actuators,” *Extrem. Mech. Lett.*, vol. 9, pp. 45–54, Dec. 2016.

[130] Y. Forterre, J. M. Skotheim, J. Dumais, and L. Mahadevan, “How the Venus flytrap snaps,” *Nature*, vol. 433, no. 7024, pp. 421–425, Jan. 2005.

[131] S. Armon, E. Efrati, R. Kupferman, and E. Sharon, “Geometry and Mechanics in the Opening of Chiral Seed Pods,” *Science (80-.).*, vol. 333, no. 6050, pp. 1726–1730, Sep. 2011.

[132] M. J. Harrington, K. Razghandi, F. Ditsch, L. Guiducci, M. Rueggeberg, J. W. C. Dunlop, P. Fratzl, C. Neinhuis, and I. Burgert, “Origami-like unfolding of hydro-actuated ice plant seed capsules,” *Nat. Commun.*, vol. 2, p. 337, Jun. 2011.

[133] E. Sharon, M. Marder, and H. L. Swinney, “Leaves, flowers and garbage bags: making waves,” *Am. Sci.*, vol. 92, no. 3, pp. 254–261, 2004.

[134] G. Stoychev, N. Puretskiy, and L. Ionov, “Self-folding all-polymer thermoresponsive microcapsules,” *Soft Matter*, vol. 7, no. 7, p. 3277, Mar. 2011.

[135] Z. Wei, Z. Jia, J. Athas, C. Wang, S. R. Raghavan, T. Li, and Z. Nie, “Hybrid hydrogel sheets that undergo pre-programmed shape transformations,” *Soft Matter*, vol. 10, no. 41,

pp. 8157–8162, Oct. 2014.

[136] S. Jiang, F. Liu, A. Lerch, L. Ionov, and S. Agarwal, “Unusual and Superfast Temperature-Triggered Actuators,” *Adv. Mater.*, vol. 27, no. 33, pp. 4865–4870, Sep. 2015.

[137] J. Kim, J. A. Hanna, M. Byun, C. D. Santangelo, and R. C. Hayward, “Designing Responsive Buckled Surfaces by Halftone Gel Lithography,” *Science (80-.).*, vol. 335, no. 6073, pp. 1201–1205, Feb. 2012.

[138] J.-H. Na, A. A. Evans, J. Bae, M. C. Chiappelli, C. D. Santangelo, R. J. Lang, T. C. Hull, and R. C. Hayward, “Programming Reversibly Self-Folding Origami with Micropatterned Photo-Crosslinkable Polymer Trilayers,” *Adv. Mater.*, vol. 27, no. 1, pp. 79–85, Jan. 2015.

[139] G. Stoychev, S. Zakharchenko, S. Turcaud, J. W. C. Dunlop, and L. Ionov, “Shape-Programmed Folding of Stimuli-Responsive Polymer Bilayers,” *ACS Nano*, vol. 6, no. 5, pp. 3925–3934, May 2012.

[140] Z. L. Wu, M. Moshe, J. Greener, H. Therien-Aubin, Z. Nie, E. Sharon, and E. Kumacheva, “Three-dimensional shape transformations of hydrogel sheets induced by small-scale modulation of internal stresses,” *Nat. Commun.*, vol. 4, p. 1586, Mar. 2013.

[141] E. Wang, M. S. Desai, and S.-W. Lee, “Light-Controlled Graphene-Elastin Composite Hydrogel Actuators,” *Nano Lett.*, vol. 13, no. 6, pp. 2826–2830, Jun. 2013.

[142] J. Deng, J. Li, P. Chen, X. Fang, X. Sun, Y. Jiang, W. Weng, B. Wang, and H. Peng, “Tunable Photothermal Actuators Based on a Pre-programmed Aligned Nanostructure,” *J. Am. Chem. Soc.*, vol. 138, no. 1, pp. 225–230, Jan. 2016.

[143] Y. Hu, G. Wu, T. Lan, J. Zhao, Y. Liu, and W. Chen, “A Graphene-Based Bimorph Structure for Design of High Performance Photoactuators,” *Adv. Mater.*, vol. 27, no. 47, pp. 7867–7873, Dec. 2015.

[144] T. Binkert, J. Oberreich, M. Meewes, R. Nyffenegger, and J. Rieka, “Coil-Globule Transition of Poly(N4sopropylacrylamide): A Study of Segment Mobility by Fluorescence Depolarization,” *Macromolecules*, vol. 24, pp. 5806–5810, 1991.

[145] M. Shibayama, T. Tanaka, and C. C. Han, “Small angle neutron scattering study on poly(N-isopropyl acrylamide) gels near their volume-phase transition temperature,” *J. Chem. Phys.*, vol. 97, no. 9, pp. 6829–6841, Nov. 1992.

[146] F. Afroze, E. Nies, and H. Berghmans, “Phase transitions in the system poly(N-isopropylacrylamide)/water and swelling behaviour of the corresponding networks,” *J. Mol. Struct.*, vol. 554, no. 1, pp. 55–68, Oct. 2000.

[147] K. Sano, Y. Ishida, and T. Aida, “Synthesis of Anisotropic Hydrogels and Their Applications,” *Angew. Chemie - Int. Ed.*, 2018.

[148] K. J. De France, F. Xu, and T. Hoare, “Structured Macroporous Hydrogels: Progress, Challenges, and Opportunities,” *Adv. Healthc. Mater.*, vol. 7, no. 1, p. 1700927, Jan. 2018.

[149] S. Palagi, A. G. Mark, S. Y. Reigh, K. Melde, T. Qiu, H. Zeng, C. Parmeggiani, D. Martella, A. Sanchez-Castillo, N. Kapernaum, F. Giesselmann, D. S. Wiersma, E. Lauga, and P. Fischer, “Structured light enables biomimetic swimming and versatile locomotion of photoresponsive soft microrobots,” *Nat. Mater.*, vol. 15, no. 6, pp. 647–653, Jun. 2016.

[150] M. Liu, Y. Ishida, Y. Ebina, T. Sasaki, T. Hikima, M. Takata, and T. Aida, “An anisotropic hydrogel with electrostatic repulsion between cofacially aligned nanosheets,” *Nature*, vol. 517, no. 7532, pp. 68–72, Jan. 2015.

[151] T. Liu, M. Huang, X. Li, C. Wang, C.-X. Gui, and Z.-Z. Yu, “Highly compressible anisotropic graphene aerogels fabricated by directional freezing for efficient absorption of organic liquids,” *Carbon N. Y.*, vol. 100, pp. 456–464, Apr. 2016.

[152] M. Chen, J. Zhu, G. Qi, C. He, and H. Wang, “Anisotropic hydrogels fabricated with directional freezing and radiation-induced polymerization and crosslinking method,” *Mater. Lett.*, vol. 89, pp. 104–107, Dec. 2012.

[153] P. Lin, T. Zhang, X. Wang, B. Yu, and F. Zhou, “Freezing Molecular Orientation under Stretch for High Mechanical Strength but Anisotropic Hydrogels,” *Small*, vol. 12, no. 32, pp. 4386–4392, Aug. 2016.

[154] J. Wu, Y. Lin, and J. Sun, “Anisotropic volume change of poly(N-isopropylacrylamide)-based hydrogels with an aligned dual-network microstructure,” *J. Mater. Chem.*, vol. 22, no. 34, p. 17449, Aug. 2012.

[155] W. Kong, C. Wang, C. Jia, Y. Kuang, G. Pastel, C. Chen, G. Chen, S. He, H. Huang, J. Zhang, S. Wang, L. Hu, W. Kong, C. Wang, C. Jia, Y. Kuang, G. Pastel, C. Chen, G. Chen, S. He, S. Wang, L. Hu, H. Huang, and J. Zhang, “Muscle-Inspired Highly Anisotropic, Strong, Ion-Conductive Hydrogels,” *Adv. Mater*, vol. 30, p. 1801934, 2018.

[156] Y. Kuang, C. Chen, J. Cheng, G. Pastel, T. Li, J. Song, F. Jiang, Y. Li, Y. Zhang, S.-H. Jang, G. Chen, T. Li, and L. Hu, “Selectively aligned cellulose nanofibers towards high-performance soft actuators,” *Extrem. Mech. Lett.*, vol. 29, p. 100463, May 2019.

[157] Y. Liu, H. Zhang, J. Wang, and Y. Zheng, “Anisotropic Swelling in Fiber-Reinforced Hydrogels: An Incremental Finite Element Method and Its Applications in Design of Bilayer Structures,” *Int. J. Appl. Mech.*, vol. 08, no. 07, p. 1640003, Oct. 2016.

[158] Y. Liu, H. Zhang, J. Zhang, and Y. Zheng, "Constitutive modeling for polymer hydrogels: A new perspective and applications to anisotropic hydrogels in free swelling," *Eur. J. Mech. - A/Solids*, vol. 54, pp. 171–186, Nov. 2015.

[159] P. Nardinocchi and L. Teresi, "Actuation performances of anisotropic gels," *J. Appl. Phys.*, vol. 120, no. 21, p. 215107, Dec. 2016.

[160] T. K. Tonge, L. M. Voo, and T. D. Nguyen, "Full-field bulge test for planar anisotropic tissues: Part II – A thin shell method for determining material parameters and comparison of two distributed fiber modeling approaches," *Acta Biomater.*, vol. 9, no. 4, pp. 5926–5942, Apr. 2013.

[161] T. K. Tonge, J. W. Ruberti, and T. D. Nguyen, "Micromechanical Modeling Study of Mechanical Inhibition of Enzymatic Degradation of Collagen Tissues," *Biophys. J.*, vol. 109, no. 12, pp. 2689–2700, Dec. 2015.

[162] D. Ye, P. Yang, X. Lei, D. Zhang, L. Li, C. Chang, P. Sun, and L. Zhang, "Robust Anisotropic Cellulose Hydrogels Fabricated via Strong Self-aggregation Forces for Cardiomyocytes Unidirectional Growth," *Chem. Mater.*, vol. 30, pp. 5175–5183, 2018.

[163] Y. Fung, "Elasticity of soft tissues in simple elongation," *Am. J. Physiol.*, vol. 213, no. 6, pp. 1532–1544, Dec. 1967.

[164] M. S. Sacks, "Incorporation of Experimentally-Derived Fiber Orientation into a Structural Constitutive Model for Planar Collagenous Tissues," *J. Biomech. Eng.*, vol. 125, no. 2, p. 280, Apr. 2003.

[165] S. Timoshenko, "Analysis of bi-metal Thermostats," *J. Opt. Soc. Am.*, vol. 11, no. 3, pp. 233–255, 1925.